MATRIX ISOLATION AND AB INITIO THEORETICAL INVESTIGATIONS OF CARBON-BASED MOLECULES OF ASTROPHYSICAL INTEREST

By

SCOTT P. EKERN

A DISSERTATION PRESENTED TO THE GRADUATE SCHOOL
OF THE UNIVERSITY OF FLORIDA IN PARTIAL FULFILLMENT
OF THE REQUIREMENTS FOR THE DEGREE OF
DOCTOR OF PHILOSOPHY

UNIVERSITY OF FLORIDA

1996

TABLE OF CONTENTS

page

LIST OF TABLES v

LIST OF FIGURES viii

ABSTRACT xiv

CHAPTERS

1 INTRODUCTION 1

Background 1
Experimental 4
Overview 10

2 SPECTROSCOPY AND PHOTOCHEMISTRY OF THE $C_3 \cdot H_2O$ COMPLEX 12

Introduction 12
Theoretical 14
Results 17
The $C_3 \cdot H_2O$ Complex 17
The trans-HPD Isomer 30
The cis-HPD Isomer 37
HPD Isomer Interconversion 42
Discussion 49
Summary 51

3 THE C_3H_2O POTENTIAL SURFACE 53

Introduction 53
Theoretical 56
Results 57
Discussion 69
Summary 76

4 A PHOTOCHEMICAL MECHANISM FOR C_3O FORMATION 81

Introduction 81
Theoretical 83
Results 84
The C_3H_2O Potential Surface 89
Bimolecular Reactions Forming C_3O 97
Summary 99

5 EXPERIMENTAL OBSERVATION OF LONG CHAIN CARBON ANIONS 101

Introduction 101
Experimental 102
Results 104
Electronic 104
Vibrational 118
Summary 120

6 THEORETICAL STUDIES OF CARBON ANIONS 122

Introduction 122
Theoretical 123
Results and Discussion 124
Linear Anions 124
Cyclic Anions 133
Summary 138

7 THEORETICAL STUDIES OF C_3 PERTURBED BY AN ARGON MATRIX 139

Introduction 139
Theoretical 140
Results 140
Discussion 147

8 FUTURE WORK 148

LIST OF REFERENCES 154

BIOGRAPHICAL SKETCH 165

LIST OF TABLES

Table page

2-1. Experimental frequencies and vibrational assignments for small carbon clusters in their ground states 16

2-2. Comparison of experimental (Ar matrix) and calculated (HF/6-31G*) IR frequencies and intensities for the $C_3 \bullet H_2O$ complex. Frequencies in cm^{-1} and intensities in km/mol. 20

2-3. The experimental (Ar matrix) and calculated (HF/6-31G*) IR frequencies for the CCC asymmetric stretching mode of $^{12/13}C_3 \bullet H_2O$ complex. Frequencies in cm^{-1} 22

2-4. The experimental (Ar matrix) and calculated IR frequencies (cm^{-1}) and intensities (km/mol) for trans-3-hydroxypropadienylidene (trans-HPD) in its ground electronic state. 31

2-5. Experimental and calculated (HF/6-31G*) IR frequencies (cm^{-1}) for all isotopomers of cis and trans-HPD for the most intense CCC asymmetric stretch, CCH+HCO bend (trans-HPD) and HCO bend + CO stretch (cis-HPD) modes. 35

2-6. The experimental (Ar matrix) and calculated IR frequencies (cm^{-1}) and intensities (km/mol) for cis-3-hydroxypropadienylidene (cis-HPD) in its ground electronic state. 40

3-1. Total energies (hartrees), zero-point corrected relative energies (kcal/mol), and zero-point energies (kcal/mol) of all minima calculated at the HF/6-31G* level. Total energy (hartrees) calculated at the QCISD(T)/6-31G*//HF/6-31G* level. HF/6-31G* calculated zero-point corrections scaled by 0.90. 59

3-2. Total energies (hartrees), zero-point corrected relative energies (kcal/mol), and zero-point energies (kcal/mol) of each transition state at the HF/6-31G* level. Total energy (hartrees) calculated at the QCISD(T)/6-31G*// HF/6-31G* level. HF/6-31G* calculated zero-point corrections scaled by 0.90. 60

3-3. Total energies (hartrees), zero-point corrected relative energies (kcal/mol), and zero-point energies (kcal/mol) of minima calculated at the MP2/6-31G* level. MP2/6-31G* calculated zero-point corrections scaled by 0.95. 61

3-4. Total energies (hartrees), zero-point corrected relative energies (kcal/mol), and zero-point energies (kcal/mol) for all transition states found at the MP2/6-31G* level. MP2/6-31G* calculated zero-point corrections scaled by 0.95. 62

3-5. Rotational constants (GHz) of minima found at the MP2/6-31G* level. Experimental values in parenthesis. 78

3-6. Vibrational frequencies (cm^{-1}), intensities (km/mol), and symmetries of each C_3H_2O isomer found at the MP2/6-31G* level. 79

4-1. Total energies (hartrees), zero-point corrected relative energies (kcal/mol), spin squared eigenvalues, and zero-point energies (kcal/mol) of minima found at the MP2/6-31G* level of theory. 85

4-2. Total energies (hartrees), zero-point corrected relative energies (kcal/mol), spin squared eigenvalues, and zero-point energies (kcal/mol) of transition states found at the MP2/6-31G* level of theory. 85

5-1. Experimental electronic absorption band positions (λ in nm, ν in cm^{-1}) and absorbances for anionic carbon clusters isolated in neon and argon matricies. Band widths (FWHM, in cm^{-1}) in parenthesis. All 0-0 transition energies are plotted in Figure 5-6 110

6-1. Linear carbon anion total energies (hartrees), zero-point energies (kcal/mol), rotational constants (GHz), spin squared values, in their ground electronic states calculated at the B3LYP/6-31G* level of theory. . . . 126

6-2. Vibrational frequencies (cm^{-1}), IR intensities (km/mol), and symmetries for linear carbon anions C_n^- (n = 2-9) calculated at the B3LYP/6-31G* level of theory 127

6-3. A comparison of experimental and select calculated linear carbon anion bands. Frequencies in cm^{-1}, intensities in km/mol 128

6-4. Energies of reaction (kcal/mol) between neutral linear carbon chains ($n_{prod} \leq 9$ atoms) calculated at the B3LYP/6-31G* level of theory. Not zero-point corrected. 130

6-5. Energies of reaction (kcal/mol) between linear carbon neutrals (abscissa) and linear carbon anions (ordinate) yielding a longer linear carbon anion. Calculated at the B3LYP/6-31G* level of theory. Electronic states in parenthesis. 131

6-6. Symmetries, total energies (hartrees), spin squared values, zero-point energies (kcal/mol), and the number of imaginary frequencies (*iv*) found for each of the cyclic carbon anion species. 135

6-7. Vibrational frequencies of the cyclic carbon anions calculated at the B3LYP/6-31G* level. Frequencies are in cm^{-1} and intensities are in km/mol. 136

7-1. Total energies (hartrees), relative energies (kcal/mol), geometric parameters (in angstroms and degrees), and Mulliken charges for the central carbon--argon orientation as a function of C_3-Ar distance. 141

7-2. Total energies (hartrees), relative energies (kcal/mol), goemetric parameters (in angstroms and degrees), and Mulliken charges for the bridging carbon--argon orientation as a function of C_3-Ar distance. 142

7-3. Total energies (hartrees), relative energies (kcal/mol), goemetric parameters (in angstroms and degrees), and Mulliken charges for the terminal carbon--argon orientation as a function of C_3-Ar distance. 143

LIST OF FIGURES

Figure page

1-1. Experimental set-up for matrix isolation of carbon anions produced by electron impact ionization 5

1-2. Expander module and matrix window 6

1-3. Experimental set-up for matrix isolation of carbon anions produced by dual laser vaporization of graphite and yttrium metal. 7

1-4. The experimental reaction scheme relevant to Chapters 2, 3, and 4 11

2-1. Structures of the intermediates hydroxyethynlcarbene (HEC, **1**), cis-3-Hydroxypropadienylidene (cis-HPD, **2**), trans-3-hydroxypropadienylidene (trans-HPD, **3**), the $C_3 \bullet H_2O$ complex (**4**), and the transition state between the complex and the HPD isomers (**5**). 15

2-2. Portions of the 10K matrix infrared spectrum of $^{12}C/Ar + H_2O$ (0.1%) in the asymmetric stretch region (ca. 2000 cm^{-1}) and in the OH asymmetric (ν_3) and symmetric (ν_1) region (ca. 3700 cm^{-1}). Monomer (M) and dimer (D) bands are marked; $C_3 \bullet H_2O$ complex bands are starred. Inset shows the $\nu_2 + \nu_3$ combination band of H_2O 18

2-3. Portion of the annealed (32K) matrix infrared spectra of $^{12}C/^{13}C/Ar$ ($[^{12}C]:[^{13}C] = 1:1$) (top) and of ^{12}C (12K) (bottom) in the asymmetric CC stretching region. The C_3 isotopomers are marked by triangles, while the $C_3 \bullet H_2O$ complex isotopomers are marked with dots. The marked bands in the lower spectrum are due to C_9 (1998 cm^{-1}), C_3 (2039 cm^{-1}), and the $C_3 \bullet H_2O$ complex (2052 cm^{-1}). 21

2-4. Portion of the 12K matrix infrared spectra of $^{12}Cn/Ar + H_2O$ (0.2%) in the OH stretch region before photolysis (b) and after photolysis (a). The monomer (M), dimer (D), and trimer (T) bands of water are marked accordingly. The starred bands are the OH stretches in the $C_3 \bullet H_2O$ complex. 24

2-5. Portion of the 12K matrix infrared spectra of $^{12}Cn/Ar + H_2O$ (0.2%) before photolysis and after photolysis ($\lambda > 390$ nm). Bands which have grown upon photolysis are due to C_3O, propynal, and trans-HPD. Note that the $C_3{\bullet}H_2O$ complex band has decreased upon photolysis. $C_3{\bullet}(H_2O)_n$ (n = 2 and 3) bands are marked by stars. 25

2-6. Portion of the 12K matrix infrared spectra of $^{12}Cn/Ar + H_2O$ (0.2%) before photolysis (b) and after photolysis (a) ($\lambda > 390$ nm). All bands in the difference spectrum are due to trans-HPD. 26

2-7. Electronic spectra for $^{12}C_3$ and $^{12}C_3{\bullet}H_2O$ complex before photolysis (upper) and after (lower). Band at 405.4 nm is assigned to the $^{12}C_3{\bullet}H_2O$ complex. 28

2-8. Comparison of the experimental (upper) and theoretical (lower) spectra of trans-HPD. Bands with one star, two stars, and dots are due to the $C_3{\bullet}H_2O$ complex, propynal, and trans-HPD, respectively. 32

2-9. Portion of the 12K matrix infrared spectra of $^{12}C/^{13}C/Ar + H_2O$ (0.15%) ($[^{12}C]:[^{13}C] = 1:2$) before photolysis and after 30 min of photolysis ($\lambda > 390$ nm). The negative peaks in the difference spectrum (triangles) are the asymmetric CCC stretches of the $^{12,13}C_3{\bullet}H_2O$ complex isotopomers. The positive peaks (dots) are the asymmetric CCC stretches of the $^{12,13}C_3$ sustituted trans-HPD isotopomers. 34

2-10. Portion of the 12K matrix infrared spectrum of $^{12}C/^{13}C/Ar + H_2O$ (0.15%) ($[^{12}C]:[^{13}C] = 1:2$) after 30 min photolysis ($\lambda > 390$ nm). Isotopomeric bands are due to trans-HPD. 36

2-11. Portion of the 12K matrix infrared spectra of $^{12}C_n/Ar + H_2O$ (0.2%) before and after 30 min of photolysis ($\lambda > 390$ nm), but recorded during photolysis. The 3245.2 and 3258.9 cm^{-1} bands are the $\nu_1 + \nu_3$ combination bands in C_3 and the $C_3{\bullet}H_2O$ complex. 38

2-12. Portion of the 12K matrix infrared spectra of $^{12}C/^{13}C/Ar + H_2O$ (0.15%) ($[^{12}C]:[^{13}C] = 1:2$) before photolysis and after 30 min photolysis ($\lambda > 390$ nm), but recorded during photolysis. The 1254.3 cm^{-1} band is the COH bend + CO stretch of cis-HPD. 39

2-13. Portion of the 12K matrix infrared spectra of $^{12}C/^{13}C/Ar + H_2O$ (0.15%) ($[^{12}C]:[^{13}C] = 1:2$) after 30 min of photolysis ($\lambda > 390$ nm) and recorded with the photolysis lamp on (bottom) and off (middle). In the difference spectra (top) are shown the CCC asymmetric stretching modes of the Isotopomers of cis-HPD (positive peaks) and trans-HPD (negative peaks). . . . 41

2-14. Time dependence of the difference spectrum (A_t-A_∞). The t = 0 and and subsequent plots were scanned after the photolysis lamp was turned off. Each spectrum was recorded for ca. 10 sec, with A_∞ scanned after 2 hrs. The 1992.5 cm^{-1} (trans-HPD) band is at a maximum absorbance at t = 2 hr, at which time the 1999.6 cm^{-1} (cis-HPD band is at its maximum absorbance 43

2-15. Dependence of $\ln|A_t-A_\infty|$ vs. time after 30 min of photolysis ($\lambda > 390$ nm) of the $^{12}C_n/Ar + H_2O$ (0.15%) matrix for T = 11 and 20K. The A_t and A_∞ absorbances are identical to the ones shown in Figure 2-14. 45

2-16. Potential energy surface for the rotation of the H atom about the C-O bond of HPD in its ground electronic state. See text for ΔE and $\Delta G°$ values. 48

3-1. Unoptimized structures of C_3H_2O isomers studied. 58

3-2. The HF/6-31G* calculated potential surface. Only lowest energy isomers are shown. Zero-point corrected energies (kcal/mol) relative to **A** in parenthesis. 63

3-3. The QCISD(T)/6-31G*//HF/6-31G* calculated potential surface. Only lowest energy isomers are shown. Zero-point corrected energies (kcal/mol) relative to **A** in parenthesis. 64

3-4. The MP2/6-31G* calculated potential surface. Only lowest energy isomers are shown. Zero-point corrected energies (kcal/mol) relative to **A** in parenthesis. 65

3-5. Optimized structures of all minima found at the MP2/6-31G* level of theory 66

3-6. Optimized structures of all transition structures found at the MP2/6-31G* level of theory 68

3-7. Portion of the 12K matrix infrared spectrum of $^{12}C_n/Ar$ before and after photolysis ($\lambda > 390$ nm) with a water filter present 74

3-8. Portion of the 12K matrix infrared spectrum of $^{12}C_n$/Ar before and after photolysis ($\lambda > 390$ nm) without a water filter 75

3-9. The experimental reaction scheme. The large arrow shows the reaction path described by the potential surface in Chapter 3. 77

4-1. The experimental reaction scheme. The large arrow shows the reaction path represented by the potential surface in Chapter 4 82

4-2. Optimized structures of all minima found at the MP2/6-31G* level of theory 87

4-3. Optimized structures of all transition states found at the MP2/6-31G* level of theory 88

4-4. Potential surface at the MP2/6-31G* level. Numbers are zero-point corrected energies (kcal/mol) relative to the $C_3 \bullet H_2O$ complex 90

4-5. Graph representing the singlet (squares) and triplet (circles) surfaces for H atom dissociation from cis-HPD (**C**). Note that the triplet surface approaches the molecule **F** + H atom total energies at infinite separation (68.1 kcal/mol). Energies are relative to the fully optimized cis-HPD molecule. 93

4-6. Graph representing the singlet (squares) and triplet (circles) surfaces for H atom dissociation from propynal (**E**). Note that the triplet surface approaches the molecule **F** + H atom total energies at infinite separation (130.4 kcal/mol). Energies are relative to the fully optimized propynal molecule. 94

4-7. Graph representing the singlet (squares) and triplet (circles) surfaces for H atom dissociation from trans-HPD (**B**). Note that the triplet surface approaches the molecule **G** + H atom total energies at infinite separation (98.0 kcal/mol). Energies are relative to the fully optimized trans-HPD molecule. 96

5-1. Part of the vibrational (left) and electronic (right) spectra for the C_n/C_n^- clusters in an Ar matrix at 12K, recorded before (upper) and after photolysis (lower). Photolysis was for 0.5 hr using a 265 nm cut-off filter. 105

5-2. Part of the electronic spectra of C_n species vaporized with two different laser beam densities at the vaporization point. In (a) a low flux of photons is used and no plasma is observed. In (b) a high flux of photons is used and a purple plasma is seen at the graphite surface. Note the difference in C_2 at 238.8 nm. 106

5-3. Part of the vibrational spectra of C_n species vaporized with two different laser beam densities at the vaporization point. In (a) a low flux of photons is used and no plasma is observed. In (b) a high flux of photons is used and a purple plasma is seen at the graphite surface 107

5-4. Spectrum showing absorption bands due to the electronic transitions of the C_{16}^- and C_{18}^- clusters isolated in an Ar matrix 108

5-5. Spectrum showing absorption bands due to electronic transitions of the C_{34}^- and C_{36}^- clusters isolated in an Ar matrix. Other known bands are marked accordingly 109

5-6. Graph of 0-0 electronic transition energy as a function of the number of carbon atoms in the anionic cluster 113

5-7. The infrared emission spectrum (UIR) recorded from planetary nebula NGC 7027 and HD4179. The positions of the 0-0 electronic transitions for chain carbon cluster anions C_n^- ($18 \leq n \leq 36$) from this work are indicated. UIR emission spectra taken from reference 17. 116

5-8. Portion of the infrared spectrum of C_n/C_n^- species trapped in an Ar matrix at 12K 119

6-1. Linear carbon anion optimized geometries. Bond lengths in angstroms. B3LYP/6-31G* lengths in bold type, ROHF/6-31G* lengths from reference 156 in normal type. 125

6-2. Plot of the exothermicity of the reaction between neutral carbon cluster chains (ordinate) and anionic carbon chains (in graph). Note the larger exothermicity for reactions with even numbered neutral chains. 132

6-3. Optimized structures of all stable cyclic anion structures found at the B3LYP/6-31G* level of theory. 134

7-1. Central, bridging, and terminal geometries 140

7-2. Potential energy for the bending of C_3 in the terminal orientation as a function of C-Ar distance. Energies are relative to the linear (CCC bond angle = 0°). 145

7-3. Interaction energies between C_3 and Ar in the central, bridging, and terminal orientations. Energies are relative to the completely optimized C_3•Ar complex. 146

8-1. Infrared emission spectra of several unsubstituted PAH molecules. Black bands at the bottom represent wavelengths where UIRs are observed. Spectra were recorded using the single-photon infrared emission spectroscopy (SPIRES) technique. Figure from reference 173. . . . 151

Abstract of Dissertation Presented to the Graduate School
of the University of Florida in Partial Fulfillment of the
Requirements for the Degree of Doctor of Philosophy

MATRIX ISOLATION AND AB INITIO THEORETICAL INVESTIGATIONS OF CARBON-BASED MOLECULES OF ASTROPHYSICAL INTEREST

By

Scott P. Ekern

December 1996

Chairperson: Martin T. Vala
Major Department: Chemistry

Carbon clusters and their products have been of interest to researchers for some time. This interest has arisen because of the involvement of carbon clusters in such diverse processes and products as soot, fullerenes, flames, nanotubes, and interstellar species. In this dissertation, two major avenues of research into carbon clusters are investigated. In the first, the complex formed between the C_3 cluster and water is probed experimentally and theoretically. Photolysis of the complex is shown to produce a stable intermediate and the products propynal and tricarbon monoxide. Further photolysis is of propynal yields acetylene and carbon monoxide. The structures of the intermediate and products are proven by isotopic substitution. The mechanisms for the most probable reaction pathways are investigated by ab initio calculations. The implication of these results for the formation of these species in small interstellar dust grains is explored.

The second major avenue of research investigated concerns carbon cluster anions. Relatively little work has been reported on these species compared to the neutral species. New methods for their production and stabilization in rare gas matrices are introduced. Density functional theory (DFT) has shown that the linear isomers are much more stable than their cyclic counterparts. DFT also been used to show that the reaction between neutral and anionic clusters is strongly exothermic. This is consistent with the experimental results which provide evidence for even-numbered carbon cluster anions from C_4 through C_{36}. The vibrational spectra of a number of these anions is also assigned. The electronic spectra for the C_n^- series spans the spectral range from the visible through the mid-infrared. It is shown that there is a reasonable match for the longer chain anions with several of the unidentified interstellar infrared emission bands.

CHAPTER 1
INTRODUCTION

Background

Matrix isolation spectroscopy was introduced originally by Whittle, Dows, and Pimentel in 1954.[1] Since then numerous books and articles have been published on the subject.[2,3] This technique involves the codeposition of a host matrix gas and the vapor of a guest molecule, which is the molecule of interest. The temperature of most matrices fall within the 4 to 20K range, with the final temperature being dependent on the refrigeration system and the melting temperature of the matrix host gas being employed. Typically, the temperature is kept several degrees below the melting temperature of the host material to minimize diffusion of guest species through the matrix. A matrix gas is chosen primarily with two criteria in mind. First, the matrix material should be transparent in the spectroscopic region of interest. Second, it should be as weakly interacting as possible with other host atoms or molecules and the guest material. Even though N_2 and O_2 are sometimes employed, the most widely chosen matrix materials are the noble gases: neon, argon, krypton, and xenon. They are transparent from the vacuum ultraviolet region to the far infrared. But most importantly, perturbation of the guest species is smallest when a rare gas is used. In order to minimize the possibility of aggregates of guest molecules,

which could undergo chemical reactions (photolytically induced or not) or perturb the spectrum, a large host-to-guest ratio is deposited. These ratios generally fall in the range 10^2 to 10^5:1, with most being 10^3:1.

Matrix isolation spectroscopy has the advantage of being able to trap ions, radicals, weakly bound complexes, atoms, and unusual molecules for long periods of time. For better or worse the trapped species are in their ground electronic and vibrational states. And, like at higher temperatures, fluorescence and phosphorescence are seen only from the lowest lying excited state. Careful control of temperature can influence the rate of diffusion, and this can be used to change the concentrations and/or identities of many species. There is even indication that molecules can be created in the matrix that could not be made in the gas phase because the matrix itself prevents parts of molecules from irreversibly separating after dissociation.[4] While there are many points that make matrix isolation spectroscopy a useful tool for interrogating charged or transient species, operating in the condensed phase has several unfortunate consequences. Most manifest themselves spectroscopically as some combination of line broadening, band splitting, line shape changes, or gas-to-matrix frequency shifts. All of these phenomena arise from guest/host interactions, and are, therefore, intrinsic to the technique. Since more attention is paid to the frequency shifts, priority is given to minimizing this effect. Shifts are approximately 1%, but many times this is enough to prevent positive band assignment. Argon is the most commonly used matrix material; however, neon is preferred as it exhibits the smallest shifts from gas phase values.

Matrix isolation spectroscopy is applied here to try to shed light on one of two longstanding and (possibly) related astrophysical problems. The first is concerned with a series of over 100 absorption bands spread throughout the visible and near infrared regions commonly known as the diffuse interstellar bands (DIBs).[5] The origins of these bands, originally discovered in 1934,[6] have been the subject of wide spread debate. Smith, Snow, and York[7] suggested some time ago that the carriers of the DIBs could be molecular in origin rather than solid grains. Since then linear carbon chains,[8] free carbene molecules,[9] polycyclic aromatic hydrocarbons (PAHs),[10] and the C_{60}^+ ion[11] have been proposed as molecular species contributing to the DIBs. These species were suggested because they and/or their ions have absorption bands in the visible and ultraviolet regions spanned by the DIBs. Recently a new hypothesis was forwarded which could conceivably account for all of the DIBs.[12] This model involves the nonlinear absorption of Lyman-alpha and optical photons near a star by the H_2 molecule. However, experiments have challenged this hypothesis by only being able to reproduce a few of the observed DIBs.[13]

The other part of the astrophysical puzzle deals with the unidentified infrared bands (UIRs). Discovered in 1973,[14,15] the interstellar infrared emission bands are a series of bands observed at 3.3, 6.2, 7.7, 8.8, and 11.3 μm. It has been proposed that the UIR bands originate from IR emission of neutral and/or ionic polycyclic aromatic hydrocarbons (PAHs).[16,17] The reasoning behind this is simple. The 3.3 and 6.2 μm bands correspond closely to an aromatic C-H stretch and C=C stretch in aromatic rings, respectively. The 7.7 μm band is also assigned to C-C stretch, however it is not seen in smaller aromatic compounds and could be representative of larger species.[18] The 8.8 and 11.3 μm bands

correspond to an in-plane aromatic C-H bend and an out-of-plane aromatic C-H bend, respectively. The position of the C-H out-of-plane bend band depends highly on the number of adjacent hydrogens on the ring, and can range from 11.0 to 13.3 μm.[19] Matrix isolation IR spectroscopy is a valuable tool to investigate the species (especially ions) suspected of contributing to the UIRs, largely due to its ability to isolate molecules at the very cold temperatures characteristic of the interstellar medium.

Experimental

Matrix isolation spectroscopy is carried out in a high vacuum chamber containing several windows and ports for the introduction of photons and gases (Figure 1-1). As each experiment has its own unique setup only the general details common to each experiment will be given here, and the specifics will be summarized in each chapter. The electron gun assembly shown in Figure 1-1 is shown for clarity only and is not present in each experiment.

The cryostat chamber is evacuated by an two inch air-cooled oil diffusion pump (Alcatel PDR 250, rated at 250 *l*/sec) backed by a mechanical roughing pump (Alcatel 2004, rated at 450 *l*/sec) and baffled by a liquid nitrogen cold trap. The pressure is monitored by an ion gauge (Kurt J. Lesker Co. Model G075K) and ion gauge controller (Granville-Phillips 280) spanning the range 10^{-4} though 10^{-8} torr. Vacuum was maintained between nonpermanent parts with rubber O-rings. Pressures inside the chamber with the window cooled to ca. 20K and the nitrogen trap filled were typically $3x10^{-8}$ torr. At room

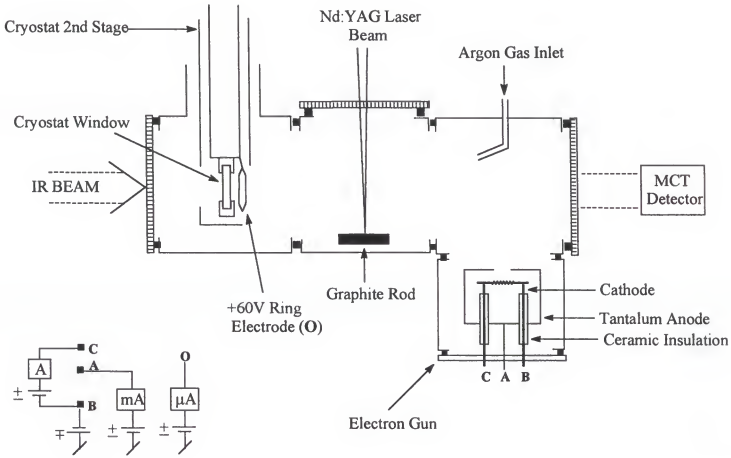

Figure 1-1. Experimental set-up for matrix isolation of carbon anions produced by electron impact ionization.

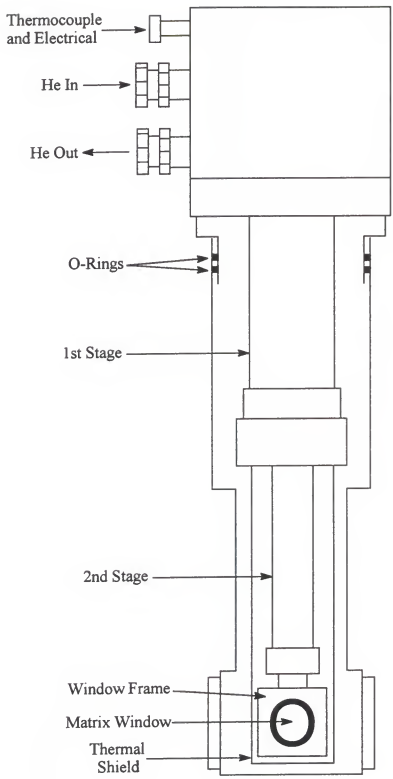

Figure 1-2. Expander module and matrix window.

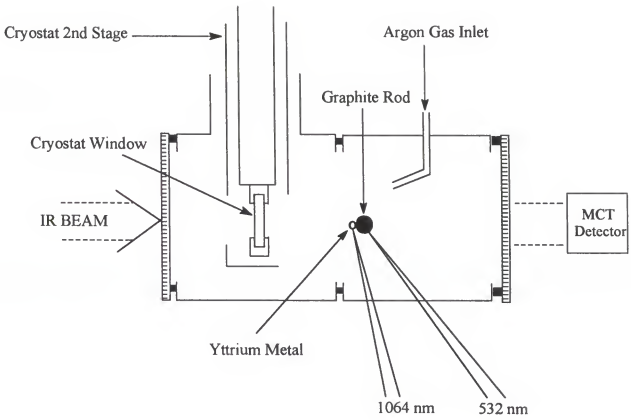

Figure 1-3. Experimental set-up for matrix isolation of carbon anions produced by dual laser vaporization of graphite and yttrium metal.

temperature, with only the diffusion and forepumps operating, the pressure was slightly more than a factor of 10 higher. Pressure during deposition never exceeded 1.2×10^{-7} torr, this translates into deposition times of 1 to 3 hours depending on the guest/host ratio.

The refrigerator is a two stage closed-cycle helium cryostat consisting of a compressor (Air Products Model 1RO4W) and an expander (Air Products Model DE 202). A copper radiation shield that partially surrounds the cold window is attached to the first stage (Figure 1-2). A window sandwiched between two halves of a copper frame is attached to the second stage. Matrix windows were BaF_2 (International Crystal Laboratories, transparent from 200 nm to 700 cm^{-1}). The cryostat expander can be rotated through 360° so the matrix window can face different external ports and windows.

Ionization of carbon clusters is achieved with two methods which take advantage of the high electron affinity of C_n carbon clusters (1.98 to 4.38 eV for $3 \leq n \leq 9$).[20,21] The first uses the electron gun assembly shown in Figure 1-1. The cathode is a 0.1 mm tungsten wire rolled into a coil and centered on a 3 mm exit hole. Emitted electrons are captured by carbon molecules and the negative carbon cluster ions are partially extracted from the vaporization region by an electric field created between the +60V O-ring electrode and -120V cathode of the electron gun, and then trapped in an Ar matrix. A canted ring electrode positioned above and adjacent to the deposition window serves to accelerate the ionizing electron beam and also acts as a monitor of electron production.

The second method involves dual laser beam plasma generation of carbon vapor and high energy photons from yttrium metal (Figure 1-3). Vacuum UV radiation and soft X-rays are produced when a pulsed Nd:YAG laser beam is focused onto metal targets such

as tungsten, molybdenum, and titanium.[22] In these experiments the fundamental (1064 nm) and second (532 nm) harmonics of an Nd:YAG laser are separated spatially with a prism. The second harmonic was used to vaporize graphite from a rod, while the fundamental was tightly focused onto a piece of tungsten metal placed in the center of the graphite rod. The two plasma plumes are generated simultaneously about 1.5 mm apart, and, instead of being partially extracted with a voltage, the negatively charged carbon ions (as well as other carbon material) are cryo-pumped onto the matrix window.

Two independent methods were used to measure window temperatures. A gold-chromel (0.07% Fe) thermocouple was joined with indium metal and placed between the window frame and second stage. The temperature was read digitally by a programmable temperature controller (Scientific Instruments Model 9600).

Research grade argon (Matheson Gas Products, 99.9995% pure) was used as the matrix gas throughout. Mixtures with CCl_4 and H_2O were made on a vacuum manifold to the indicated dilution. All carbon species were produced by pulsed Nd:YAG laser (Spectra Physics Model DCR-11, 532 and 1064 nm, 10 mJ/cm^2) vaporization of a graphite rod or pellet. Mixed isotopes of carbon were produced by laser vaporizing a pellet pressed from powders of ^{12}C (Alfa, 99.9995% pure) and ^{13}C (Isotec, 98.4% atom percent). The electronic (200-1000 nm) and vibrational (7000-700 cm^{-1}) absorption spectra of the trapped species were measured with a Cary 17 UV/VIS/IR spectrophotometer (0.5-1.0 nm resolution) and a MIDAC (Model M2000) FTIR spectrometer (0.5 cm^{-1} resolution), respectively. Photolysis of the matrices was carried out using a medium pressure mercury lamp with a 5 cm long H_2O heat-filter and color

filters (veb Jena) or with a 1kW Xe lamp plus a 0.25m monochrometer (2 mm slit) tunable over the 380-550 nm region.

Overview

This dissertation is grouped into three parts. Chapters 2, 3, and 4 are concerned with the photochemistry of the $C_3 \bullet H_2O$ complex. The experimental identification of the $C_3 \bullet H_2O$ complex and the hydroxypropadienylidene isomers is detailed in Chapter 2. Chapters 3 and 4 outline two theoretically generated potential surfaces which explain the presence of certain C_3H_2O isomers and other photoproducts observed experimentally. The two mechanisms are shown schematically in Figure 1-4 as they pertain to each chapter. Chapter 5 reports the experimental assignments of some newly-discovered carbon anion electronic and vibrational frequencies. Chapter 6 is a density functional theory modeling of linear and some cyclic carbon anion vibrational frequencies with comparison to the experimental results in Chapter 5. Finally, Chapter 7 reports the results of *ab initio* calculations on rare-gas/C_3 interactions. The aim of this chapter is to attempt to model (to a first approximation) how an argon atom might perturb a 'floppy' molecule like C_3 and how C_3 might influence its packing environment of argon atoms.

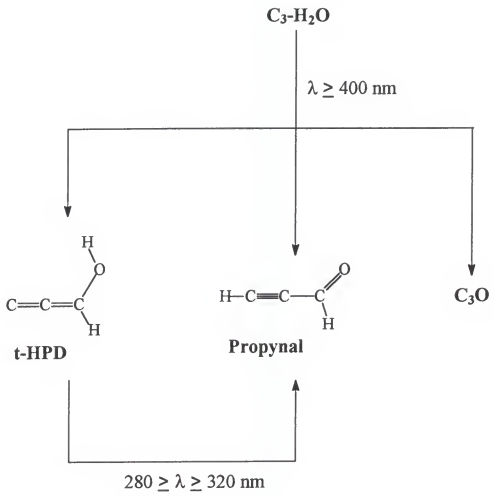

Figure 1-4. The experimental reaction scheme relevant to Chapters 2, 3, and 4.

CHAPTER 2
SPECTROSCOPY AND PHOTOCHEMISTRY OF THE $C_3 \cdot H_2O$ COMPLEX

Introduction

Interest in small carbon clusters has grown rapidly since the early pioneering work of Weltner and coworkers on the vibrational, electronic, and electron spin resonance spectroscopy of these species isolated in rare gas matrices.[23-25] Much of the current interest revolves around the structure, size, and widespread involvement of these clusters in various processes. They have been implicated in the formation of the fullerenes, in flame chemistry, in soot production, and in interstellar species.[26-30]

Carbon cluster work has proceeded rapidly in the past several years. The linearity (or near-linearity) of gaseous small carbon clusters ($n \leq 9$) is now generally accepted. The structure of C_3 has been investigated intensely.[31-34] The very low value of the bending frequency ($\nu_2 \sim 62$ cm^{-1}) in the gas phase suggests that the molecule is floppy. Recent calculations[33,35] show that the bending potential of free linear C_3 is essentially flat up to 160°. The $\nu_1 + \nu_3$ combination mode of all six $^{12}C/^{13}C$ isotopomers of C_3 have recently been measured,[36] with the conclusion that in Ar and Kr matrices the molecule is bent with a bond angle of 160°.

Although the main focus in the recent past has been on the structures of the carbon clusters, little attention has been given to their reactivities with other species. The reaction of small carbon clusters (C_n, $n \leq 5$) with H_2O in Ar matrices has, however, been investigated experimentally by Ortman, Hauge, Margrave, and Kafafi (OHMK).[37] These researchers concluded that certain carbon species, such as atoms in their ^3P ground states or diatomic molecules in their $^1\Sigma_g^+$ ground or $^3\Sigma_g^-$ excited states, do not react with H_2O. However, atomic carbon in its ^1D excited state is known to react with H_2O to form CO, H_2, and formaldehyde.[38] In their study of C_3 with H_2O, OHMK assigned the 2052 cm^{-1} band to the CCC asymmetric stretch of a $C_3 \cdot H_2O$ complex. It was originally suspected that a different species was responsible,[39] but here new evidence is presented which confirms OHMK's assignment. During photolysis with radiation of wavelengths $\leq$400 nm, OHMK observed that new bands grew in at 1999.8, 1992.8, 1459.6, 1252.5, and 1061.1 cm^{-1}. It was suggested that these bands originated from an intermediate, hydroxyethynylcarbene (HEC) (**1**), a photoproduct of the $C_3 \cdot H_2O$ complex. Later, Liu, Zhou, and Pulay (LZP) reported[40] *ab initio* results of **1** and the cis and trans isomers of 3-hydroxypropadienylidene (HPD) (**2**) and (**3**). From a comparison of OHMK's experimental spectra with their calculated IR frequencies and intensities, LZP suggested that **2** and **3**, not **1**, were responsible for the above IR bands.

In this chapter, results of the investigation of the photochemistry of the $C_3 \cdot H_2O$ complex are reported. In addition to the identification of the intermediate(s), there remain a number of other unsettled problems. (1) Besides the CCC asymmetric stretching mode, what are the other experimental IR frequencies of the $C_3 \cdot H_2O$ complex? (2) What are the

true identities of the 1999.8 cm^{-1} and 1992.8 cm^{-1} bands? Is one a site band of the other, as OHMK suggest, or are they the CCC asymmetric stretch modes of cis and trans-HPD, as LZP suggest? (3) Can the cis and trans isomers be differentiated experimentally? (4) Why do only wavelengths in the 400 nm region induce the $C_3 \cdot H_2O$ photoreaction? (5) What are the structures of the $C_3 \cdot H_2O$ complex and the cis and trans-HPD isomers in an Ar matrix? (6) Why are three IR bands predicted for the two isomers in the 1200-1300 cm^{-1} region, yet only two were observed by OHMK?

Theoretical

Ab initio calculations were carried out on the $C_3 \cdot H_2O$ complex (**4**), cis and trans-HPD (**2** and **3**), and the transition state between the complex and HPD isomers (**5**) (see Figure 2-1) using the GAUSSIAN 92 program package.[42] The calculations were carried out at the HF/6-31G* level with the optimized geometries shown in Figure 2-1. Other starting $C_3 \cdot H_2O$ geometries were tested in order to determine if multiple structures might exist. Interaction of the oxygen with the terminal carbon, the hydrogen or oxygen with the central carbon of C_3, and an O-H bond parallel to a C-C bond (both orientations) were used as starting geometries. In all cases the geometry ultimately optimized to the hydrogen bridged structure shown in Figure 2-1. Vibrational frequencies were calculated at the HF/6-31G* level to determine the nature of the stationary points and to help confirm experimental isotopomer assignments. Scaling factors for the calculated frequencies of the various isotopomers were determined by making a ratio of the

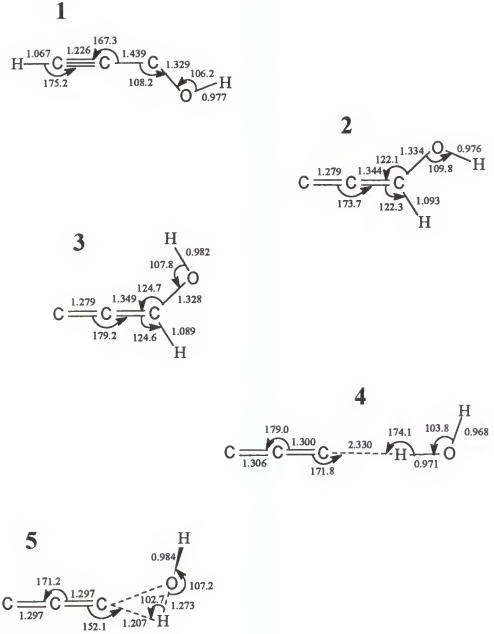

Figure 2-1. Structures of the intermediates hydroxyethynylcarbene (HEC, **1**), cis-3-hydroxypropadienylidene (cis-HPD, **2**), trans-3-hydroxypropadienylidene (trans-HPD, **3**), the $C_3 \cdot H_2O$ complex (**4**), and the transition state between the complex and the HPD isomers (**5**).

Table 2-1. Experimental frequencies and vibrational assignments for small carbon clusters in their ground states.

Carbon Cluster	Structure	Experimental Frequecies	Mode Description	Remarks
C_3 ($^1\Sigma_g^+$)	linear in gas phase[33,34] bent in Ar matrix[36]	2038.9[23] 1214.0[36] ~80[36,45]	asym. stretch, ν_3 (σ_u) sym. stretch, ν_1 (σ_g) bending, ν_2 (π_u)	2040.2 cm^{-1}, gas phase[46] 1224.5 cm^{-1}, gas phase[47] 63.4165 cm^{-1}, gas phase[48]
C_4 ($^3\Sigma_g^-$)	linear	1543.4[49]	asym. stretch, ν_3 (σ_u)	1548.9368 cm^{-1}, gas phase[54,55]
C_5 ($^1\Sigma_g^+$)	linear	2164[50] 1446.6[53]	asym. stretch, ν_3 (σ_u) asym. stretch, ν_4 (σ_u)	2169.44 cm^{-1}, gas phase[29,51]
C_6 ($^3\Sigma_g^-$)	linear	1952.5[52] 1197.3[53]	asym. stretch, ν_4 (σ_u) asym. stretch, ν_5 (σ_u)	1959.85852 cm^{-1}, gas phase[54,55]
C_7 ($^1\Sigma_g^+$)	linear or near linear	2128.1[43,54,55] 1894[51,52]	asym. stretch, ν_4 (σ_u) asym. stretch, ν_5 (σ_u)	2138.1951 cm^{-1}, gas phase[56-58]
C_8 ($^3\Sigma_g^-$)	linear or near linear			expected structure
C_9 ($^1\Sigma_g^+$)	linear or near linear	1998.4[59,60]	asym. stretch, ν_6 (σ_u)	2014.277964 cm^{-1}, gas phase[61]

experimental to calculated all ^{12}C isotopomer frequencies for a particular mode, then applying the ratio to the remaining calculated frequencies.

Results

The $C_3 \cdot H_2O$ Complex

The $C_3 \cdot H_2O$ complex has C_s symmetry and is predicted to be bound by a mere 1.4 kcal/mol (zero-point corrected). Figure 2-2 (right) shows the asymmetric CCC stretch region for a number of carbon clusters formed in an Ar matrix at 11K. The initial distribution for cluster sizes in the matrix depends on the power density of the laser beam, matrix deposition temperature and the Ar gas pressure in the deposition chamber. The clusters C_3 and C_2, and presumably C atoms, are favored when higher laser powers are used. A much broader distribution of clusters is made when the beam is defocused or lower laser powers are used. Aggregation of the clusters is readily achieved by annealing the matrix. This results from diffusion of the C_n species in solid Ar which increases rapidly with increasing temperature in the 20-36K range[43] and from the exothermic heats of formation of the carbon clusters.[44] In earlier work many of the IR bands observed in this region were assigned using matrix and/or gaseous samples. These assignments are compiled in Table 2-1.

Water is ubiquitous in matrix isolation experiments. Its removal is exceedingly difficult due to its high affinity for all surfaces. Its presence is however easily noted by the

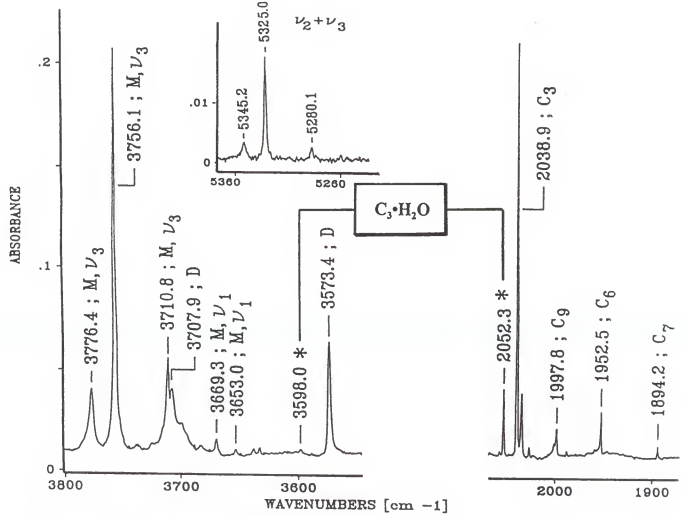

Figure 2-2. Portions of the 10K matrix infrared spectrum of $^{12}C_n/Ar + H_2O$ (0.1%) in the asymmetric stretch region (ca. 2000 cm^{-1}) and in the OH asymmetric (ν_3) and symmetric (ν_1) region (ca. 3700 cm^{-1}). Monomer (M) and dimer (D) bands are marked; $C_3 \cdot H_2O$ complex bands are starred. Inset shows the $\nu_2 + \nu_3$ combination band of H_2O.

appearance of the IR bands in the OH stretch region (ca. 3700 cm^{-1}). Figure 2-2 (left) shows the IR bands of matrix-isolated noninteracting H_2O monomers (M) and (D) for a sample formed from a mixture of Ar/0.1% H_2O/C_n clusters. The inset shows the region of the $\nu_2 + \nu_3$ combination bands of noninteracting H_2O. In addition to known bands attributable to water and carbon clusters, the figure also shows two bands at 2052.3 cm^{-1} and 3598.0 cm^{-1} (starred). The 2052 cm^{-1} band has been assigned previously by OHMK to the asymmetric CCC stretch of the $C_3 \bullet H_2O$ complex.

The 2052.3 cm^{-1} band. The vibrational frequencies and intensities for the $C_3 \bullet H_2O$ complex are given in Table 2-2. Twelve modes are predicted but only five intraspecies modes were observed. The calculated intermoiety modes and the C_3 bending mode are included in the table but were not observed since their frequencies are below the range of the spectrometer employed. The predictions include three perturbed OH modes at 1626.8, 3604, and 3705.2 cm^{-1} and two perturbed CC stretches at 1216 and 2052.3 cm^{-1}. The 2052 cm^{-1} mode is predicted to be the most intense, with three others about one-tenth as intense and one practically zero. These bands are compared in the table to the experimental bands assigned to the $C_3 \bullet H_2O$ complex. A discussion of these assignments follows below.

A mixed $^{12}C/^{13}C$ isotope run aided in the assignments of the bands and helped in establishing the geometry of the complex. For a symmetric complex (e.g., one with the H_2O bound symmetrically to the middle carbon) six isotopomer peaks are expected for the asymmetric CCC stretch. However, for an asymmetrically bound complex (e.g., H_2O bound to one end of the C_3) eight isotopomeric peaks are predicted. The experimental

Table 2-2. Comparison of experimental (Ar matrix) and calculated (HF/6-31G*) IR frequencies and intensities for the $C_3 \cdot H_2O$ complex. Frequencies in cm^{-1} and intensities in km/mol.

ν_{exp}	Intensity (exp)	ν_{calc}[a]	Intensity (calc)[b]	Mode Description
3712.2	(0.1)	3705.2	154.7 (0.11)	OH asym. stretch
3598.0	(0.09)	3604.0	82.0 (0.06)	OH sym. stretch
2052.3	(1.0)	2052.3	1450.5 (1.0)	CC asym. stretch
1593.4	(0.11)	1626.8	117.4 (0.08)	HOH bend
1214.2[c]	(0.0)	1216.0	2.9 (0.002)	CC sym. stretch
		270.0	168.7 (0.12)	
		203.2	74.3 (0.05)	
		144.0	7.9 (0.005)	
		138.7	29.9 (0.02)	
		83.9	1.29 (0.001)	
		37.2	8.3 (0.006)	
		33.8	0.2 (0.0)	

[a] Calculated frequencies scaled by 0.8856.
[b] Relative intensities in parenthesis.
[c] Expected value based on the 3258.9 cm^{-1} ($\nu_1 + \nu_3$) combination band of C_3 perturbed by H_2O in the $C_3 \cdot H_2O$ complex (see text).

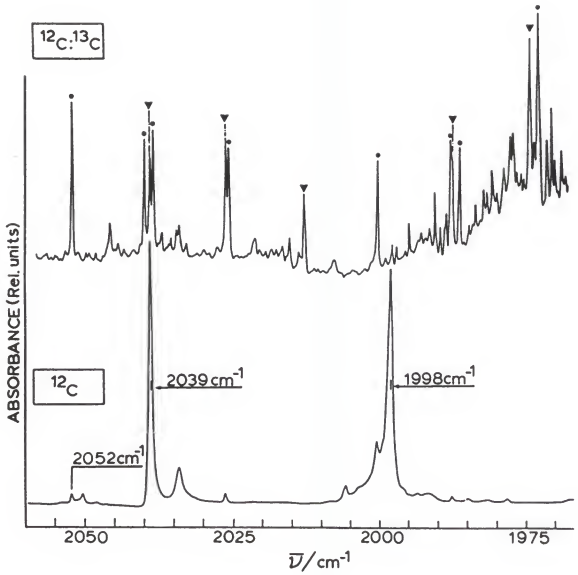

Figure 2-3. Portion of the annealed (32K) matrix infrared sprectra of $^{12}C/^{13}C/Ar$ ($[^{12}C]:[^{13}C]=1:1$) (top) and of $^{12}C/Ar$ (12K) (bottom) in the asymmetric CC stretching regoin. The C_3 isotopomers are marked by triangles, while the $C_3 \bullet H_2O$ complex isotopomers are marked with dots. The marked bands in the lower spectrum are due to C_9 (1998 cm^{-1}), C_3 (2039 cm^{-1}), and the $C_3 \bullet H_2O$ complex (2052 cm^{-1}).

Table 2-3. The experimental (Ar matrix) and calculated (HF/6-31G*) IR frequencies for the CCC asymmetric stretching mode of $^{12/13}C_3 \bullet H_2O$ complexes. Frequencies in cm^{-1}.

ν_{exp}	ν_{calc} [a] (FG+force const. fit)	ν_{calc} [b] (HF/6-31G*)	Isotopomer
2052.3	2052.82 (+0.52)	2052.3 (0.0)	12-12-12-1-16-1
2040.0	2040.19 (+0.19)	2040.1 (+0.1)	13-12-12-1-16-1
2038.5	2038.87 (+0.37)	2038.2 (-0.3)	12-12-13-1-16-1
2026.0	2025.33 (-0.67)	2025.5 (-0.5)	13-12-13-1-16-1
2000.5	2000.69 (+0.19)	1998.9 (-1.6)	12-13-12-1-16-1
1988.2	1987.86 (-0.54)	1986.5 (-1.7)	13-13-12-1-16-1
1986.5	1986.26 (-0.24)	1984.6 (-1.9)	12-13-13-1-16-1
1973.3	1972.40 (-0.90)	1971.5 (-1.8)	13-13-13-1-16-1

[a] Program from reference 62; deviations from experimental frequencies given in parentheses; RMS deviation of all 8 bands is 0.44 cm^{-1}. Force constants found in force constant adjustment calculation: $f(C_1\text{-}C_2) = 11.213$; $f(C_2\text{-}C_3) = 10.932$; $f(C_3 \bullet H_1) = 2.079$; $f(H_1\text{-}O) = 9.483$; $f(O\text{-}H_2) = 5.331$; $f(C_1\text{-}C_2, C_2\text{-}C_3) = 1.239$, and $f(H_1\text{-}O, O\text{-}H_2) = -1.208$ in units of 10^2 N m^{-1}.

[b] Scaled by 0.8856. Deviations from experimental frequencies given in parentheses.

spectrum of the $^{12,13}C_3 \bullet H_2O$ complex in the asymmetric CCC stretch region is shown in Figure 2-3. The band positions, collected in Table 2-3, are compared to a normal coordinate force constant adjustment calculation[62] and the *ab initio* frequencies. Both the force constant fit and the *ab initio* frequencies for a planar asymmetrical complex are close to the experimental values, leading to the conclusion that the 2052.4 cm^{-1} band is due to the asymmetric CCC stretch of the planar asymmetrical complex.

The 3598 cm^{-1} band. The spectra in Figures 2-4 to 2-6 give different regions of the IR spectrum of a $C_n/H_2O/Ar$ matrix before photolysis for a higher concentration (0.2%) than in Figure 2-2 (0.1%). The intensities of the 2052.4 cm^{-1} and 3597.6 cm^{-1} bands both increase with increasing water concentration while the 2038.9 cm^{-1} band (due to uncomplexed C_3) decreases. Forty different spectral runs, including photolysis and annealing experiments, established a positive correlation (correlation coefficient = 0.97) between the 3598 cm^{-1} band and the 2052.4 cm^{-1} band intensities. The 3598 cm^{-1} band, because of its proximity to the calculated frequency at 3604 cm^{-1} and the close match of experimental and calculated relative intensities, is attributed to the OH symmetric stretch of the $C_3 \bullet H_2O$ complex.

The 3712 cm^{-1} band. The OH asymmetric stretch in the complex is predicted to appear at 3705.2 cm^{-1}. As Figure 2-4 shows the experimental spectrum is very crowded in this region, with monomer, dimer, and trimer H_2O bands appearing. Upon photolysis changes are detected in this region. The changes are complicated by overlap with the 3711.5 cm^{-1} band ($1_{-1} \rightarrow 0_0$ transition of the ν_3 H_2O monomer mode) which is expected to remain unchanged upon photolysis. There are several reasons for believing that the

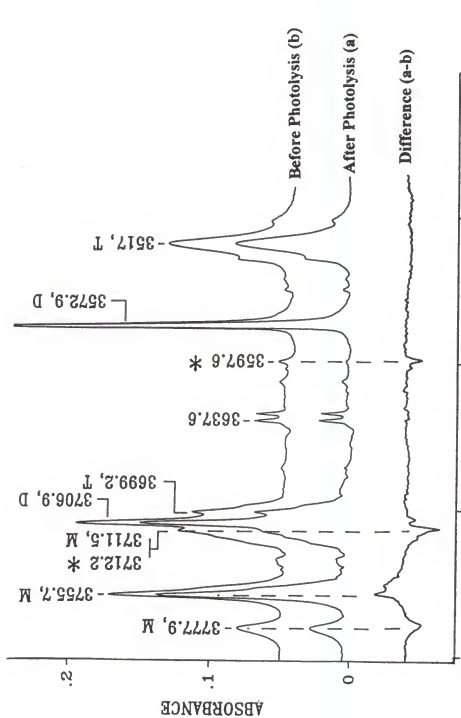

Figure 2-4. Portion of the 12K matrix infrared spectra of $^{12}C_n/Ar + H_2O$ (0.2%) in the OH stretch region before photolysis (b) and after photolysis (a). The monomer (M), dimer (D), and trimer (T) bands of water are marked accordingly. The starred bands are the OH stretches in the $C_3 \cdot H_2O$ complex.

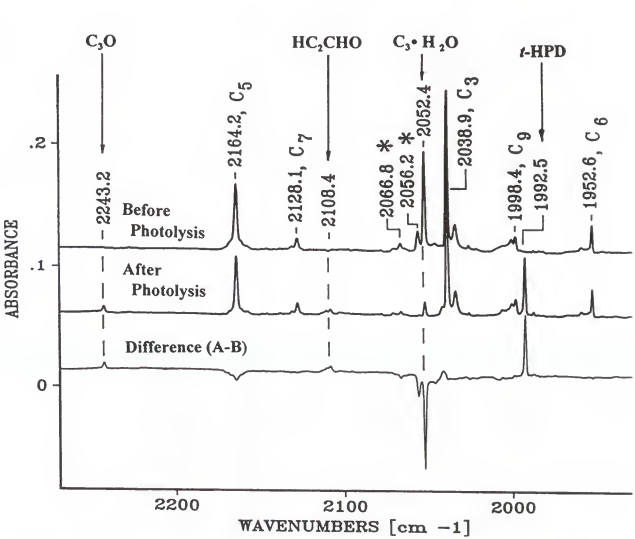

Figure 2-5. Portion of the 12K matrix infrared spectra of $^{12}C_n$/Ar + H_2O (0.2%) before photolysis and after photolysis ($\lambda > 390$ nm). Bands which have grown upon photolysis are due to C_3O, propynal, and trans-HPD. Note that the $C_3 \bullet H_2O$ complex band has decreased upon photolysis. $C_3 \bullet (H_2O)_n$ (n = 2 and 3) bands are marked by stars.

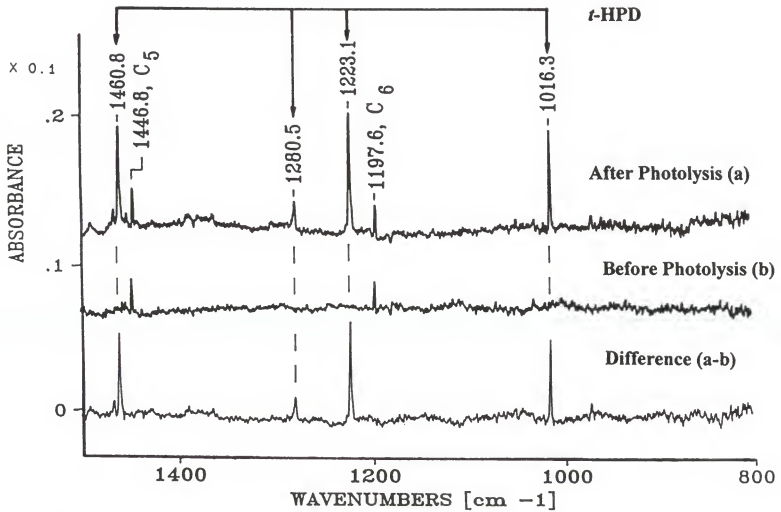

Figure 2-6. Portion of the 12K matrix infrared spectra of $^{12}C_n/Ar + H_2O$ (0.2%) before photolysis (b) and after photolysis (a) ($\lambda > 390$ nm). All bands in the difference spectrum are due to trans-HPD.

negative peak in the difference spectrum contains a contribution from the temperature dependent 3711.5 cm^{-1} band and the 3712.2 cm^{-1} $C_3 \bullet H_2O$ complex band. Namely, (1) the intensity ratio of the 3755.7 cm^{-1} ($0_0 \rightarrow 1_{-1}$) band to the 3777.9 cm^{-1} ($1_{-1} \rightarrow 2_{-2}$) band of the H_2O monomer is larger in spectrum (a) than in spectrum (b), indicating that the temperature is lower in (a). This is reasonable since (a) was recorded an hour later than (b), after the matrix had more time to cool. (2) The intensity ratio of the 3777.9 cm^{-1} and 3711.5 cm^{-1} bands is known[63] to be 1.4 at 15K in an Ar matrix. While it is not possible to determine this ratio here, it can be deduced from the $\nu_2 + \nu_3$ combination bands (Figure 2-2). The 5345.2 cm^{-1} (ν_2 + 3776.4 cm^{-1}) band is slightly more intense than the 5280.1 cm^{-1} (ν_2 + 3711.5 cm^{-1}) band, which here is shifted to 3710.8 cm^{-1}. It is expected that the 3776.4 and 3710.8 cm^{-1} bands should be in approximately the same ratio. But, as the difference spectrum in Figure 2-4 shows, the intensity ratio is inverted. Thus it is reasonable to conclude that another species is contributing to this band. Because of its proximity to the predicted 3705.2 cm^{-1} band, the 3712.2 cm^{-1} band is assigned to the OH asymmetric stretch of the $C_3 \bullet H_2O$ complex.

The 1214.3 and 1593.4 cm^{-1} bands. A perturbed HOH bend is predicted for the complex at 1626.8 cm^{-1} with an intensity intermediate between the two OH stretch modes. A band at 1593.4 cm^{-1}, having the correct behavior can be assigned to this mode. With photolysis this band decreases in intensity, in parallel with the 2052.2 cm^{-1} band, as expected.

A symmetric CC stretch is predicted at 1216 cm^{-1} and is expected to have very low intensity. Its presence can, however, be determined from the $\nu_1 + \nu_3$ combination region.

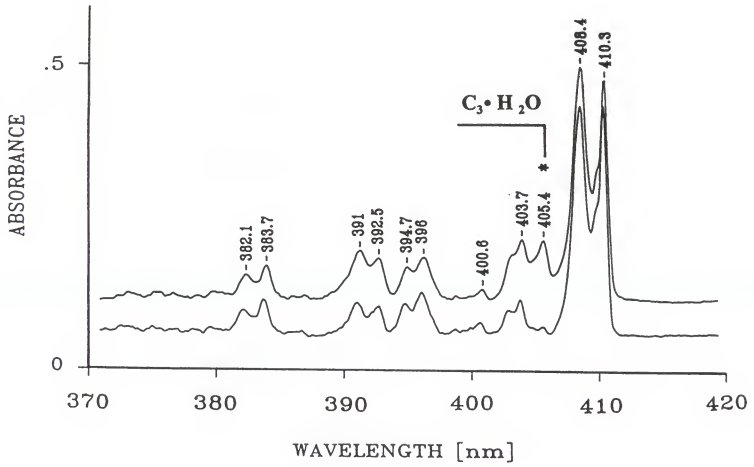

Figure 2-7. Electronic spectra for $^{12}C_3$ and $^{12}C_3 \bullet H_2O$ complex before photolysis (upper) and after (lower). Band at 405.4 nm is assigned to the $^{12}C_3 \bullet H_2O$ complex.

Two weak bands are observed in this region. One at 3245.2 cm^{-1}, which has been previously assigned[36,37] to the $\nu_1 + \nu_3$ combination band in C_3, and the other at 3258.9 cm^{-1} which we assign here to the $\nu_1 + \nu_3$ combination band of the complex. To determine the frequency of the ν_1 mode, we use the anharmonicity factor of 7.7 cm^{-1} found[36] for the combination mode of C_3 in Ar. If this value is correct for the complex also, it is expected that the CC symmetric mode frequency in $C_3 \bullet H_2O$ should be found at 3258.9 - 2052.4 + 7.7 cm^{-1} = 1214.2 cm^{-1}. This is very close to the observed ν_1 value of 1214.0 cm^{-1} for C_3 in Ar and to the 1216 cm^{-1} value calculated here for the complex. Furthermore, this band decreases upon photolysis of the matrix, as expected. Based on this evidence the CC symmetric stretch in the complex is assigned to the band at 1214.2 cm^{-1}.

Electronic spectrum. OHMK showed previously[37] that photolysis with $\lambda = 420$ nm produces no reaction, but with $\lambda > 400$ nm photochemical activity is observed. Since photolysis in the 400-500 nm region destroys the $C_3 \bullet H_2O$ complex, the electronic band of the complex responsible for activation was sought by scanning this region before and after photolysis. Figure 2-7 shows that a band at 405.4 nm disappears upon photolysis. Furthermore this band correlates well with the 2052.3 cm^{-1} band (correlation coefficient = 0.95). The integral intensity ratio, **I** (405.4 nm)/**I** (2052.3 cm^{-1}), is found to be ca. 70. The 405.4 nm band we assign to the electronic band origin of the complex, a transition analogous to the $^1\Pi \leftarrow {}^1\Sigma$ transition of uncomplexed C_3 at 408.4 nm.[23-25] The above assignment demonstrates that the rearrangement of the $C_3 \bullet H_2O$ complex to the isomers of HPD and/or C_3O requires the excess energy acquired from excitation to an excited electronic state of the complex.

$C_3 \bullet H_2O$ to HPD transition state. Using *ab initio* calculations, the transition state (TS) connecting the $C_3 \bullet H_2O$ complex and the trans-HPD isomer has been located. The optimized TS geometry found is illustrated in Figure 2-1. The $C_3 \bullet H_2O$ complex is planar with a long C-H hydrogen bridge (2.492Å). The TS geometry is nonplanar with the terminal carbon interacting with both the hydrogen and oxygen of H_2O. The C-H bond length has decreased to 1.257Å on its way to 1.075Å in the HPD isomers. The calculated barrier of 29.3 kcal/mol (MP2/6-31G* + zero-point correction) from complex to transition state represents a substantial endothermic barrier and explains why instantaneous reaction between C_3 and H_2O is not seen.

The trans-HPD Isomer

Photolysis of the matrix isolated mixture described above with $\lambda > 390$ nm leads to a decrease in the bands at 2066.8, 2056.2, 2052.4, 3597.6, and 3712.2 cm^{-1}. The latter three are due to the $C_3 \bullet H_2O$ complex, while the former two are tentatively assigned here to the $C_3(H_2O)_3$ and $C_3(H_2O)_2$ complexes, respectively. As a result of this photolysis, new bands appear at 2243.2, 2108.4, 1992.5, 1688.4, 1460.8, 1280.5, 1223.1, 1016.3, and 940.1 cm^{-1}. The 2243.2 and 2108.4 cm^{-1} bands have previously[37,64] been assigned to the asymmetric CCC stretch of C_3O and CC stretch of propynal, respectively. The remaining peaks must clearly also be photolysis products. It will be shown below that they are due to trans-HPD.

Table 2-4. The experimental (Ar matrix) and calculated IR frequencies (cm^{-1}) and intensities (km/mol) for trans-3-hydroxypropadienylidene (trans-HPD) in its ground electronic state.

trans-HPD					
	HF/6-31G*		DZP+diffuse[b]		Mode Description
ν_{exp}[c] (cm^{-1})	ν_{calc}[a]	Intensity[c]	ν_{calc}[b]	Intensity[c]	
	3619.7	120.4 (0.11)	3669	127 (0.10)	OH str.
	3051.2	10.3 (0.01)	3080	6 (0.005)	CH str.
1992.5 (1.0)	1974.0	1104.7 (1.0)	1940	1274 (1.0)	CCC asym. str.
1460.8 (0.14)	1487.9	292.0 (0.26)	1482	355 (0.28)	COH bend, CH str.
1280.5 (0.04)	1311.5	63.8 (0.06)	1309	105 (0.08)	COH bend, CO str.
1223.1 (0.16)	1222.6	265.5 (0.24)	1216	284 (0.22)	HCO, CCH bend
1016.3 (0.12)	1023.4	109.5 (0.10)	1018	91 (0.07)	CC, CO str.
	997.0	0.4 (0.0004)	995	1 (0.0008)	CH wag
	655.5	200.3 (0.18)	657.5	193 (0.15)	HOCC, HOCH tor.
	589.7	40.8 (0.04)	596.0	46 (0.04)	CCO bend
	196.0	2.6 (0.002)	267.2	1 (0.0008)	CCCO bend
	177.2	3.8 (0.003)	211.4	3 (0.002)	CCC bend

[a] Frequencies scaled by 0.897.
[b] From reference 40. Frequencies have been scaled by 0.9.
[c] Normalized relative intensities in parenthesis.

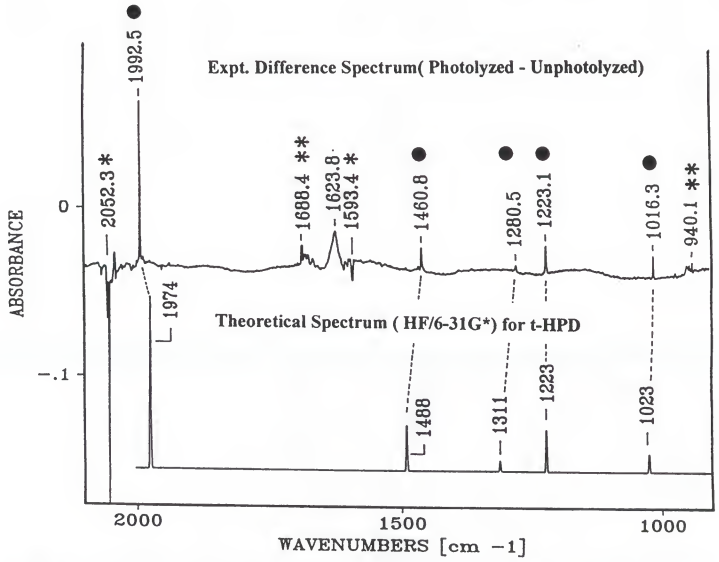

Figure 2-8. Comparison of the experimental (upper) and theoretical (lower) spectra of trans-HPD. Bands with one star, two stars, and dots are due to the $C_3 \cdot H_2O$ complex, propynal, and trans-HPD, respectively.

LZP have shown[40] on the basis of extensive *ab initio* calculations that one of the major products of photolysis of the $C_3 \bullet H_2O$ complex is probably trans-HPD. In Table 2-4 are presented experimental frequencies and intensities, results from LZP's calculation and *ab initio* calculations for trans-HPD from this work. A graphical comparison is given in Figure 2-8. It can be seen that the correspondence for the bands at 1992.5, 1460.8, 1280.5, 1223.1, and 1016.3 cm^{-1} is quite good. Even at the SCF level the calculated frequencies and intensities match reasonably well with experiment, the largest frequency deviation being ca. 30 cm^{-1}.

Further support for this assignment comes from $^{12}C/^{13}C$ isotopic studies. Taking into account all possible unique arrangements of ^{12}C and ^{13}C in the HPD molecule, eight isotopomeric bands are expected. In Figure 2-9 are shown the $^{12}C/^{13}C$ mixed isotope spectra before and after photolysis. The difference spectrum shows a series of eight negative peaks, attributed above to the isotopomers of the $C_3 \bullet H_2O$ complex. Also shown in the difference spectrum are a series of eight positive peaks which are also listed in Table 2-5. The table gives the results of the *ab initio* calculations of the IR frequencies for the eight isotopomers of trans-HPD. As confirmation of this assignment, the isotopomeric band structure was sought for the next most intense trans-HPD band at 1223.1 cm^{-1}. A set of five weak bands, found in this region, are displayed in Figure 2-10. The energy spread of these bands is much smaller than the spread in the 1992.5 cm^{-1} range (5.5 cm^{-1} vs. 84.6 cm^{-1}). This is because the 1223.1 cm^{-1} mode is a combination HCO/CCH bending vibration while the 1992.5 cm^{-1} band is an asymmetric CCC stretching vibration. The match between the observed and calculated peaks, given in Table 2-5, is quite good which

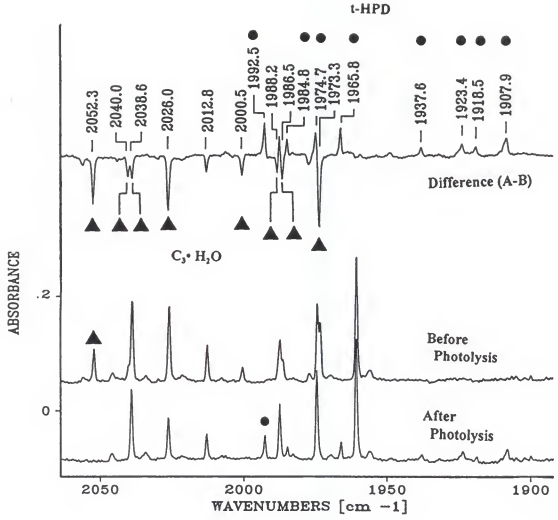

Figure 2-9. Portion of the 12K matrix infrared spectra of $^{12}C/^{13}C/Ar + H_2O$ (0.15%) ($[^{12}C]:[^{13}C]=1:2$) before photolysis and after 30 min of photolysis ($\lambda > 390$ nm). The negative peaks in the difference spectrum (triangles) are the asymmetric CCC stretches of the $^{12,13}C_3 \cdot H_2O$ complex isotopomers. The positive peaks (dots) are the asymmetric CCC stretches of the $^{12,13}C_3$-substituted trans-HPD isotopomers.

Table 2-5. Experimental and calculated (HF/6-31G*) IR frequencies (cm^{-1}) for all isotopomers of cis and trans-HPD for the most intense CCC asymmetric stretch, CCH+HCO bend (trans-HPD) and HCO bend + CO stretch (cis-HPD) modes.

Isotopmer	trans-HPD			cis-HPD		
	ν_{exp}	ν_{calc}	$\nu_{exp} - \nu_{calc}$	ν_{exp}	ν_{calc}	$\nu_{exp} - \nu_{calc}$
12-12-12-1-16-1	1992.5	1989.7 (0.99)[a,b]	+2.8	1999.6	2000.5 (1.00)[d]	-0.9
12-12-13-1-16-1	1984.8	1983.3 (0.95)	+1.5	1991.3	1992.5 (0.96)	-1.2
13-12-12-1-16-1	1974.7	1970.2 (1.00)	+4.5	1982.0	1982.7 (1.00)	-0.7
13-12-13-1-16-1	1965.8	1963.3 (0.96)	+2.5	1973.1	1973.9 (0.96)	-0.9
12-13-12-1-16-1	1937.6	1938.9 (0.95)	-1.3	1950.2	1950.4 (0.95)	-0.2
12-13-13-1-16-1	1923.4	1932.5 (0.91)	-9.1	1942.2	1942.0 (0.91)	+0.2
13-13-12-1-16-1	1918.5	1918.9 (0.96)	-0.4	1932.8	1932.3 (0.96)	+0.5
13-13-13-1-16-1	1907.9	1911.9 (0.92)	-4.0	1923.5	1922 (0.91)	+0.6
12-12-12-1-16-1	1223.1	1223.1 (0.85)[c,f]	0.0	1254.3	1254.3 (0.97)[e,f]	0.0
12-12-13-1-16-1	1220.2	1220.1 (0.97)	+0.1		1247.1 (0.73)	
13-12-12-1-16-1	1221.7	1221.9 (0.87)	-0.2		1254.2 (0.98)	
13-12-13-1-16-1	1218.6	1218.7 (0.99)	-0.1		1246.9 (0.75)	
12-13-12-1-16-1	1221.7	1222.4 (0.86)	-0.7		1253.7 (0.99)	
12-13-13-1-16-1	1218.9	1218.7 (0.97)	+0.2		1246.4 (0.74)	
13-13-12-1-16-1	1221.7	1221.2 (0.88)	+0.5		1253.7 (1.00)	
13-13-13-1-16-1	1217.6	1218.0 (1.00)	-0.4		1246.2 (0.77)	

[a] All frequencies for this mode scaled by 0.904.
[b] Normalized relative intensities in parenthesis.
[c] Scaled by 0.897.
[d] Scaled by 0.903.
[e] Scaled by 0.879.
[f] Due to the overlapped isotopomer bands, the assignment of the experimental frequencies for the CCH+HCO bend mode is tentative.

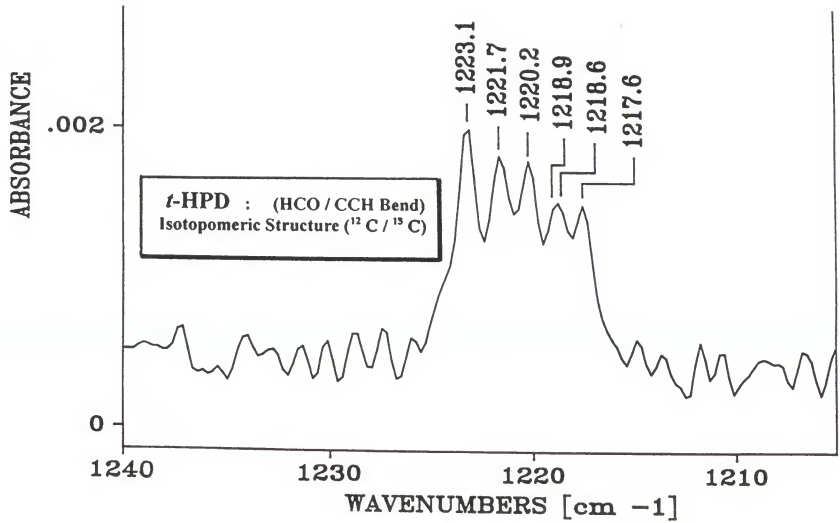

Figure 2-10. Portion of the 12K matrix infrared spectrum of $^{12}C/^{13}C/Ar + H_2O$ (0.15%) ($[^{12}C]:[^{13}C]=1:2$) after 30 min photolysis ($\lambda > 390$ nm). Isotopomeric bands are due to trans-HPD.

leads to the conclusion that the set of peaks at 1992.5, 1460.8, 1280.5, 1223.1, and 1016.3 cm^{-1} originate from trans-HPD.

The cis-HPD Isomer

Normally, photolysis of a matrix occurs just prior to a scan. Occasionally, however, photoproducts are produced whose lifetimes are so short that they are not observable under such an experimental protocol. Therefore scans were taken during photolysis. The matrix sample window was aligned at 45° to the photolysis beam and the IR probe beam. Figures 2-11 and 2-12 show the results of spectra taken during photolysis. Two new bands at 1999.6 and 1254.3 cm^{-1} grow in, while the five bands, attributable to trans-HPD, all decrease in parallel. With the photolysis light source off, the process is reversed. This strongly suggests a photolysis induced process, with spontaneous reversion in the dark. The species producing the 1999.6 and 1254.3 cm^{-1} bands will be shown to be cis-HPD.

LZP have predicted[40] that HPD can also exist in the cis form. Their calculations of the IR frequencies and intensities for cis-HPD, compared with this work, are given in Table 2-6. The most intense bands are predicted to lie at 1987.2 and 1279.8 cm^{-1}, the former about twice as intense as the latter. This is the same pattern observed for the two new bands at 1999.6 and 1254.3 cm^{-1}.

Further support for the attribution of these bands to cis-HPD comes from $^{12}C/^{13}C$ isotopic studies. Figure 2-13 gives the spectra of the $^{12}C/^{13}C$ isotopically substituted

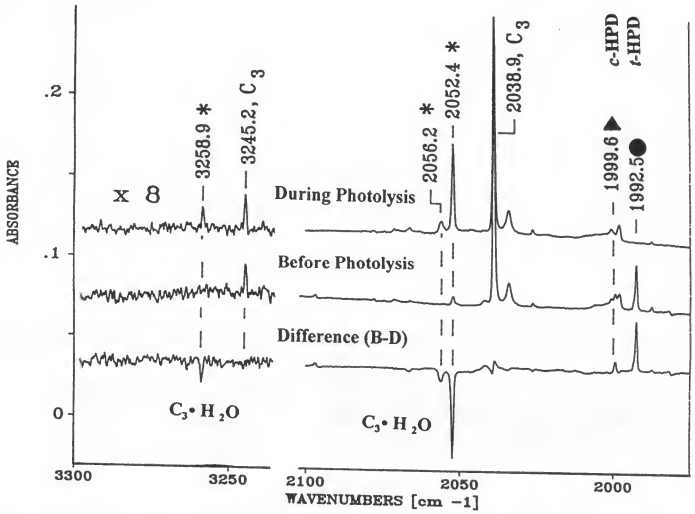

Figure 2-11. Portion of the 12K matrix infrared spectra of $^{12}C_n/Ar + H_2O$ (0.2%) before and after 30 min of photolysis ($\lambda > 390$ nm), but recorded during photolysis. The 3245.2 and 3258.9 cm^{-1} bands are the $\nu_1 + \nu_3$ combination bands in C_3 and the $C_3 \bullet H_2O$ complex.

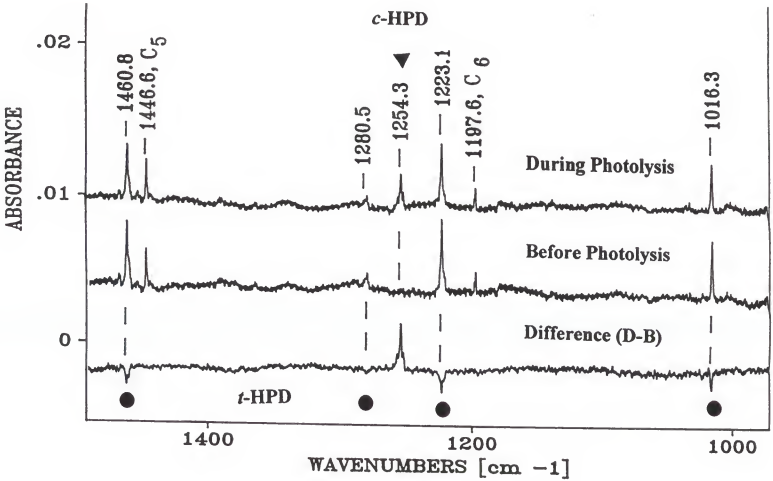

Figure 2-12. Portion of the 12K matrix infrared spectra of $^{12}C/^{13}C/Ar + H_2O$ (0.15%) ($[^{12}C]:[^{13}C]=1:2$ before photolysis and after 30 min photolysis ($\lambda > 390$ nm), but recorded during photolysis. The 1254.3 cm^{-1} band is the COH bend + CO stretch of cis-HPD.

Table 2-6. The experimental (Ar matrix) and calculated IR frequencies (cm^{-1}) and intensities (km/mol) for cis-3-hydroxypropadienylidene (cis-HPD) in its ground electronic state.

cis-HPD					
	HF/6-31G*		DZP+diffuse[b]		
ν_{exp}[c]	ν_{calc}[a]	Intensity[c]	ν_{calc}[b]	Intensity[c]	Mode Description
	3676.9	208.4 (0.19)	3714	221 (0.17)	OH str.
	3000.0	21.9 (0.02)	3020	17 (0.013)	CH str.
1999.6 (1.0)	1987.2	1120.0 (1.0)	1951	1284 (1.0)	CCC asym. str.
1254.3 (0.35)	1507.3	82.3 (0.07)	1495	116 (0.09)	COH bend, CH str.
	1279.8	494.9 (0.44)	1281	628 (0.49)	COH bend, CO str.
	1249.1	178.8 (0.16)	1240	104 (0.08)	HCO, CCH bend
	1011.5	2.2 (0.002)	1001	1 (0.001)	CC, CO str.
	968.3	2.2 (0.002)	956.3	2 (0.002)	CH wag
	592.3	13.1 (0.01)	594.5	15 (0.01)	HOCC, HOCH tor.
	489.5	116.2 (0.10)	494.0	106 (0.08)	CCO bend
	210.5	15.2 (0.01)	267.8	32 (0.02)	CCCO bend
	193.0	1.1 (0.001)	213.5	2 (0.002)	CCC bend

[a] Frequencies scaled by 0.897.
[b] From reference 40. Frequencies have been scaled by 0.9.
[c] Normalized relative intensities in parenthesis.

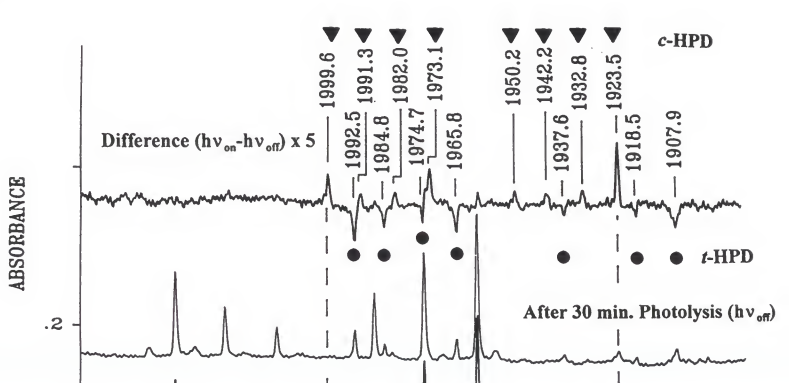

Figure 2-13. Portion of the 12K matrix infrared spectra of $^{12}C/^{13}C/Ar + H_2O$ (0.15%) ($[^{12}C]:[^{13}C]=1:2$) after 30 min of photolysis ($\lambda > 390$ nm) and recorded with the photolysis lamp on (bottom) and off (middle). The difference spectra (top) are shown the CCC asymmetric stretching modes of the isotopomers of cis-HPD (positive peaks) and trans-HPD (negative peaks).

species recorded with and without the photolysis lamp on. The difference spectrum shows the negative peaks of trans-HPD, beginning at 1992.5 cm^{-1} and stretching to 1907.9 cm^{-1}. Also shown is a set of eight positive peaks starting at 1999.6 cm^{-1} and ending at 1923.5 cm^{-1}, which are created as a result of photolysis. The negative peak due to trans-HPD at 1923.4 cm^{-1} is not seen in this spectrum due to overlap with the 1923.5 cm^{-1} isotopomer peak of cis-HPD. Table 2-5 lists the results of the *ab initio* calculations of the eight cis-HPD isotopomeric bands. Isotopomeric bands in the 1254.3 cm^{-1} region were searched for, and none were detected. Presumably this is due to the expected weak intensity.

HPD Isomer Interconversion

The process by which the two isomers interconvert can be investigated by focusing on similar vibrational modes in the two isomers and monitoring their intensity with time. First, the kinetic behavior is tracked by looking at the CCC asymmetric stretching modes. At long times after photolysis, the absorbance of the 1999.6 cm^{-1} cis-HPD band is a factor of 1.26×10^{-2} smaller than the absorbance of the 1992.6 cm^{-1} trans-HPD, which is at a maximum. The difference spectra ($A_t - A_\infty$) for both isomers as a function of time are plotted in Figure 2-14. The positive peak (1999.6 cm^{-1}, cis-HPD) is at a maximum at the photolysis cutoff of $t = 0$, and decreases with time. The negative peak (1992.6 cm^{-1}, trans-HPD) is at a minimum at $t = 0$ and increases to a maximum at $t = \infty$. (An increasing absorbance will appear as a negative peak decreasing in amplitude with time.) The fact that the integral intensity of the 1999.6 cm^{-1} (cis-HPD) positive peak is approximately

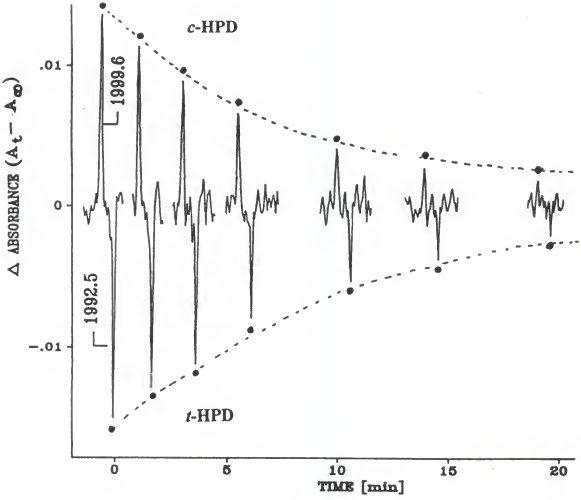

Figure 2-14. Time dependence of the difference spectrum (A_t - A_∞). The t = 0 and subsequent plots were scanned after the photolysis lamp was turned off. Each spectrum was recorded for ca. 10 sec, with A_∞ scanned after 2 hr. The 1992.5 cm^{-1} (trans-HPD) band is at maximum absorbance at t = 2 hr, at which time the 1999.6 cm^{-1} (cis-HPD) band is at its minimum absorbance.

equal to the integral intensity of the 1992.6 cm^{-1} (trans-HPD) negative peak indicates that the product of the concentration and the transition strength for this mode is about the same for both cis and trans isomers. Table 2-6 shows that calculations predict the same transition strength of the CCC asymmetric stretch for both isomers.

Next, the behavior of the combined COH bend/CO stretch modes in the two isomers is investigated. The difference spectrum shows that the integral intensity of the 1254.3 cm^{-1} band (cis-HPD) is approximately twice as intense as the 1223.1 cm^{-1} band (trans-HPD), if one assumes that the concentration changes $\{\Delta[\text{cis-HPD}] = \Delta[\text{trans-HPD}]\}$ in the light induced process are the same for both isomers. The latter is a reasonable assumption if the isomers interconvert and are not formed by any other process. Both calculations predicted that this mode in cis-HPD should be approximately twice as intense as in trans-HPD. The theoretical calculations predict both intensities and frequencies for the two HPD isomers reasonably well.

The dark reaction relaxation time and (crudely) its temperature dependence may be determined by using the data in Figure 2-14. Both data sets were fit to the first-order expression

$$[A_t - A_\infty] = [A_t - A_\infty] \exp(-t / \tau),$$

where τ is the relaxation (appearance or disappearance) time for either isomer. If one isomer converts directly into the other, the relaxation times should be the same for both. Figure 2-15 shows the plot of $\ln |A_t - A_\infty|$ vs. time for both isomers at two different matrix

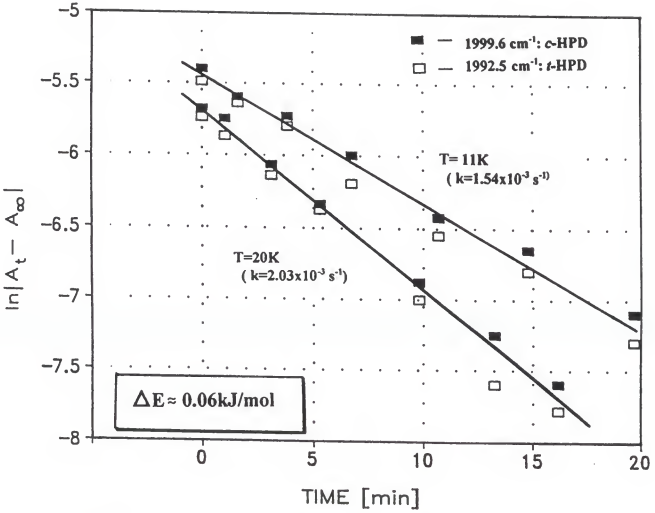

Figure 2-15. Dependence of $\ln|A_t - A_\infty|$ vs. time after 30 min of photolysis ($\lambda > 390$ nm) of the $^{12}C_n/Ar + H_2O$ (0.15%) matrix for T = 11 and 20K. The A_t and A_∞ absorbances are identical to the ones shown in Figure 2-14.

temperatures. The slopes (= $-1/\tau$) at a given temperature are the same for each isomer. Hence, it can be concluded that the cis-HPD conformer relaxes completely to trans-HPD with a relaxation time of τ = 10.8 min ($k = 1.54 \times 10^{-3}$ s^{-1}) at 11K and τ = 8.2 min ($k = 2.03 \times 10^{-3}$ s^{-1}) at 20K.

Although higher temperature measurements were attempted, aggregation of the carbon clusters interferes at temperatures higher than 20K.[41] In addition, other reaction channels, probably different for the two isomers, open up. We observed different values for the relaxation times for the two isomers at higher temperatures. In addition, we found that the 1999.6 cm^{-1} (cis-HPD) peak of $(A_t - A_\infty)$ was more intense than the 1992.6 cm^{-1} (trans-HPD) peak at elevated temperatures.

Despite this difficulty, it is possible to obtain a rough estimate of the activation barrier for the cis to trans-HPD isomerization from the 11K and 20K runs. Using

$$\ln k = -\frac{\Delta E_a}{RT} + \ln A$$

we find $\Delta E_a = 0.06 \pm 0.02$ kJ/mol and $A = 2.84 \times 10^{-3}$ s^{-1}. This very small value leads to the question of whether there is a barrier at all. This value is equivalent to ca. 5 cm^{-1}. This is compared to the calculated barrier of 34.7 kJ/mol (2900 cm^{-1}). There are two possible explanations for such a low value. First, it could simply represent a lower bound on the activation energy since the energies used in the IR probe beam in this experiment (7000-700 cm^{-1}) are much greater than this value. Or, the process involved in the conversion could involve hydrogen tunneling. (OHMK reported that photolysis

experiments involving a $C_3 \bullet D_2O$ complex were slow and required four times as long as the $C_3 \bullet H_2O$ complex.)[37]

The difference in stabilization energies for the two isomers may be determined from the intensity distribution of their CCC asymmetric stretching vibrations. At long times after the photolysis is terminated, the 1992.6 cm^{-1} band is about 79 times more intense than the 1999.6 cm^{-1} band. Taking the integral intensities of these two bands to be equal, the equilibrium constant for the two isomers at 11K is

$$K_{11K} = \frac{[cis\text{-}HPD]}{[trans\text{-}HPD]} = 1.2X10^{-2}.$$

From this value the standard free energy difference for the two isomers can be obtained from the expression

$$\Delta G_{11K}^{\circ} = -RT \ln K_{11K} = 0.4 \pm 0.15 \text{ kJ/mol},$$

where ΔG_{11K}° is the standard free energy difference between cis-HPD and trans-HPD isomers in equilibrium in an Ar matrix. Figure 2-16 shows a schematic diagram of the potential energy curve involved in the isomerization process. The cis isomer is less stable than the trans. The experimental value of 0.4 kJ/mol is comparable to the standard free energy difference of 0.12 kJ/mol for the two hydroxy isomers of amino-hydroxy-9-methylguanine in Ar at 12K.[63] It may be compared also with the theoretical value of the internal energy difference between the two isomers. LZP in their *ab initio* studies[40] of the

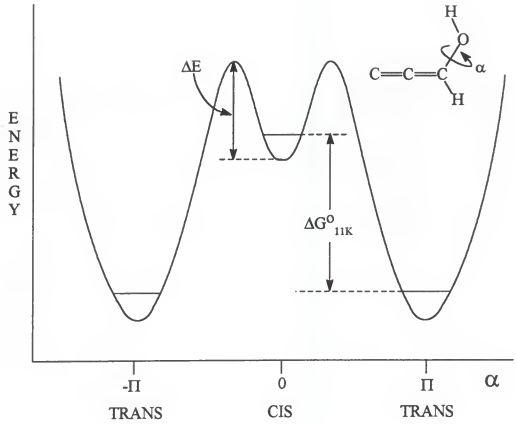

Figure 2-16. Potential energy surface for the rotation of the H atom about the C-O bond of HPD in its ground electronic state. See text for ΔE and ΔG^{o} values.

HPD products predicted that the cis form should lie about 23.4 kJ/mol above the trans form. This calculated difference in stabilization energies is practically independent of method; RHF, MP2, MP3, or MP4(SD) give the same results to $\pm$ 1.3 kJ/mol and are very different from the experimental value. While the matrix is expected to influence this value somewhat, this large discrepancy suggests the possibility of a different mechanism involved in the conversion process.

LZP also located the transition state for the isomerization of cis to trans-HPD. They calculated that the energy of the transition state lies 46 kJ/mol above the cis singlet ground state (MP2/DZP level). The almost negligible value of 0.06 kJ/mol for the activation barrier we find here is also very different from the calculated one. As LZP point out, the interconversion could be occurring via hydrogen tunneling, for which there should be no activation barrier.

Discussion

Our observations may be significant with respect to the mechanisms of chemical reaction in the interstellar medium. Both C_3O and propynal, the final products of photolysis of the $C_3 \cdot H_2O$ complex, have been observed[64,65] in almost equal abundance in the cold (10K) molecular cloud, TMC-1. Herbst, Smith, and Adams have postulated[66] that the following ion-molecule reactions are the principal pathways of formation for C_3O and H_2C_3O:

$$C_2H_2^- + CO \rightarrow H_2C_3O^+ + h\nu \quad (1a)$$

$$H_2C_3O^- + e^- \rightarrow C_3O + H_2 \quad (1b)$$

$$\rightarrow HC_3O + H \quad (1c)$$

and

$$C_2H_3^- + CO \rightarrow H_3C_3O^+ + h\nu \quad (2a)$$

$$H_3C_3O^+ + e^- \rightarrow C_3O + H_2 + H \quad (2b)$$

$$\rightarrow H_2C_3O + H \quad (2c)$$

On the other hand, Brown and coworkers have suggested[67] that the most important pathway for C_3O production is:

$$O + C_4 \rightarrow C_3O + C \quad (3a)$$

$$\rightarrow C_3 + CO \quad (3b)$$

The estimates by Brown and coworkers[67] and by Herbst and Leung[68] for the formation of C_3O are in good agreement with observations. Irvine *et al.* point out[65] that, although the branching ratio in (2) is not known from laboratory studies, the fact that nearly equal abundances of C_3O and propynal are observed, must mean that (2c) is a significant reaction pathway.

Results presented here suggest a different mechanism. As we have shown, the $C_3 \bullet H_2O$ complex readily forms in low temperature environments and, when photolyzed, forms the intermediates, cis and trans-HPD. Further photolysis results in C_3O and

propynal formation. Desorption from the surface of the dust particles could then take place by any of the mechanisms proposed by others previously.[69] The matrix environment used in our studies is obviously different from that of dust particles, but the conditions of low temperature and exposure to visible and/or ultraviolet radiation are common to both. The low activation energy measured for cis to trans isomerization of HPD might suggest that hydrogen tunneling is present. Herbst has recently proposed[70] that hydrogen tunneling could be a viable low temperature process for the reaction between neutral species of astrophysical importance.

Summary

In this chapter the existence of a complex between C_3 and H_2O in an Ar matrix has been confirmed via $^{12}C/^{13}C$ isotopic labeling studies using FTIR spectroscopy in conjunction with *ab initio* calculations. IR frequencies attributable to the complex have been observed at 2052.3 (asym. CCC str.), 3598 (OH sym. str.), 3712.2 (OH asym. str.), 1593.4 (HOH bend), and 1214.3 cm^{-1} (CC sym. str.). An electronic band at 405.4 nm is assigned to the perturbed $^1\Pi \leftarrow {}^1\Sigma$ transition of the C_3 portion of the complex. The ground state geometry of the complex is determined to be planar with one hydrogen of the H_2O weakly bound to a terminal C of the C_3 with an intermoiety angle of 175°.

Photolysis of the $C_3 \bullet H_2O$ complex results in the formation of C_3O and cis and trans 3-hydroxypropadienylidene (HPD). IR peaks assigned to trans-HPD have been observed at 1992.5, 1460.8, 1280.5, 1223.1, and 1016.3 cm^{-1}. Further photolysis of trans-HPD

results in isomerization to cis-HPD, which exhibits IR bands at 1999.6 and 1254.3 cm^{-1}. Two sets of eight $^{12}C/^{13}C$ isotopomeric bands have ben observed for the intense 1992.5 cm^{-1} trans-HPD and 1999.6 cm^{-1} cis-HPD asymmetric CCC stretching modes. All observed bands are shown to match *ab initio* values reasonably well.

The dark relaxation rate of cis-HPD to trans-HPD has been found to be $1.54x10^{-3}$ s^{-1} at 11K and $2.03x10^{-3}$ s^{-1} at 20K. A lower limit for the activation energy of this process has been established as approximately 0.06 kJ/mol. In addition, the difference in standard free energies of the two isomers has been determined to be 0.4 kJ/mol. Both of these values are much smaller than theoretical estimates. This finding may be of importance for other chemical reactions which occur in the interstellar medium. Indeed, the mechanism for propynal formation in these experiments could be a viable method of propynal formation in interstellar dust clouds.

CHAPTER 3
THE C_3H_2O POTENTIAL SURFACE

Introduction

Over one hundred molecular species exist in the interstellar medium.[71] Two of these, propynal and C_3O, have been observed in approximately equal abundances in the molecular cloud TMC-1.[65,67,72] The mechanisms by which these species are formed has been the topic of widespread interest. Herbst, Smith, and Adams postulated[66] that they are formed via ion-molecule reactions involving the radiative association processes:

$$C_2H_2^+ + CO \rightarrow H_2C_3O^+ + h\nu$$

$$C_2H_3^+ + CO \rightarrow H_3C_3O^+ + h\nu$$

followed by the dissociative electron recombination processes:

$$H_2C_3O^+ + e^- \rightarrow C_3O + H_2$$

$$\rightarrow C_3O + H_2$$

$$H_3C_3O^+ + e^- \rightarrow H_2C_3O + H_2 + H$$

$$\rightarrow H_2C_3O + H$$

Alternatively, Brown and coworkers have proposed[65] that the most important pathway for C_3O production in "young" interstellar clouds (~10^6 years) is reaction of atomic oxygen with C_4:

$$O + C_4 \rightarrow C_3O + C$$

$$\rightarrow C_3 + CO$$

These suggestions have now been investigated experimentally[73] and theoretically[74] by researchers in New Zealand. Petrie, Bettens, Freeman, and McEwan measured[73] rate coefficients and product distributions for the gas phase reaction of $H_nC_3O^+$ (n = 0-3) and $C_3O_2^+$ with a number of neutral species including H_2O using the selected ion flow tube (SIFT) technique. They concluded that $H_nC_3O^+$ ions were notably unreactive toward the major known neutral constituents of interstellar clouds. Very recently, Maclagan, McEwan, and Scott reported[74] *ab initio* G2 level calculations and showed that the reaction of $C_2H_3^+$ and CO yields C_2-protonated propadienone rather than O-protonated propynal. They concluded that while this species could form neutral propadieneone via dissociative electron recombination, propynal could not be formed in a similar manner. However, the amount of internal energy available after electron recombination should be sufficient to make other unimolecular dissociation channels available.

In this study a different mechanism, which is initiated by the formation of a complex between the carbon cluster, C_3, and water, is examined. In an important study Ortman, Hauge, Margrave, and Kafafi were the first to report[37] evidence for a complex between C_3 and H_2O in an argon matrix at 12K. When photolyzed with radiation of $\lambda \geq 400$nm, the

complex was shown to rearrange to C_3O, propynal, and a third compound postulated to be hydroxyethynylcarbene (HEC, **J**). Further photolysis with radiation between $280 \geq \lambda \geq 360$ nm caused the third compound's bands to decrease and those due to propynal to increase. No new photoproducts were noted. Later, Liu, Zhou, and Pulay (LZP) reported[40] a comprehensive *ab initio* theoretical study of the expected infrared spectral bands of HEC and an alternate intermediate, 3-hydroxypropadienylidene (HPD, **B** and **C**). By comparison with the calculated experimental spectra, LZP proposed that **B** and not **J**, was responsible for the intermediate bands.

In Chapter 2 it was shown from $^{12}C/^{13}C$ isotopic studies that the intermediate was indeed **B**.[75] It was also shown that further photolysis of **B** led to propynal. It was suggested that small carbon clusters such as C_3 could complex with H_2O on the icy mantles of small dust grains prevalent in interstellar clouds, and upon photolysis lead to the formation of propynal. This solid state mechanism is very different from the gas phase one proposed by Herbst and coworkers[66] and by Brown and coworkers.[65]

Given the conclusions reached by the New Zealand researchers on the unlikelihood of the ion-molecule reaction route to propynal in the interstellar medium and the apparent ease of formation of propynal and C_3O from the photolysis of solid state $C_3 \bullet H_2O$ complexes, this chapter will present the theoretical investigation of the entire C_3H_2O potential surface. The study in Chapter 2 was limited primarily to the $C_3 \bullet H_2O$ complex and the HPD intermediates **B** and **C**. From that study several questions arose. (1) Given the photolytic conditions and the number of C_3H_2O isomers available, why were the HPD intermediates (**B** and **C**), propynal (**O**) and C_3O observed? (2) Why is propynal

apparently not photodepleted? (3) Two other C_3H_2O isomers, cyclopropenone (**R**) and propadienone (**S**), are known to be very stable. Why are neither seen experimentally?

Theoretical

All calculations were carried out using the GAUSSIAN 92 program package.[42] All structures presented here are in their singlet ground states. Geometries were optimized initially at the HF/6-31G* level. Then, to gauge the effects of electron correlation, single point calculations at the QCISD(T)/6-31G* level were run on the HF optimized geometries. The HF structures were then used as starting points for optimization at the MP2/6-31G* level. Unless otherwise specified, the discussion in the following sections is restricted exclusively to the surface at the higher MP2/6-31G* level of theory. Vibrational frequencies for all HF and MP2 points were performed at their respective levels in order to characterize the nature of the stationary points. In all cases the intrinsic reaction coordinate (IRC) utility was employed to confirm that the transition state did indeed connect to the correct minima. Each minima is connected to one or more other minima through a transition state in which either one hydrogen atom migrates to an adjacent heavy atom or a bond between heavy atoms (i.e., C and O) either forms or breaks. There are, however, three exceptions to this rule. TS1, which involves carbon inserting into a water OH bond, and TS14 and TS15 which are concerned with the unimolecular dissociation of **R** and **S** respectively into acetylene and CO. Transition states between conformers were not investigated.

Results

The structures of all intermediates and stable compounds studied in this work are shown in Figure 3-1. Table 3-1 lists the total energies, relative energies, and zero-point energies of each minimum at the HF/6-31G* and QCISD(T)/6-31G*//HF/6-31G* levels, while Table 3-2 gives similar quantities for the corresponding transition states. Tables 3-3 and 3-4 give the equivalent values from the MP2/6-31G* level calculations. Figures 3-2 to 3-4 show these energies schematically as potential surfaces. The HF/6-31G* surface is complete, incorporating all transition states and isomers (except for **G**, which is predicted to be unstable at all levels of theory). The MP2 optimized minima are shown in Figure 3-5. Several of the minima and transition states studied were found to be unstable at the MP2/6-31G* level of theory. In each case they followed a CCC ring cyclization path, optimizing to another structure. Both isomers **E** and **F** optimized to **H**, while **G** optimized to **I**. And, the very stable cyclopropenone molecule (**R**) was formed from the unstable isomer **P**.

The transition state structures between the minima are indicative of the probable mechanism of interconversion. Figure 3-6 shows the geometries of the MP2 optimized transition states. All transition states represent adiabatic barriers which are the minimum energies necessary to promote isomerization. Five transition states-TS4, TS5, TS7, TS12 and TS13-found at the HF level could not be located at the MP2 level, and are presumed not to exist. This has serious consequences for the shape and content of the potential surface. The absence of these transition states eliminates isomers **H** and **N** from the MP2

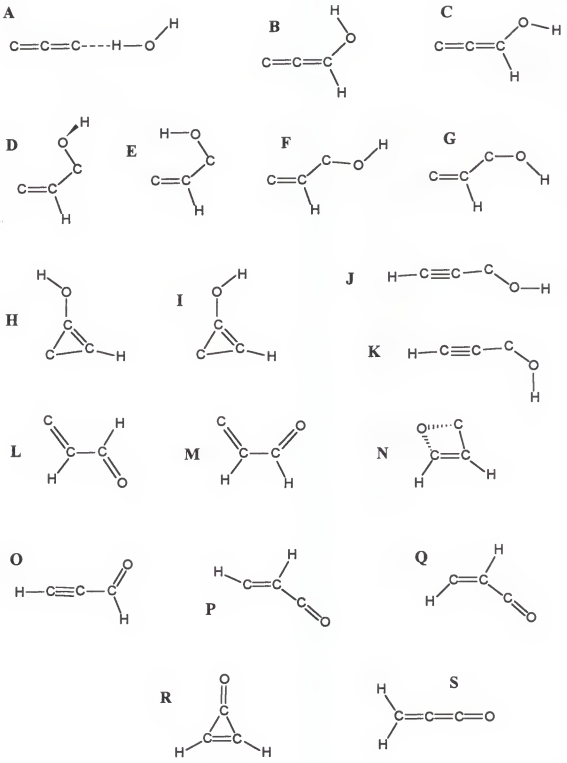

Figure 3-1. Unoptimized structures of C_3H_2O isomers studied.

Table 3-1. Total energies (hartrees), zero-point corrected relative energies[a] (kcal/mol), and zero-point energies (kcal/mol) of all minima calculated at the HF/6-31G* level. Total energy (hartrees) calculated at the QCISD(T)/6-31G*//HF/6-31G* level. HF/6-31G* calculated zero-point corrections scaled by 0.90.

Isomer	Sym	HF/6-31G*	Relative Energy	QCISD(T)/6-31G*	Relative Energy	Z.P.E
A	C_s	-189.369 60	0.0	-189.946 83	0.0	21.1
B	C_s	-189.465 66	-55.9	-190.044 28	-56.9	25.9
C	C_s	-189.456 91	-50.6	-190.036 25	-52.0	25.7
D	C_1	-189.406 15	-20.3	-189.972 95	-13.8	24.0
E	C_1	-189.397 22	-14.8	-189.948 54	-11.1	23.9
F	C_s	-189.411 28	-23.4	-189.973 27	-13.9	24.1
G[b]						
H	C_s	-189.485 80	-69.3	-190.055 43	-64.5	26.1
I	C_s	-189.482 23	-66.2	-190.051 95	-61.5	26.0
J	C_s	-189.465 45	-56.3	-190.041 94	-55.9	25.3
K	C_s	-189.459 86	-53.0	-190.037 74	-53.4	25.1
L	C_s	-189.486 53	-70.5	-190.056 61	-66.0	24.3
M	C_s	-189.483 75	-68.7	-190.053 12	-63.8	24.3
N	C_1	-189.438 69	-39.8	-190.025 56	-45.9	25.0
O	C_s	-189.541 11	-103.5	-190.123 07	-106.5	25.7
P	C_s	-189.495 84	-76.1	-190.066 06	-71.7	24.5
Q	C_s	-189.490 72	-72.9	-190.067 85	-72.8	24.5
R	C_{2v}	-189.533 98	-98.8	-190.114 14	-100.7	25.9
S	C_{2v}	-189.536 25	-101.0	-190.122 46	-106.6	25.1
CO	$C_{\infty v}$	-112.737 88		-113.036 12		3.5
C_2H_2	$D_{\infty h}$	-76.817 83		-77.091 83		18.5

[a] Energy relative to the $C_3 \cdot H_2O$ complex. [b] Not predicted to exist at the HF/6-31G* level.

Table 3-2. Total energies (hartrees), zero-point corrected relative energies[a] (kcal/mol), and zero-point energies (kcal/mol) of each transition state at the HF/6-31G* level. Total energy (hartrees) calculated at the QCISD(T)/6-31G*//HF/6-31G* level. HF/6-31G*calculated zero-point corrections scaled by 0.90.

	Sym	HF/6-31G*	Relative Energy	QCISD(T)/6-31G*	Relative Energy	Z.P.E.
TS1	C_1	-189.285 27	53.8	-189.892 84	34.7	20.1
TS2	C_1	-189.318 51	32.0	-189.912 04	21.7	21.3
TS3	C_1	-189.395 85	-15.2	-189.966 93	-11.4	22.4
TS4	C_s	-189.326 29	28.2	-189.916 97	19.7	20.0
TS5	C_s	-189.387 59	-8.9	-189.976 07	-16.0	23.7
TS6	C_s	-189.461 04	-56.6	-190.044 01	-60.2	22.0
TS7	C_s	-189.377 31	-2.6	-189.964 20	-8.7	23.5
TS8	C_s	-189.379 95	-6.2	-189.983 08	-22.4	21.4
TS9	C_s	-189.416 24	-29.3	-190.006 30	-37.3	21.0
TS10	C_s	-189.491 96	-75.2	-190.074 19	-77.3	24.0
TS11	C_s	-189.394 43	-15.6	-189.988 37	-26.1	21.2
TS12	C_1	-189.435 81	-38.6	-190.025 64	-46.4	24.4
TS13	C_1	-189.386 35	-9.5	-189.950 22	-1.1	22.2
TS14	C_s	-189.459 18	-54.9	-190.045 62	-60.7	22.5
TS15	C_s	-189.489 78	-73.9	-190.065 96	-73.2	22.7

[a] Energy relative to the C_3•H_2O complex.

Table 3-3. Total energies (hartrees), zero-point corrected relative energies[a] (kcal/mol), and zero-point energies (kcal/mol) of minima calculated at the MP2/6-31G*level. MP2/6-31G* calculated zero-point corrections scaled by 0.95.

Isomer	MP2/6-31G*	Relative Energy	Z.P.E.
A	-189.895 21	0.0	19.9
B	-189.997 78	-60.2	24.2
C	-189.988 86	-54.7	24.1
D	-189.913 79	-9.4	22.3
E[b]			
F[b]			
G[c]			
H	-190.014 95	-70.9	24.3
I	-190.011 32	-68.7	24.2
J	-189.997 71	-64.3	23.1
K	-189.993 01	-58.6	22.7
L	-190.004 76	-66.4	22.3
M	-190.001 51	-64.5	22.2
N	-189.983 80	-52.2	23.5
O	-190.086 63	-117.1	23.1
P[d]			
Q	-190.024 58	-78.2	23.1
R	-190.077 69	-110.7	23.9
S	-190.086 31	-116.2	23.8
C_2H_2	-77.066 79		16.1
CO	-113.021 21		3.0

[a] Energy relative to the $C_3 \bullet H_2O$ complex. [b] Not predicted to exist. Reverts to structure **H**. [c] Not predicted to exist. Reverts to structure **I**. [d] Not predicted to exist. Reverts to structure **R**.

Table 3-4. Total energies (hartrees), zero-point corrected relative energies[a] (kcal/mol), and zero-point energies (kcal/mol) for all transition states found at the MP2/6-31G* level. MP2/6-31G* calculated zero-point corrections scaled by 0.95.

	MP2/6-31G*	Relative Energy	Z.P.E.
TS1	-189.848 43	30.7	18.4
TS2	-189.858 92	23.3	19.3
TS3	-189.905 82	-5.5	21.0
TS4[b]			
TS5[b]			
TS6	-190.001 45	-66.0	20.5
TS7[b]			
TS8	-189.946 22	-32.5	19.4
TS9	-189.953 58	-36.6	19.8
TS10	-190.021 03	-76.3	22.6
TS11	-189.957 66	-39.4	19.7
TS12[b]			
TS13[b]			
TS14	-190.005 41	-67.3	21.8
TS15	-190.009 10	-71.4	19.9

[a] Energies relative to the $C_3 \bullet H_2O$ complex. [b] Stationary point not found at the MP2/6-31G* level.

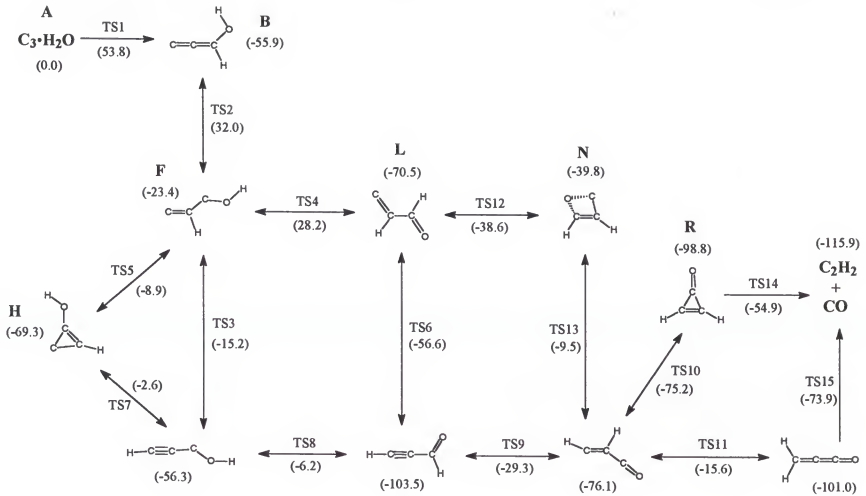

Figure 3-2. The HF/6-31G* calculated potential surface. Only lowest energy isomers are shown. Zero-point corrected energies (kcal/mol) relative to A in parentheses.

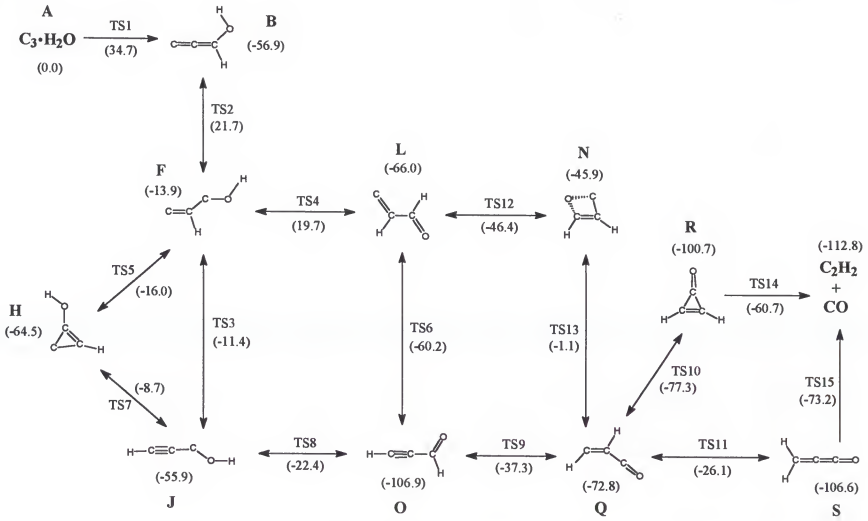

Figure 3-3. The QCISD(T)/6-31G*//HF/6-31G* calculated potential surface. Only lowest energy isomers are shown. Zero-point corrected energies (kcal/mol) relative to **A** in parentheses.

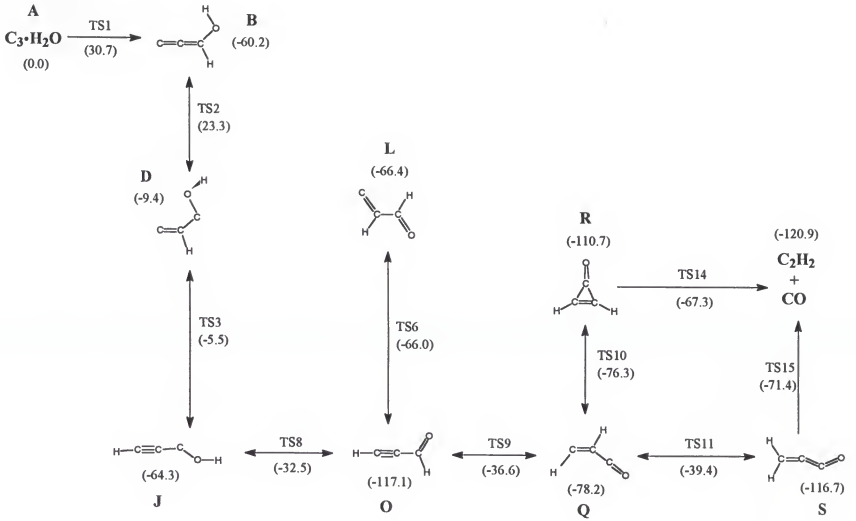

Figure 3-4. The MP2/6-31G* calculated potential surface. Only lowest energy isomers are shown. Zero-point corrected energies (kcal/mol) relative to **A** in parentheses.

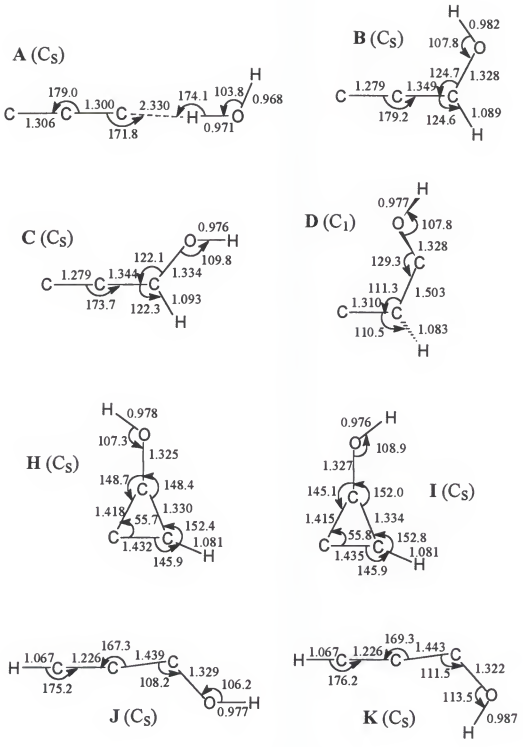

Figure 3-5. Optimized structures of all minima found at the MP2/6-31G* level of theory.

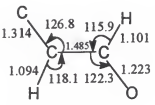

L (C_S)

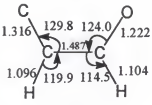

M (C_S)

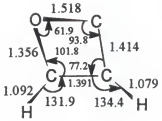

N (C_1)

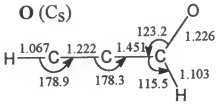

O (C_S)

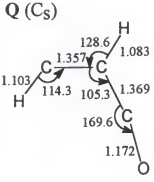

Q (C_S)

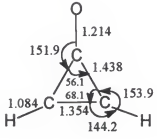

R (C_2v)

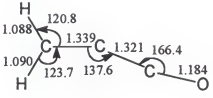

S (C_S)

Figure 3-5 continued. Optimized structures of all minima found at the MP2/6-31G* level of theory

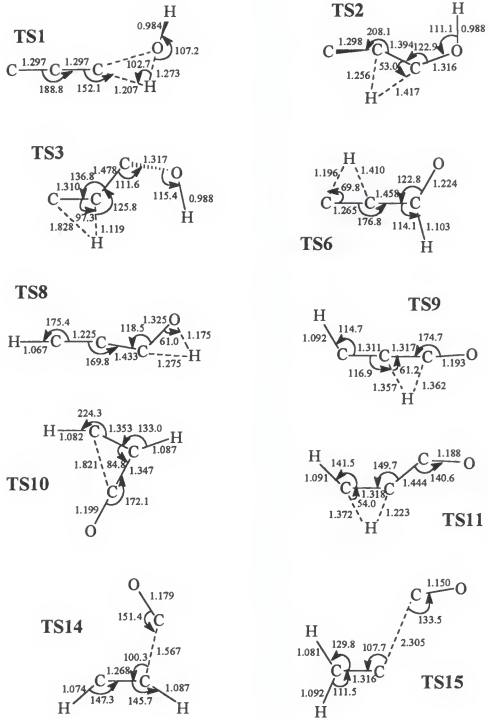

Figure 3-6. Optimized structures of all transition structures found at the MP2/6-31G* level of theory.

surface, but more importantly it forces the production of cyclopropenone (**R**) and propadienone (**S**) to proceed through propynal (**O**). And, if propynal is indeed a trap, **R** and **S** will not be seen experimentally.

Discussion

An understanding of the photochemical transformation of the $C_3 \bullet H_2O$ complex to propynal (and beyond) is greatly aided by consideration of the calculated MP2 potential surface. The $C_3 \bullet H_2O$ complex (**A**) has been studied experimentally[37,75] and theoretically in detail previously.[40,75] There exists a large barrier (TS1) to the formation of the HPD intermediates **B** and **C** which is calculated to be 52 kcal/mol at the HF level, 33.8 kcal/mol at the QCISD(T) level, and 29.3 kcal/mol at the MP2 level. Clearly, this barrier prevents the immediate reaction of C_3 and water, as observed for atomic carbon and water.[38] There is a large discrepancy between the calculated barrier for TS1 and the photolysis wavelength ($\lambda \leq 400$ nm) necessary to promote reaction. This can be explained by the fact that going from **A** to **B** and **C** proceeds through an excited electronic state. In fact, there is no reaction until the $^1\Pi_u \leftarrow {}^1\Sigma_g^+$ electronic transition in C_3 at 405 nm is excited. The trans or cis-HPD intermediates have been observed experimentally[75] which indicates that there are barriers sufficiently large to preclude their immediate photochemical destruction. Ortman *et al.* showed[37] that radiation between 320 and 380 nm does not deplete the intermediate **B**, but radiation between 280 and 360 nm does. Thus, the energy necessary to destroy HPD must lie between 280 to 320 nm (89 and 102 kcal/mol). The former limit

matches well the MP2 barrier of 87.0 kcal/mol from **B** to the transition state TS2. Radiation with $\lambda \leq 400$ nm (71.5 kcal/mol) used to photolyze the $C_3 \bullet H_2O$ complex to **B** and **C**, is not sufficiently energetic to continue photoconversion over TS2. However, light in the 280-320 nm range is. This would explain why the HPD isomers (**B**, **C**) are seen experimentally.

The computed surface from **B** through intermediates **D** and **J** to propynal (**O**) involves three consecutive H atom migrations along the CCCO framework. Transition state TS2 shows that the migration involves formation of a three-membered ring with H bridging two adjacent carbons in the chain. TS3 involves a similar structure as the H migrates further down the chain. Finally, TS8, leading from **J** to **O**, involves the migration of the hydroxy hydrogen to the adjacent carbon. Once photoconversion from **B** or **C** to **D** occurs, the remaining barriers to propynal formation are relatively small (30 to 40 kcal/mol range) and easily surmounted by photons in the 280-320 nm range.

Propynal is predicted to be the global minimum of the C_3H_2O surface at the MP2 level of theory (117.1 kcal/mol more stable than the $C_3 \bullet H_2O$ complex). It is pertinent to ask whether propynal can act as a photochemical 'dead end' or if it is possible to deplete it during photolysis to produce other photoproducts? The three calculated barriers which deplete propynal (TS6, TS8, and TS9) are in the 80 to 90 kcal/mol range. Radiation with $\lambda \sim 320$ nm (89 kcal/mol) is sufficient to scale all three barriers. Thus, propynal is predicted to be depleted slowly by continuous irradiation at 320 nm or below, and this depletion is in fact seen experimentally (*vide infra*).

The destruction of propynal implies that one or more of the C_3H_2O isomers, especially **R** (cyclopropenone) or **S** (propadienone), could be formed. Propynal (**O**), cyclopropenone (**R**), and propadienone (**S**) are the most stable C_3H_2O isomers. A few C_3H_2O isomers have been investigated by Radom and coworkers.[76-78] The order of stability found by Komornicki, Dykstra, Vincent, and Radom[78] is also found here. At the HF level propynal is predicted to be more stable than propadienone by 3.0 kcal/mol and cyclopropenone by 4.5 kcal/mol. At the MP2 level, the order remains the same but with propynal now predicted to be more stable than propadienone by just 0.2 kcal/mol and cyclopropenone by 5.6 kcal/mol. The relative order of these three isomers found by Maclagan, McEwan, and Scott[74] at the very sophisticated G2 level finds propadienone (**S**) to be more stable than propynal (**O**) by 1.6 kcal/mol and cyclopropenone (**R**) by 8.4 kcal/mol.

The barriers to formation of the isomers propadienone and cyclopropadienone from **Q** and the subsequent barriers to dissociation into acetylene and CO are smaller than the photolysis energy used experimentally. The MP2 barrier from **Q** to propadienone (**S**) is 42 kcal/mol via TS11, while the barrier from **Q** to cyclopropenone (**R**) is only 2.3 kcal/mol via TS10. From **R** to C_2H_2 and CO requires 45.4 kcal/mol energy input, whereas the decomposition of **S** via TS15 requires 46.6 kcal/mol. The latter pathway would yield vinylidene (H_2CC) and CO initially, but the vinylidene to acetylene rearrangement barrier[†]

[†] An upper bound to the vinylidene zero point level of 15 525 cm^{-1} above acetylene has been reported by Chen, Y.; Jonas, D. M.; Kinsey, J. J. L.; Field, R. W. *J. Chem. Phys.* **91**, *3976*, 1989; but the isomerization barrier between the two isomers has yet to be measured.

is calculated to require only 8.6 kcal/mol of activation energy.[79,80] These results are consistent with previously reported observations that the photofragmentation of propadienone leads to acetylene and CO.[81-83]

From the presently computed surface the expectation is that, once formed, propynal may be depleted slowly by crossing one or more of the transition states TS3 to 13 upon photolysis. It appears likely that **R** and **S** should be formed and subsequently decomposed to form acetylene and CO. Searching for evidence on the validity of this mechanism, previous photochemical infrared data for evidence of CO and/or acetylene were re-examined. Ortman *et al.* reported[37] IR bands for both, but stated that CO was present in their experiments as a trace gas and that acetylene was formed from the reaction of C_2 and residual H_2 from the cracking of pump oil on hot surfaces or outgassing of the graphite sample. Our results, given in Figure 3-7, show that neither CO (2138 cm^{-1}) nor acetylene (736 cm^{-1}) bands are present in our unphotolyzed sample of C_n in Ar (with 0.15% H_2O). However, after photolysis with a water filter, bands due to CO, acetylene, and propynal (2108 cm^{-1}) are present (*cf.* Figure 3-8). In addition, new unassigned bands at 2148.7, 2145.9, and 743.9 cm^{-1} are also seen. In an identical experiment with no water filter and longer photolysis times, no propynal peak was found, but peaks due to acetylene and CO are present. The conclusion arrived at from this evidence is that CO and acetylene are the final products of the photolysis of the $C_3 \bullet H_2O$ complex, and that propynal is not a photochemical 'dead-end'. Propynal itself is slowly depleted by photolysis eventually yielding CO and acetylene. Evidence for the existence of **R** and **S** has not been found in either the matrix experiments or to date in the interstellar medium. To aid in their

identification, calculated rotational constants and IR frequencies at the MP2 level are given in Tables 3-5 and 3-6, respectively, for all the C_3H_2O isomers studied here.

The major species discussed here-propynal, acetylene, CO, C_3, and H_2O-are all constituents of the interstellar medium.[71] It is hypothesized that propynal may be formed from the photolysis of the $C_3 \bullet H_2O$ complex. This complex could be present in the icy mantles of small dust grains in the interstellar medium. Other molecules are suspected to originate in a similar manner on dust grains.[84-86] There is evidence for C_3 in the mantles of dust grains near the protostar W33A. Tielens and Allamandola have observed[81-83] a band at 2043 cm^{-1} which is close to the C_3/argon matrix value of 2039 cm^{-1}. These workers had tentatively assigned this band to OCS and another at 2165 cm^{-1} to an 'XCN' species. This 2165 cm^{-1} band is very close to the C_5/argon matrix band at 2164 cm^{-1}. These (and possibly other) C_n species could be accreted from matter lost from carbon rich stars. It is speculated here that, especially on small grains where exothermic reactions can raise the grain temperature many degrees, photolysis of the $C_3 \bullet H_2O$ complex in icy layers of the grain mantle may lead to the eventual expulsion of propynal from the grain into the interstellar medium. The pronounced relative stability of propynal could make this a viable process on small grains where the grain diameter is ~10 μm or less. Long duration photolysis of the $C_3 \bullet H_2O$ complex in deeper-lying layers could result in further photorearrangement to the acetylene and CO products, with eventual release to the interstellar medium.

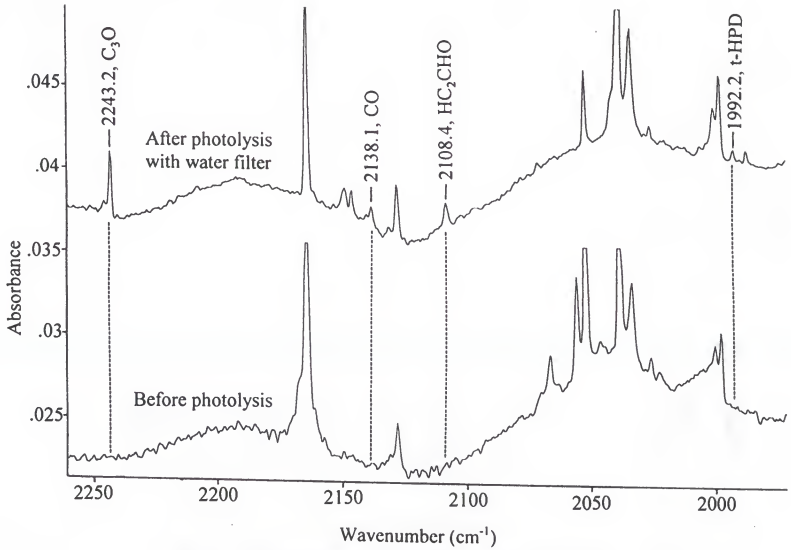

Figure 3-7. Portion of the 12K matrix infrared spectrum of $^{12}C_n$/Ar before and after photolysis ($\lambda > 390$ nm) with a water filter present.

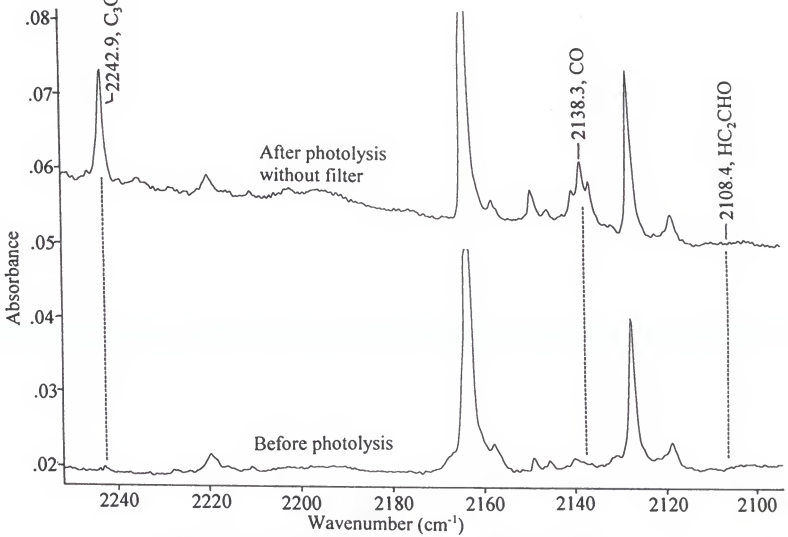

Figure 3-8. Portion of the 12K matrix infrared specrtum of $^{12}C_n$/Ar before and after photolysis ($\lambda > 390$ nm) without a water filter.

Summary

The potential surface for the rearrangement of nineteen C_3H_2O isomers has been calculated at the HF/6-31G*, QCISD(T)/6-31G*//HF/6-31G*, and MP2/6-31G* levels of theory. (The portion of Figure 1-4 that is represented by the potential surface in this chapter is shown in Figure 3-9). The relative stabilities and even the existence of certain minima and transition states is profoundly effected by the level of theory. The nonexistence of the isomers **H** and **N** at the MP2 level forces the production of cyclopropenone and propadienone to proceed through propynal, a condition not required at the HF level. The observed photochemical pathway from the $C_3{\bullet}H_2O$ complex to propynal through the hydroxypropadienylidene intermediates during photolysis with $\lambda \geq$ 400 nm is shown to be consistent with the MP2 surface. The mechanism of isomer interconversion is predicted to involve the migration of hydrogen atoms along a CCCO backbone via transition states in which one H is bonded to adjacent heavy atoms (C or O). If propynal is predicted to be photolytically depleted through **Q**, the isomers cyclopropenone and propadienone may be formed. However, the barriers leading out from these molecules are small and further decomposition to acetylene and CO is predicted. Experimental evidence is presented which supports the validity of this mechanism. It is proposed that the propynal observed in interstellar space is produced via the photolysis if $C_3{\bullet}H_2O$ complexes in the ice mantles of dust grains, and not in gas-phase ion-molecule reactions, as previously suggested.

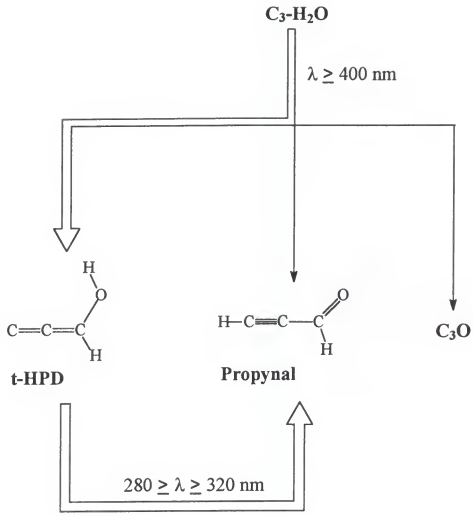

Figure 3-9. The experimental reaction scheme. The large arrow shows the reaction path described by the potential surface in Chapter 3.

Table 3-5. Rotational Constants (GHz) of minima found at the MP2/6-31G* level. Experimental values in parentheses.

Isomer	A	B	C
A	510.18	1.74	1.73
B	53.18	5.07	4.63
C	63.78	4.89	4.54
D	24.31	7.63	5.95
H	32.3	7.65	6.18
I	32.21	7.63	6.17
J	67.7	4.82	4.5
K	58.86	4.92	4.54
L	59.61	5.1	4.7
M	28.59	6.39	5.22
N	21.81	13.03	8.78
O	65.31 (68.04)[a]	4.77 (4.826)[a]	4.44 (4.500)[a]
Q	33.55	6.32	5.32
R	31.81 (32.05)[b]	7.72 (7.825)[b]	6.21 (6.281)[b]
S	123.79 (149.83)[c]	4.41 (4.387)[c]	4.26 (4.258)[c]

[a] From reference 87. [b] From reference 88. [c] From reference 89.

Table 3-6. Vibrational frequencies (cm^{-1}), intensities (km/mol), and symmetries of each C_3H_2O isomer found at the MP2/6-31G* level.

A	3901.1 (153)a′, 3765.5 (117)a′, 2185.5 (421)a′, 1751.6 (104)a′, 1224.8 (2)a′, 286.6 (174)a″, 257.7 (87)a′, 177.7 (0), 176.7 (18), 115.2 (3)a′, 43.9 (8), 37.8 (1)
B	3647.8 (94) a′, 3236.7 (7) a′, 2133.1 (635) a′, 1531.9 (184) a′, 1384.9 (56) a′, 1280.7 (191)a′, 1048.9 (84)a′, 1021.2 (18)a″, 749.5 (148)a″, 587.5 (36)a′, 195.8 (10), 145.0 (4)
C	3722.5 (171)a′, 3167.7 (18)a′, 2140.3 (679)a′, 1558.9 (59)a′, 1329.7 (336)a′, 1323.3 (130)a′, 1048.8 (1)a′, 978.1 (0)a″, 608.8 (108)a″, 592.7 (8)a′, 205.4 (5)a″, 172.7 (1)a′
D	3696.3 (154), 3291.0 (28), 1677.0 (128), 1372.6 (62), 1311.1 (232), 1044.1 (95), 945.0 (67), 828.2 (47), 676.8 (126), 395.4 (47), 258.7 (4), 167.0 (7)
H	3682.9 (85)a′, 3326.4 (2)a′, 1865.7 (151)a′, 1462.0 (65)a′, 1253.9 (159)a′, 1212.8 (31)a′, 981.8 (5)a′, 873.1 (35)a″, 825.4 (11)a′, 593.6 (142)a″, 481.2 (0)*a″, 423.9 (38)a′
I	3707.0 (79)a′, 3318.2 (2)a′, 1843.0 (186)a′, 1471.9 (44)a′, 1266.6 (13)a′, 1179.0 (185)a′, 970.2 (12)a′, 865.6 (12)a″, 823.6 (6)a′, 568.6 (136)a″, 483.2 (4)a″, 445.9 (0)*a′
J	3692.9 (150)a′, 3516.5 (52)a′, 2153.1 (53)a′, 1392.0 (31)a′, 1325.2 (321)a′, 932.7 (45)a′, 867.9 (80)a″, 640.1 (40)a″, 622.4 (2)a′, 560.8 (49)a′, 254.9 (5)a″, 219.6 (9)a′
K	3512.7 (60)a′, 3505.1 (8)a′, 2132.1 (46)a′, 1388.1 (7)a′, 1343.2 (292)a′, 910.2 (10)a′, 876.0 (150)a″, 638.4 (23)a″, 638.2 (27)a′, 565.6 (32)a′, 239.8 (15)a″, 193.3 (7)a′
L	3175.8 (40)a′, 3069.0 (57)a′, 1742.5 (152)a′, 1713.3 (172)a′, 1457.8 (4)a′, 1093.3 (56)a′, 1000.7 (1)a″, 901.9 (43)a′, 640.4 (45)a″, 511.5 (12)a′, 178.4 (27)a′, 145.8 (22)a″

Table 3-6. Continued.

M 3152.9 (26)a′, 3045.1 (97)a′, 1781.2 (85)a′, 1701.5 (245)a′, 1455.2 (18)a′, 1027.4 (54)a′, 1000.9 (3)a″, 944.5 (34)a′, 574.9 (30)a″, 559.6 (15)a′, 175.5 (7)a′, 117.7 (0)*a″

N 3354.3 (4), 3192.7 (12), 1468.6 (7), 1307.1 (23), 1281.8 (26), 1178.4 (39), 1017.4 (3), 987.4 (31), 835.0 (38), 761.7 (30), 609.0 (9), 439.6 (20)

O 3513.2 (50)a′, 3055.0 (77)a′, 2151.4 (63)a′, 1723.5 (98)a′, 1450.8 (10)a′, 1012.8 (0)*a″, 982.8 (100)a′, 634.9 (32)a′, 587.0 (18), 585.7 (43), 255.1 (3)a″, 200.1 (4)a′

Q 3273.6 (1)a′, 3072.2 (30)a′, 2174.0 (521)a′, 1404.3 (56)a′, 1294.4 (13)a′, 1070.7 (11)a′, 1041.7 (35)a′, 1005.8 (209)a″, 670.5 (15)a′, 484.1 (35)a′, 448.3 (21)a″, 242.2 (70)a′

R 3300.7 (1)a_1, 3269.9 (0)*b_2, 1980.5 (509)a_1, 1559.7 (4)a_1, 1188.7 (7)b_2, 1069.8 (6)a_1, 955.4 (0)a_2, 870.4 (0)a_1, 857.5 (47)b_2, 735.4 (62)b_1, 528.1 (0)*b_2, 457.9 (16)b_1

S 3251.2 (10)a′, 3163.0 (22)a′, 2206.8 (616)a′, 1734.5 (6)a′, 1529.6 (1)a′, 1108.6 (22)a′, 1021.8 (27)a″, 960.5 (1)a′, 710.5 (8)a″, 514.8 (10)a′, 278.7 (4)a″, 204.9 (17)a′

*Calculated intensity < 1, rounded to zero.

CHAPTER 4
A PHOTOCHEMICAL MECHANISM FOR C_3O FORMATION

Introduction

The $C_3 \bullet H_2O$ complex was originally identified in 1990 by Ortman *et al.*[37] Since that time this laboratory has been interested in the photochemical mechanisms and products which arise by photolyzing the $C_3 \bullet H_2O$ complex. The experiment itself is simple. Laser vaporized graphite and argon seeded with ca. 0.75% H_2O are codeposited in a matrix. Bands due to a complex between C_3 and H_2O are seen: 3598 cm^{-1} (OH sym. str.), 3712.2 cm^{-1} (OH asym. str.), 2052.3 cm^{-1} (asym. CCC str.), 1593.4 cm^{-1} (HOH bend), and 1214.3 cm^{-1} (sym. CC str.). An electronic band at 405.4 nm arising from the C_3 moiety is also seen.[75] The $C_3 \bullet H_2O$ complex is then subjected to a two step photolysis procedure. The first step photolyses the complex with radiation which spans the aforementioned 405.4 nm electronic band. After photolysis new bands due to C_3O, propynal (**E**), and 3-hydroxypropadienylidene (HPD) (**B** and **C**) appear while the $C_3 \bullet H_2O$ complex bands decrease. The second photolysis involves irradiating the matrix with light of wavelengths $280 \leq \lambda \leq 320$ nm. HPD bands are observed to decrease and bands due to propynal, CO, and acetylene to increase. (The experiment is summarized schematically in Figure 1-4, while the reaction route modeled in this chapter is shown in Figure 4-1).

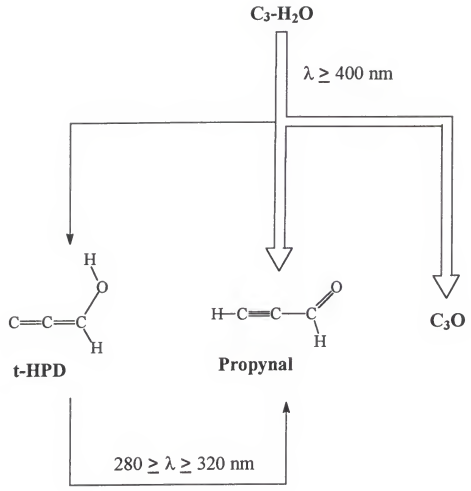

Figure 4-1. The experimental reaction scheme. The large arrow shows the reaction path represented by the potential surface in Chapter 4.

In Chapter 3 *ab initio* calculations were employed to characterize the mechanism leading from the $C_3 \bullet H_2O$ complex to HPD to propynal and finally to CO and acetylene.[90] The model involves initial insertion of the C_3 molecule into the OH bond of water. The remainder of the surface involves a series of hydrogen migrations followed by dissociation of two isomers into CO and acetylene. While this mechanism describes the experimental observations behavior quite well, several questions remain about the reaction scheme in Figure 4-1. First, even though it was shown how propynal could form from HPD during the second photolysis step, it was not at all clear how propynal was being formed in the first photolysis step with lower photon energies. Second, how was C_3O produced? Did it arise from the $C_3 \bullet H_2O$ complex? Third, why does C_3O form only during the first photolysis step and not during the second, higher energy step? Presented in this chapter is a calculated potential surface which explains the observed one step photolysis of $C_3 \bullet H_2O$ to propynal and C_3O.

Theoretical

All calculations were carried out at the MP2/6-31G* level using the GAUSSIAN 94 program package.[91] The inclusion of electron correlation has been shown to be extremely important in obtaining correct geometries[76] and can have a profound effect on the quantitative aspects and even the content of potential energy surfaces.[90] Unless otherwise stated, all minima and transition states were optimized in their ground electronic states constrained to the symmetries given in Tables 4-1 and 4-2. Optimized structures of all

minima and transition states are shown in Figures 4-2 and 4-3, respectively. The surface calculated in this study represents the minimum energies which must be supplied to promote reaction. Vibrational frequencies were calculated in order to determine the nature of the stationary point and to provide thermochemical data necessary for corrections to reaction energies. Finally, internal reaction coordinate (IRC) calculations were performed to confirm which minima connected to a particular transition state. The potential surface shown in Figure 4-4 represents points along the H_2C_3O potential surface. Those molecules that have one or no hydrogens have the MP2/6-31G* H or H_2 energy added in (at the infinite separation limit) so that the H_2C_3O total energy is maintained.

Results

Whatever surface is modeled it must ultimately lead to the creation of C_3O and propynal. We have shown previously that the precursor to propynal is the $C_3{\bullet}H_2O$ complex, whereas C_3O may have several unique routes of formation. These include:

$$C_3{\bullet}H_2O + h\nu \rightarrow C_3O + 2H \text{ or } H_2 \quad (1)$$

$$C_2 + CO + h\nu \rightarrow C_3O \quad (2)$$

$$C_2 + H_2O \rightarrow C_2{\bullet}H_2O \quad (3a)$$

$$C_2{\bullet}H_2O + h\nu \rightarrow C_2O + 2H \text{ or } H_2 \quad (3b)$$

$$C + CO + h\nu \rightarrow C_2O \quad (4a)$$

$$C + C_2O + h\nu \rightarrow C_3O \quad (4b)$$

Table 4-1. Total energies (hartrees), zero-point corrected relative energies (kcal/mol), spin squared eigenvalues, and zero-point energies (kcal/mol) of minima found at the MP2/6-31G* level of theory.

Molecule	Sym	MP2/6-31G*	Relative Energy	$\langle S^2 \rangle$	Z.P.E.
A	C_s	-189.895 21	0.0	0.0	19.9
B	C_s	-189.997 78	-60.3	0.0	24.2
C	C_s	-189.988 86	-54.8	0.0	24.1
D	C_s	-189.997 71	-61.3	0.0	23.1
E	C_s	-190.086 63	-117.1	0.0	23.1
F	C_s	-189.374 38	13.3[a]	1.167	18.9
G	C_s	-189.343 49	30.9[a]	0.922	17.1
C (^{3}P)		-37.733 83		2.005	---
C_2 ($^1\Sigma_g^+$)	$D_{\infty h}$	-75.696 17		0.0	2.7
C_2 ($^3\Pi$)	$D_{\infty h}$	-75.688 20		2.005	2.7
CO ($^1\Sigma^+$)	$C_{\infty v}$	-113.021 21		0.0	3.0
C_2O ($^3\Sigma^-$)	$C_{\infty v}$	-150.834 92		2.059	5.6
C_3O ($^1\Sigma^+$)	$C_{\infty v}$	-188.860 03		0.0	9.7
C_3O ($^3\Sigma^-$)	$C_{\infty v}$	-188.740 66		2.521	10.2
C_4O_2 ($^3\Sigma_g^-$)	$D_{\infty h}$	-301.896 13		2.151	15.8
H		-0.498 23		0.750	---
H_2	$D_{\infty h}$	-1.144 14		0.0	6.5

[a] Relative energy composed of stationary point and hydrogen atom total energies with zero point correction.

Table 4-2. Total energies (hartrees), zero-point corrected relative energies (kcal/mol), spin squared eigenvalues, and zero-point energies (kcal/mol) of transition states found at the MP2/6-31G* level of theory.

Transition State	Sym	MP2/6-31G*	Relative Energy	$\langle S^2 \rangle$	Z.P.E.
TS1	C_1	-189.848 43	27.9	0.0	18.4
TS2	C_1	-189.808 72	51.5	0.0	16.9
TS3	C_s	-189.327 87	35.0[a]	0.897	11.1
TS4	C_s	-189.304 59	49.5[a]	1.005	11.1
TS5	C_s	-189.796 85	58.2	0.0	16.2
TS6	C_s	-189.807 89	51.1	0.0	16.0
TS7	C_s	-189.834 44	36.1	0.0	17.8
TS8	C_s	-189.856 73	21.5	0.0	17.2
TS9	C_1	-189.969 86	-44.1	0.0	22.6
TS10	C_s	-188.709 73	---	2.040	10.3

[a] Relative energy composed of stationary point and hydrogen atom total energies with zero point correction.

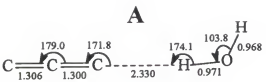

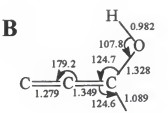

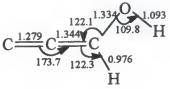

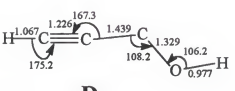

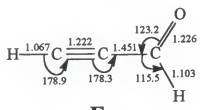

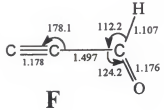

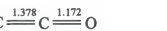

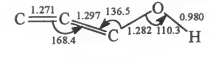

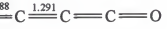

Figure 4-2. Optimized structures of all minima found at the MP2/6-31G* level of theory.

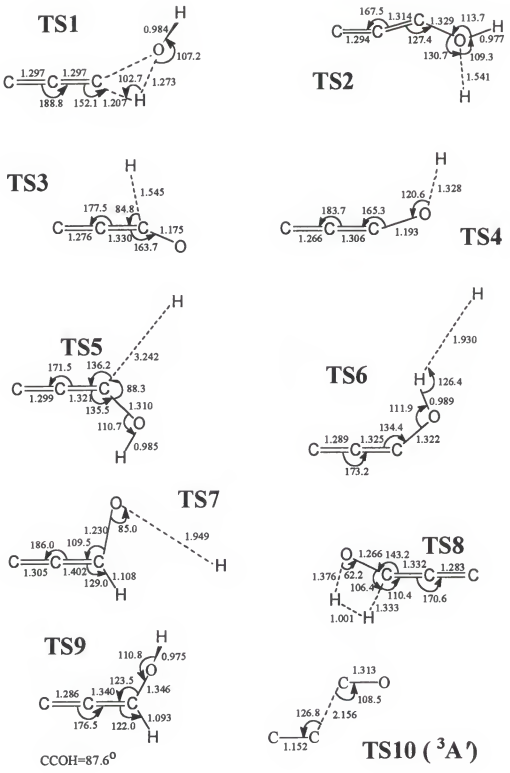

Figure 4-3. Optimized structures of all transition states found at the MP2/6-31G* level of theory.

$$2C_2O + h\nu \rightarrow C_4O_2 \quad (5a)$$

$$C_4O_2 + h\nu \rightarrow C_3O + CO \quad (5b)$$

Although some of the above reactions may not require photolytic activation, their inclusion is necessary since it is known that C_3O is not present in the matrix before photolysis. The reactants, carbon atom, C_2, C_3, and water, are known to be the most abundant species after deposition, and thus must be considered as possible precursors to C_3O. In the following section (A), attention is focused on the formation of C_3O and propynal via the H_2C_3O potential surface. Then, in the next section (B), the bimolecular reactions specified in equations 2-5, which may lead to C_3O formation are considered.

The C_3H_2O Potential Surface

In the previous chapter it was shown how a two step photolysis involving a series of hydrogen migrations could produce propynal from the $C_3{\bullet}H_2O$ complex. However, a competing mechanism exists which makes propynal during the first photolysis step (with $\lambda \geq 400$ nm). This process almost certainly begins with the $C_3{\bullet}H_2O$ complex since no propynal-or any other product-is observed in the matrix prior to excitation of the 405 nm C_3 electronic transition. Yet this simple observation leads us to the presumption that a different mechanism produces propynal and C_3O. This new mechanism, unlike that in the previous chapter, largely involves photolytic detachment of hydrogen which later recombines at various points on the potential surface. Such a mechanism assumes that

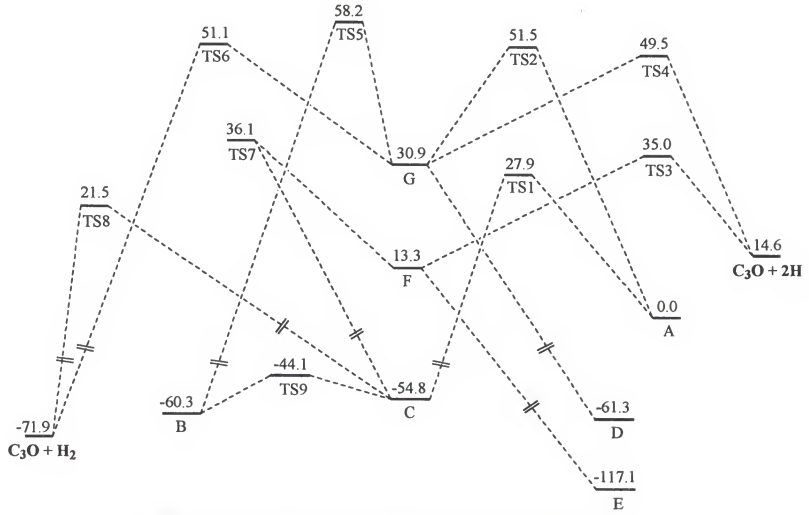

Figure 4-4. Potential surface at the MP2/6-31G* level. Numbers are zero-point corrected energies (kcal/mol) relative to the $C_3 \cdot H_2O$ complex.

hydrogen atoms can diffuse through a matrix. There is evidence that this occurs. Experiments have shown that H atoms can migrate through H_2O,[92-94] CO,[95] and N_2[94] matrices. After encountering other open shell species, H atoms can combine to form basic organic molecules like NH_3,[94] HCO, formaldehyde, and methanol.[95] A mechanism which incorporates this behavior is necessary here since the suspected precursor to C_3O, the $C_3 \bullet H_2O$ complex, contains hydrogen.

Photons having energy up to 71.5 kcal/mol (400 nm) are available during photolysis. This value places an upper limit on the step size (i.e the energy difference) between points on the surface. The $C_3 \bullet H_2O$ complex (**A**) has two outlet paths through transition states 1 and 2 (TS1 and 2), and each of these will be examined separately.

The HPD isomers **B** and **C** form via the transition state TS1. Only a small barrier (TS9) exists between the HPD isomers, yet **C** is only seen during photolysis. The barrier for HPD conversion to propynal (**E**) in the hydrogen migration scheme is 87.0 kcal/mol,[90] making that particular path unavailable here. The only other way propynal can be formed from HPD is through hydrogen atom dissociation and recombination. The most direct way this can be accomplished is through hydrogen loss from the oxygen, resulting in molecule **F**, followed by recombination at the terminal carbon. This is calculated to be a very exothermic reaction (130.4 kcal/mol). The step from **C** to **F** is predicted to require 68.1 kcal/mol, and if there is a transition state more than 3 kcal/mol above **F**, this path will not be energetically accessible. Figure 4-4 shows that the transition state (TS7) from **C** to **F** lies almost 91 kcal/mol above **C**. However, this transition state does not represent the actual transition state. The real transition state is formed by the crossing of the singlet and

triplet dissociation/recombination surfaces (shown in Figure 4-5). In this calculation the O-H bond distance was increased stepwise by 0.2Å, starting near the optimized cis-HPD O-H bond distance. At each point the remainder of the complex was allowed to relax, constrained only to C_s symmetry. As Figure 4-5 shows, there are two intersections between the singlet and triplet surfaces, but the limiting barrier here is at an O-H distance of ca. 1.82Å. The barrier of approximately 85 kcal/mol created by this intersection is only marginally smaller than the singlet surface barrier at TS7. In any case, both barriers require more energy than is input in the experiments, leading to the conclusion that the transformation of **B** or **C** to **F** does not occur during photolysis.

The ground state structure of **F** indicates that the unpaired electron resides primarily on the terminal carbon (Figure 4-2). Because of this, reaction between a H atom and **F** will more than likely lead to propynal formation in an extremely exothermic reaction (130.4 kcal/mol). Once **F** is formed, reaction with H atom at the terminal carbon will yield propynal. As shown in Figure 4-6, the reaction from **F** to **E** has a small barrier which is formed by the crossing of the singlet and triplet reaction surfaces. Dissociation along the triplet surface approaches the total energy of molecule **F** and the H atom at infinite separation, 130.4 kcal/mol above propynal and ca. 12 kcal/mol below the singlet-triplet intersection. A similar type of path is found for H loss from linear HC_3H.[96] While this barrier is a fraction of the reaction enthalpies or photolysis energies considered in this surface, it is more than adequate to keep propynal from being formed in the gas phase. In the absence of a photon or energetic reactants, such small barriers as this could actually prevent hydrogenation of gas-phase unsaturated species.

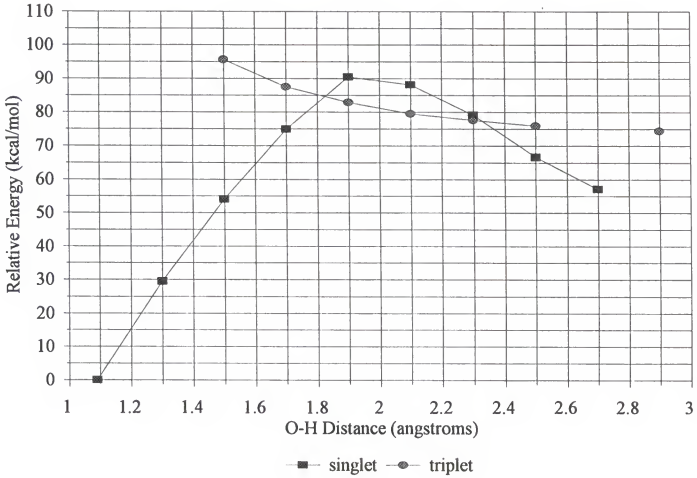

Figure 4-5. Graph representing the singlet (squares) and triplet (circles) surfaces for H atom dissociation from cis-HPD (**C**). Note that the triplet surface approaches the molecule **F** + H atom total energies at infinite separation (68.1 kcal/mol). Energies are relative to the fully optimized cis-HPD molecule.

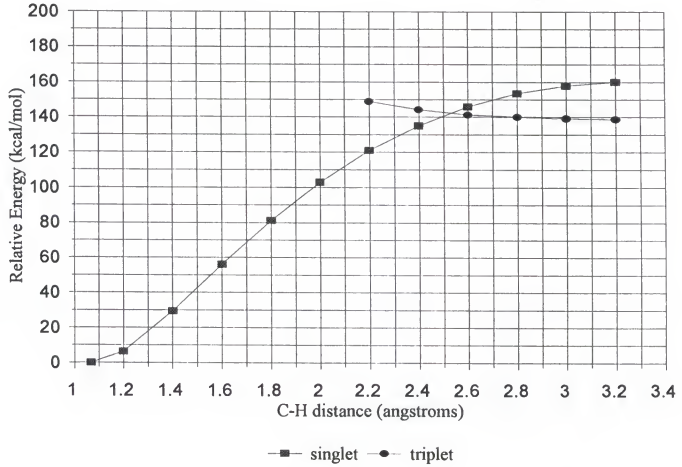

Figure 4-6. Graph representing the singlet (squares) and triplet (circles) surfaces for H atom dissociation from propynal (**E**). Note that the triplet surface approaches the molecule **F** + H atom total energies at infinite separation (130.4 kcal/mol). Energies are relative to the fully optimized propynal molecule.

C_3O may form from HPD as well. There are only two possible reaction pathways. The first is the path **C** → TS8 → $C_3O + H_2$. The step from **C** to TS8 is calculated to require 76.3 kcal/mol. This is 5.2 kcal/mol more than the upper energy limit, and, even considering the calculation error intrinsic to the level of theory, this route is probably not possible. The other path once again involves hydrogen loss from **B** or **C** → **F** → TS3 → $C_3O + 2H$. Once **F** is made there is just a 21.7 kcal/mol barrier to H loss and C_3O formation. However, as was mentioned above, the path from **B** or **C** to **F** probably does not exist. Our results here indicate that once HPD is made it cannot be photolyzed with photons of $\lambda > 400$ nm to produce C_3O or propynal.

The outlet from the $C_3 \bullet H_2O$ complex through TS2 involves a single step rotation of the H_2O with H loss. (It should be kept in mind that the process initially begins with excitation of C_3 and that the barrier TS2 is a minimum energy). The product, **G**, is the hub of several paths leading to formation of **B**, **C**, **D**, $C_3O + H_2$, and $C_3O + 2H$. The formation processes leading to **B**, **C**, and **D** by H atom capture are calculated to be very exothermic. The process **G** → **B** is calculated to have a barrier of 27.3 kcal/mol. While this is well within the photon energy limit, the actual barrier is approximately 15 kcal/mol smaller due to a singlet/triplet surface crossing (Figure 4-7). C_3O is formed by both hydrogen abstraction in TS6 and dissociation in TS4. All paths leading out of **G** lie well within the experimental energy limit and should be rapid reactions under the experimental photolysis conditions.

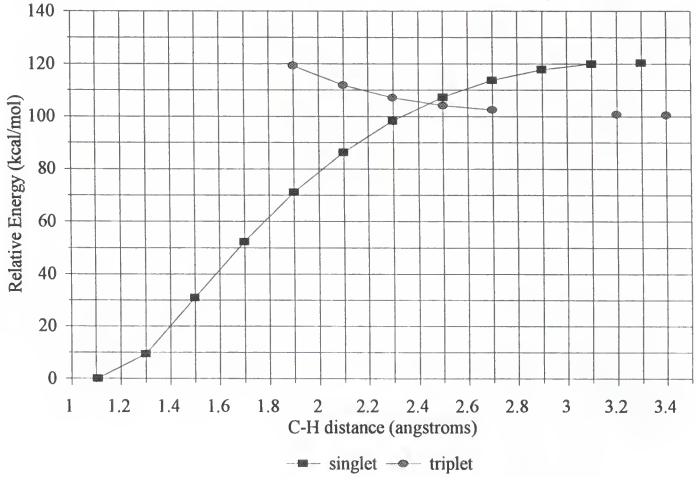

Figure 4-7. Graph representing the singlet (squares) and triplet (circles) surfaces for H atom dissociation from trans-HPD (**B**). Note that the triplet surface approaches the molecule **G** + H atom total energies at infinite separation (98.0 kcal/mol). Energies are relative to the fully optimized trans-HPD molecule.

Bimolecular Reactions Forming C_3O

After deposition many carbon species are present in the matrix. Carbon atom and C_2 exist in relatively high abundance, and, to a lesser extent, C_3 and the $C_3 \bullet H_2O$ complex. In the previous section it was shown how the $C_3 \bullet H_2O$ complex could, by sequential loss of hydrogen atoms, form C_3O. Yet the large abundance of C atom and C_2 means that the probability of reactions 2-5 occurring in the matrix may be high if they are energetically possible. In this section we examine whether reactions 2-5 are possible.

We have attempted to model the ground and excited state potential surface of reaction 2. Both C_2 and CO have singlet ground states, however, despite the fact that this reaction is predicted to be exothermic by 85.5 kcal/mol (zero-point corrected), an extensive search of the singlet surface found no transition state that would yield C_3O. The only transition state located was a T-shaped structure for the migration of CO around C_2 (i.e. $OCC_1C_2 \leftarrow TS \rightarrow C_1C_2CO$). However, a transition state (TS10) connecting ($^3\Pi$) C_2 and ($^1\Sigma^+$) CO to C_3O was found on the triplet surface. The $^3\Pi$ state of C_2 was used since the singlet-triplet separation in C_2 is known to be just 716 cm^{-1} (2.0 kcal/mol; our calculations find a separation of 5.0 kcal/mol), with many other allowed triplet transitions falling within the photolysis range of these experiments, including the well-known Swan system at ~ 19,400 cm^{-1}.[25] At the MP2 level TS10 is predicted to lie just 0.2 kcal/mol above the ($^3\Pi$) C_2 and ($^1\Sigma^+$) CO reactants, but 19.0 kcal/mol above C_3O. Recently, Woon and Herbst[97] found this transition state at the MCSCF/cc-pVTZ level to be 32.9 kcal/mol above C_3O and 12.7 kcal/mol above C_2 and CO. The height of this barrier is

obviously very dependent on the multiconfigurational nature of this calculation. This is almost certainly due to the well-known nondynamical correlation effects in C_2, resolved only with very comprehensive calculations.[98]

Another important process involving C_2O is reaction 3. This is a two step sequence where the $C_2 \bullet H_2O$ complex is first formed (3a) and then followed by photolysis to C_2O and 2H or H_2 (3b). The latter reaction assumes that a process similar to the C_3O formation mechanism, shown in the previous section, exists for the production of C_2O. The presence of C_2O may have important consequences which are elaborated below. Like the $C_3 \bullet H_2O$ complex, the $C_2 \bullet H_2O$ complex is expected to be weakly bound, more than likely forming only in the condensed phase. However, theory does not predict the existence of a $C_2 \bullet H_2O$ complex. This is contrary to the calculation results on the $C_n \bullet H_2O$ series in which stable complexes were found for n = 3-9.

The presence of CO in the matrix is extremely important because reactions 4 and 5 provide simple exothermic paths to C_3O formation. DeKock and Weltner[99] have shown experimentally that the sequential reaction of carbon atoms with CO and C_2O can make C_3O in an Ar matrix at 4K. Our results indicate that the reactions of ^3P carbon atom with CO and C_2O will be exothermic by 63.7 kcal/mol and 178.7 kcal/mol, respectively. Results from density functional calculations show that, with the exception of CO, the reaction of (^3P) C atoms with C_nO species are all exothermic by at least 130 kcal/mol.

Reaction 5 is a two step process in which two C_2O molecules combine to form butatrienedione (C_4O_2), followed by photolysis of C_4O_2 to C_3O and CO. The former reaction is calculated to be 137.4 kcal/mol exothermic, while the latter is predicted to be

endothermic by ca. 12 kcal/mol. The endothermicity of 5b is not a problem since it is known that C_4O_2 photodissociates into C_3O and CO with $\lambda > 400$ nm.[100] Results of a 2-configuration-MCSCF calculation[100] indicate that an avoided crossing occurs when the $^1B_u \leftarrow {}^1A_g$ electronic transition of C_4O_2 at 412 nm is correlated with the C_3O and CO products. The barrier created by this crossing has a maximum energy less than 70 kcal/mol, and will be an available path in the experiments conducted here.

While the addition of carbon atoms and molecules to oxygen containing species have been considered, the reverse-addition of oxygen atoms to carbon species-is certainly possible. In the matrix water molecules serve as a source of oxygen atoms. Woon and Herbst[97] have recently shown that the process of making C_3O by adding an oxygen atom to C_3 proceeds over a very small barrier (1.8 kcal/mol) but is rather exothermic (99.6 kcal/mol) overall. While this small barrier is sufficient to prevent reaction in the gas phase, a photochemically driven process in the condensed phase may be possible. While these types of reactions were not investigated theoretically here, they may be an important pathway to formation of C_nO molecules.

Summary

In this and the previous chapter attention has been focused on the mechanisms of complex organic molecule formation from the $C_3 \cdot H_2O$ complex in the condensed phase. We have pointed out that such reactions could occur in the mantles of interstellar dust grains. Such a hypothesis is not new. In 1968 Williams[101] suggested that H atom

diffusion through grain mantles could react with trapped molecules and atoms to form hydrogenated products. Later, the diffusion of H atoms was proposed for the formation of NH_3, H_2O, H_2CO, CH_3OH, and others.[84,102] Owing to the low temperature of dark clouds, most species in interstellar space would be expected to condense onto cold grain surfaces. And, rather than being trapped in inert gas matrices, these molecules would be part of a 'soup' of reactive molecules containing H, C, N, and O. Grain mantles such as these, exposed to unfiltered radiation, could be an important factory for making more complex molecules. Certainly, the experiments on the $C_3 \bullet H_2O$ complex[37,75] and NH_3[94] are examples of this.

The following conclusions on the photolysis of the $C_3 \bullet H_2O$ complex with $\lambda \geq 400$ nm have been reached. (1) The $C_3 \bullet H_2O$ complex is the precursor to C_3O and propynal. (2) Photolysis of the complex through TS1 will lead to the HPD isomers, **B** and **C**. C_3O and propynal can be formed from the HPD isomers via molecule **F**. However, the barrier heights leading out of the HPD isomers prevent the formation of either C_3O or propynal. (3) Photolysis of the $C_3 \bullet H_2O$ complex through TS2 will yield molecule **G**. This molecule produces molecules **B** or **D** through H atom capture, or C_3O and H atom via hydrogen atom dissociation in TS4 or abstraction in TS6. (4) The formation of propynal and C_3O during $\lambda \geq 400$ nm photolysis in this scheme is entirely different from the mechanism in which HPD is an intermediate. Contrary to the previously proposed mechanism[90] involving H atom migration, this mechanism relies on H atom dissociation and recombination reactions. (5) It is postulated that reactions of C and O atoms with C_n and C_nO species may be instrumental in forming C_3O.

CHAPTER 5
EXPERIMENTAL OBSERVATION OF LONG CHAIN CARBON ANIONS

Introduction

Carbon atoms have recently been shown to exhibit an unusual ability to cluster into fascinating shapes and sizes. Forms such as chains, rings, balls, tubes, and ropes have been reported.[25,103-106] For small C_n carbon clusters, gas phase and matrix isolation infrared spectroscopic studies have established linear or near-linear structures for the smallest clusters with $n \leq 9$ and 13.[25,107-109] The interest in carbon clusters lies not only in their appealing shapes and myriad sizes, but in their possible involvement in the astrochemistry of the interstellar medium.

Recently, Maier and coworkers proposed[110] that highly unsaturated hydrocarbon chain radicals are the carriers of some of the DIBs. They mass selected and matrix isolated specific C_n clusters, then recorded their electronic absorption spectra. A series of neutral and anionic linear carbon clusters containing even numbers of carbons atoms, C_{2n} (n = 3-7) and C_{2n}^- (n = 2-10), were investigated, and a number of coincidences with the observed diffuse interstellar band wavelengths were noted. Although clusters containing more than 20 carbons were not observed in these experiments, there is general interest in

their spectroscopic properties. Watson speculated[111] that even longer chains might be responsible for the DIBs. Others have proposed[112] that the long carbon chains (n >10) are crucial for the formation of the stable fullerenes, with carbon growth occurring sequentially by formation of linear chains together with larger planar rings which could then coalesce to form the fullerenes. Thus, spectroscopic information on the longer chains would be helpful in advancing these ideas.

Here the generation of anionic cluster chains containing up to 36 carbons and the spectroscopic study of these chains in the visible and infrared regions is reported. It will be shown that a few of the carbon cluster absorption bands coincide closely to UIR bands observed from interstellar space.

Experimental

The experimental set up used is sketched in Figure 1-1. The negative carbon cluster ions were generated by the two methods described in chapter 1. When the electron gun is employed, anions are partially extracted from the vaporization region by the electric field created between the O-ring electrode and cathode of the electron gun and then trapped in an Ar matrix at 12-20K. The O-ring electrode indicates the electron beam current inside the deposition chamber. With a +60V potential the typical current collected by this electrode was 50 μA with Ar gas flowing, but during vaporization of graphite this current drops to 20-30 μA. This indicates a possible electron capture process by high electron affinity neutral carbon clusters.

To obtain the higher member clusters, annealing is required. During deposition the matrix temperature was 20K. After deposition, annealing up to 36K was carried out. Under these conditions very strong diffusion of the trapped carbon species is expected to occur. For neutral C_n chains with $n \leq 9$, diffusion-controlled aggregation has been observed in rare gas matrices by tracking the vibrational bands of certain clusters as a function of temperature in the 12-36K range.[43] Reaction between neutral carbon clusters apparently occurs with little or no activation energy and is strongly exothermic.[44] Calculations indicate that reactions between carbon chain neutrals and anions are also very exothermic,[113] and could occur as readily as those between neutrals.

To differentiate bands due to neutral clusters from those due to anionic clusters, use was made of CCl_4 (0.1% mixed with the Ar isolant gas). CCl_4 and its electron impact and photoproducts, such as CCl_3, CCl_2, and Cl, compete with the C_n species as electron traps. C_n clusters are known[20,21] to possess high electron affinities and increase with increasing cluster size. In matrices containing C_n / C_n^- / Ar (+ 0.1% CCl_4) the ratios of the anion C_n^- to neutral C_n absorption bands were several times smaller than the ratios in matrices containing no CCl_4. Also, experiments were run where the matrix was photolyzed with an unfiltered mercury arc lamp. The photons from this lamp photodetach an electron from the carbon cluster anions, decreasing their absorption signal. Cluster neutrals were unaffected by photolysis.

Results

Electronic

The spectra obtained after preparation of the cluster-containing matrices are shown in Figures 5-1 to 5-5. The cluster species responsible for the various bands are marked in the figures. Band wavelengths, intensity information, and probable electronic states involved in the transitions are given in Table 5-1.

The highest energy electronic bands for anionic clusters were observed for C_6^-, whose band origin lies at 615.8 nm (Ar matrix). A progression in the CC stretch vibration built on this origin was also observed. These bands correspond well with the Ne matrix bands observed by Maier and coworkers after mass selection.[110] Table 5-1 compares the results from the two matrices. Except for the expected matrix shift and the absence of the weaker bands in the Ar matrix runs, the comparison with the Ne matrix results is very good. Calculations carried out by Schmatz and Botschwina[114] on the four lowest doublet states of C_6^- support the assignment of the 607.6 nm (Ne) / 615.8 nm (Ar) origins to the $C^2\Pi_g \leftarrow X^2\Pi_u$ electronic transition of C_6^-. It has been noted[110,114] that the C_6^- origin band lies close to a prominent diffuse interstellar band at 608.97 nm. But we have observed that C_6^- is unstable to UV photolysis (Figure 5-1), and therefore it is probably unsuitable as a DIB carrier. Although no negative molecular ion has been observed in the interstellar medium (ISM), the large electron affinity of the even carbon clusters ensures that they will be very stable species and may be capable of surviving in the harsh environment of the

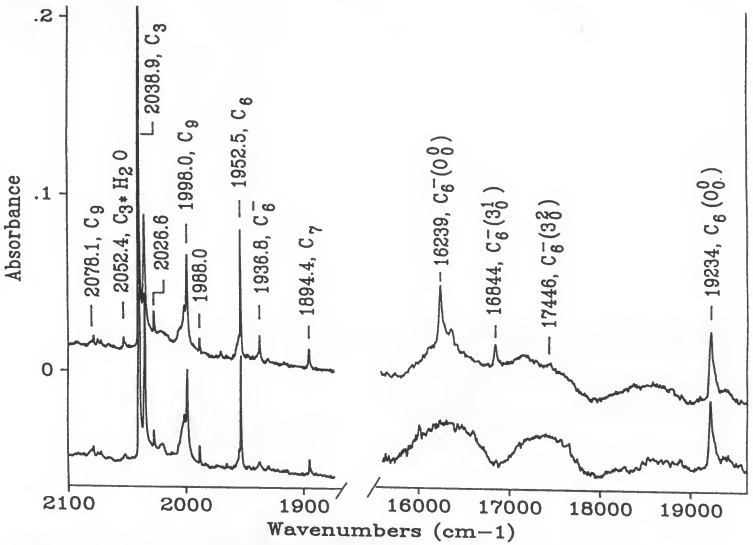

Figure 5-1. Part of the vibrational (left) and electronic (right) spectra for the C_n/C_n^- clusters in an Ar matrix at 12K, recorded before (upper) and after photolysis (lower). Photolysis was for 0.5 hr using a 265nm cut-off filter.

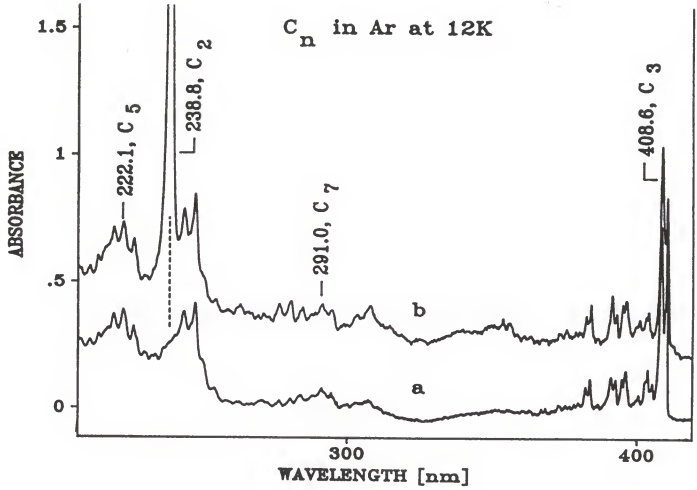

Figure 5-2. Part of the electronic spectra of C_n species vaporized with two different laser beam densities at the vaporization point. In (a) a low flux of photons is used and no plasma is observed. In (b) a high flux of photons is used and a purple plasma is seen at the graphite surface. Note the difference in C_2 at 238.8 nm.

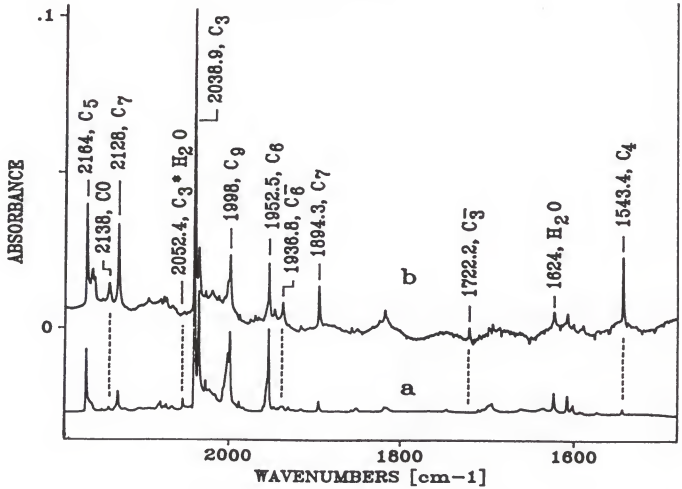

Figure 5-3. Part of the vibrational spectra of C_n species vaporized with two different laser beam densities at the vaporization point. In (a) a low flux of photons is used and no plasma is observed. In (b) a high flux of photons is used and a purple plasma is seen at the graphite surface.

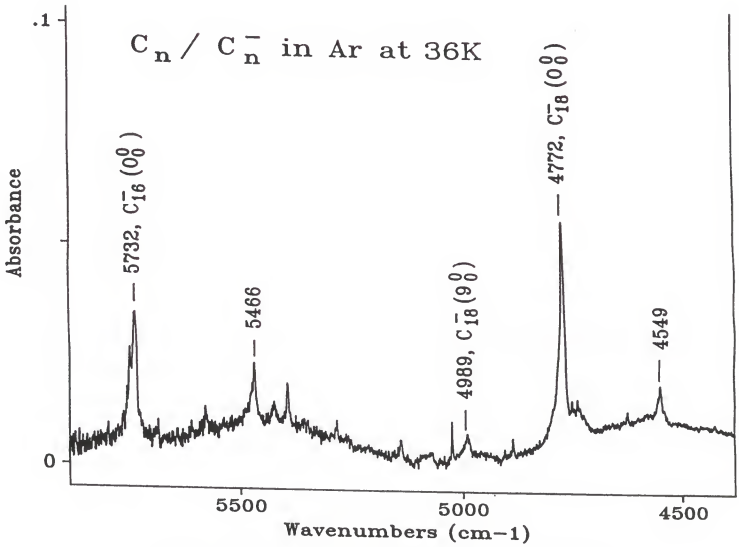

Figure 5-4. Spectrum showing absorption bands due to the electronic transitions of the C_{16}^- and C_{18}^- clusters isolated in an Ar matrix.

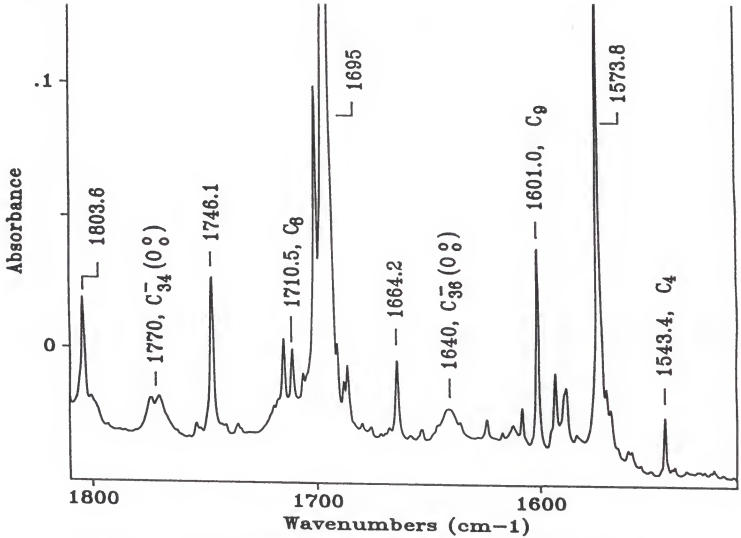

Figure 5-5. Spectrum showing absorption bands due to electronic transitions of the C_{34}^- and C_{36}^- clusters isolated in an Ar matrix. Other known bands are marked accordingly.

Table 5-1. Experimental electronic absorption band positions (λ in nm, ν in cm^{-1}) and absorbances for anionic carbon clusters isolated in neon and argon matricies. Band widths (FWHM, in cm^{-1}) in parenthesis. All 0-0 transition energies are plotted in Figure 5-6.

Ne Matrix, 5K[a]			Ar Matrix, 36K[b]				Assignment[a,b]
λ	ν	$\Delta\nu$	λ	ν	$\Delta\nu$	A_{max} (FWHM)	
607.6	16458	0	615.8	16239	0	0.003 (35)	C_6^- ($^2\Pi_g \leftarrow X^2\Pi_u$) (0_0^0)
586.1	17065	607	593.7	16844	605		(3_0^1)
577.9	17304	846					
565.7	17677	1219	573.2	17446	1207		(3_0^2)
547.2	18275	1817					(2_0^1)
539.9	18522	2064					(1_0^1)
967.3	10338	0	981.4	10189	0	0.013 (37)	C_{10}^- ($^2\Pi_g \leftarrow X^2\Pi_u$) (0_0^0)
933.7	10710	372					(5_0^1)
923.7	10826	488					(4_0^1)
811.0	12330	1992					(3_0^1)
804.5	12430	2092					(2_0^1)
1249.1	8006	0	1264.9	7906	0	0.022 (30)	C_{12}^- ($^2\Pi_u \leftarrow X^2\Pi_g$) (0_0^0)
1200.6	8329	323					(6_0^1)
1460.0	6849	0	1474.4	6782	0	0.058 (20)	C_{14}^- ($^2\Pi_g \leftarrow X^2\Pi_u$) (0_0^0)
1402.0	7133	283					(7_0^1)
1729.0	5784	0	1744.6	5732	0	0.030 (14)	C_{16}^- ($^2\Pi_u \leftarrow X^2\Pi_g$) (0_0^0)
1658.7	6029	245	1668.1	5995	263		(8_0^1)
2069.1	4833	0	2095.5	4772	0	0.050 (13)	C_{18}^- ($^2\Pi_g \leftarrow X^2\Pi_u$) (0_0^0)
1980.6	5049	216	2004.4	4989	217		(9_0^1)
2439.9	4099	0	2502.5	3996	0	0.007 (19)	C_{20}^- ($^2\Pi_u \leftarrow X^2\Pi_g$) (0_0^0)
2324.5	4302	203					

Table 5-1. Continued.

			2891.0	3459	0	0.019 (17)	$C_{22}^{-}(^2\Pi_g \leftarrow X^2\Pi_u)(0_0^0)$
			3278.7	3050	0	0.002 (13)	$C_{24}^{-}(^2\Pi_u \leftarrow X^2\Pi_g)(0_0^0)$
			3643.0	2745	0	0.009 (17)	$C_{26}^{-}(^2\Pi_g \leftarrow X^2\Pi_u)(0_0^0)$
			4145.5	2407	0	0.003 (15)	$C_{28}^{-}(^2\Pi_u \leftarrow X^2\Pi_g)(0_0^0)$
			4557.9	2194	0	0.010 (13)	$C_{30}^{-}(^2\Pi_g \leftarrow X^2\Pi_u)(0_0^0)$
			5081.3	1968	0	0.023 (7)	$C_{32}^{-}(^2\Pi_u \leftarrow X^2\Pi_g)(0_0^0)$
			5649.7	1770	0	0.016 (11)	$C_{34}^{-}(^2\Pi_g \leftarrow X^2\Pi_u)(0_0^0)$

[a] Reference 110

[b] This work.

[c] ± 5 cm^{-1}, ± 10 cm^{-1}, and ± 2 cm^{-1} uncertainty in the 20,000 - 15,000 cm^{-1}, 15,000 - 7000 cm^{-1}, and 7000 - 1600 cm^{-1} regions, respectively.

ISM,[114] provided they are large enough to dissipate any absorbed energy through radiationless transitions. In the present experiments, no decrease in intensity during UV photolysis ($\lambda > 200$ nm, 0.5 hr matrix photolysis) was observed for any of the C_n^- bands with $n \geq 16$, which is consistent with what Maier and coworkers report.[110]

As Table 5-1 shows, the correspondences of band positions in Ne and Ar matrices for all even clusters up to and including C_{20}^- is good, with a typical Ar-Ne matrix energy shift for electronic transitions. Figure 5-6 shows a plot of the wavelengths of the band origins of various anions versus the number of carbons in the chain. The data comes from mass selected C_{2n}^- (with $n \leq 8$) molecules, from C_{2n}^- (where n = 9 and 10) molecules generated by laser ablation of graphite with Ne (I) radiation in a Ne matrix,[110] and the Ar matrix data presented here. A smooth curve extending up to C_{36}^- (Ar matrix) is found. Note that the wavelengths for the larger chain species occur in the infrared region, where, for example, the electronic transition band origin of C_{36}^- lies at 1640 cm^{-1} (6097.5 nm). A rough empirical relation has been found to describe this curve: $\lambda(nm) = 13.1\ n^{1.7} + 337$, where n is the number of carbons in the chain.

These results generate a few questions. (1) Why is the formation of even numbered clusters apparently preferred? (2) Why is it suggested that the curve in Figure 5-6 represents predominantly linear clusters rather than some other structure for the larger clusters? And finally, (3) are there astrophysical implications?

The appearance of only even-membered carbon clusters can be understood from previous experimental results and simple molecular orbital theory. In his study on the sublimation of graphite, Honig found[115] substantial quantities of C_n anions with the even

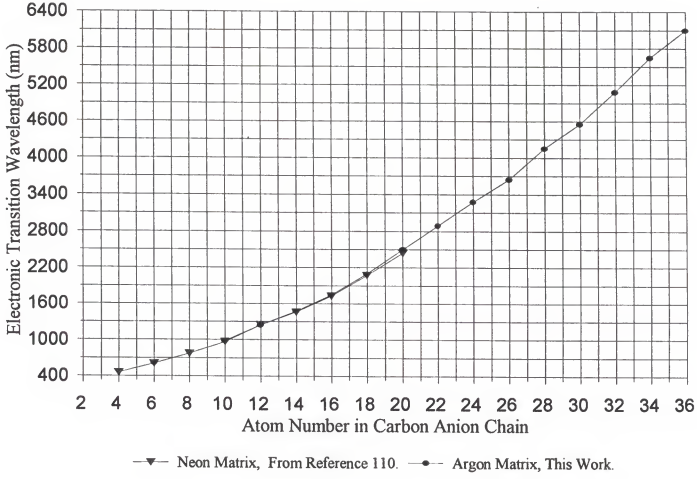

Figure 5-6. Graph of 0-0 electronic transition wavelength as a function of the number of carbon atoms in the anionic cluster.

species far more abundant than the odd . Later, Pargellis[116] sputtered negative carbon clusters from graphite and found an even-odd alternation with the even species in greater abundance. Pitzer and Clementi[44] pointed out that this follows from simple molecular orbital theory. The HOMOs (highest occupied molecular orbitals) in even neutral C_n clusters are half-filled bonding π orbitals which can accommodate another electron, whereas in the odd species the electron must go into an empty nonbonding orbital. This is reflected in the considerably higher (~1eV) vertical electron affinities of the neutral even chains compared to the odd chains.[20,21] The net result is that stabilization of the negative even-membered clusters is greater compared to the odd-membered clusters.

Are these results consistent with the appearance of ring structures or with linear chains? It is known that the smaller neutral and anionic carbon clusters ($n \leq 9$) form linear chains,[20,21,25,117-120] while the larger chains are expected to adopt the more stable ring conformations.[25,117-121] For anionic clusters with $10 \leq n \leq 20$, Helden, Kemper, Gotts, and Bowers have observed both monocyclic and linear isomers.[122] There are two reasons which suggest that the larger clusters observed here are chain species. First, is their method of formation. Annealing of the matrix to allow the diffusion and reaction of smaller clusters, argues for the formation of chain-like species. Energetically and statistically, it is not expected that a chain, once formed, would close upon itself and form a ring in the matrix. Second, based on DFT calculations (Chapter 6), anionic ring structures are predicted to be much less stable than the corresponding chain-like structures.[113] It is tentatively concluded that the bands observed here occur from chain-like carbon species.

A search was made for coincidences between the observed carbon cluster anion bands and the unidentified interstellar emission bands. Prominent UIR bands have been observed at 3.3, 6.2, 7.7, 8.6 and 11.3 μm (3030, 1610, 1300, 1160 and 885 cm^{-1}). As can be seen from Figure 5-7 there are a few coincidences between the UIR band positions and the 0-0 electronic transition energies of C_n^- ($18 < n < 36$), especially at 3.3 and 6.2 μm. The critical question is how close the matrix and gas phase values match. The Ar matrix-gas phase red energy shift for electronic 0-0 transitions in C_n^- is unknown for these size clusters, but generally this value is expected to be smaller for larger clusters based on the decreasing Ne-Ar matrix energy shift. Neon matrix values are closest to the gas-phase values. For C_6^- the Ne-Ar energy shift is 219 cm^{-1} and it is reduced to 52 cm^{-1} for C_{16}^-. For C_6^-, gas phase-Ne matrix the 0-0 electronic transition energy shift is known to be 20 cm^{-1} and is expected be smaller for a longer cluster.[117-120] Taking into account the above trends for the 0-0 electronic transition energy in matrices vs. gas phase, it is concluded that the C_{24}^- band at 3050 cm^{-1} (Ar) and the C_{36}^- band at 1640 cm^{-1} (Ar) could contribute to the UIR emissions located at 3.3 (3030 cm^{-1}) and 6.2 μm (1610 cm^{-1}). Figure 5-7 shows that other chains may also contribute to prominent UIR bands, to smaller peaks, or to the broad emission background. Clearly gas phase work is necessary to determine what impact these species might have on interstellar emission.

The attribution of C_{24}^- to the high energy wing of 3.3 μm UIR band points out a troubling problem with the prevailing PAH hypothesis. Recent theoretical and experimental studies[123-133] on the infrared absorption of the PAH cations have shown that the transition strength of the C-H stretch vibrations, to which the 3.3 μm band has been

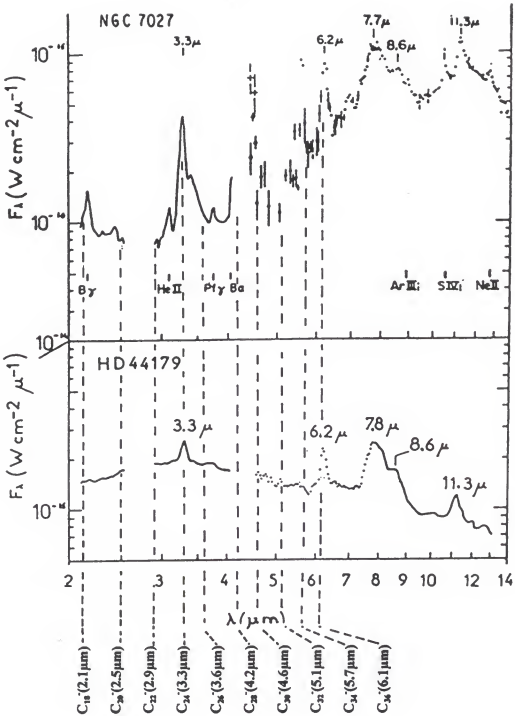

Figure 5-7. The infrared emission spectrum (UIR) recorded from planetary nebula NGC 7027 and HD44179. The positions of the 0-0 electronic transitions for chain carbon cluster anions C_n^- ($18 \leq n \leq 36$) from this work are indicated. UIR emission spectra taken from reference 17.

long assigned, are found to decrease drastically from that observed in neutral PAHs. In matrix studies the C-H stretches in the cations have not been observed, presumably because they have very small intensities and are masked by the intense bands from PAH neutrals. How then to account for the relatively intense 3.3 μm band observed from the ISM? A recent study[134] has shown that while the weaker features to lower energy of the 3.3 μm peak can be assigned to overtones of the C-H stretches in the PAHs, the main 3.3 μm band must originate from a different type oscillator. Observations of the spatial variations within the 3 μm region have also shown that the 3.3 μm peak intensity varies independently from the intensities of the 3.40 and 3.52 μm bands.[135] That the high energy wing of 3.3 μm band could arise from the electronic emission of the C_{24}^- species is consistent with this finding. Indeed, it may be that the other carbon chain anions are also emitting in this IR region, just with varying intensity.

Despite the above indications that long chain carbon anions may contribute to the UIR bands, it is necessary to ask whether these species meet certain observational criteria required of interstellar DIB candidates. In a critique of various proposed carriers of the DIBs, Snow used a set of critical factors against which each suggested carrier was judged (carbon chains were included).[136] These are: (1) Do carbon chains produce invariant wavelengths and profiles, and are they spectroscopically consistent with the observed UIR bands? (2) Are carbon chain anions able to form and survive under interstellar conditions? And, (3) are carbon chains consistent with cosmic abundances? The factors should be equally applicable to long carbon chains proposed as carriers of the UIR bands. Each carbon chain of specific length should produce a specific emission band. It is of course

still unknown whether these long chain anions emit in the infrared and what their radiative yields are. However, all chains, despite their charge, will possess a number of excited electronic states spread throughout UV, visible, and IR regions (naturally their number, type, and energy will depend on chain length). However, there does not exist at this time enough information on long carbon chains (charged or neutral) to accurately answer these questions.

While we have shown here that there are a few coincidences between the C_n^- ($18 < n < 36$) lowest electronic transition and a few UIR bands, there are a number of questions remaining which cannot be answered here. In particular, are the larger anion emission yields particularly enhanced compared to others in the series? And, is emission (fluorescence) observed only from one state or is a spin-forbidden emission (phosphorescence) observable (or being observed) also?

Vibrational

Along with the electronic bands covered in the previous section, absorption bands corresponding to the asymmetric stretch modes of several carbon cluster anions were seen and assigned. These bands appear at 1686.7 cm^{-1} (C_9^-), 1722.2 cm^{-1} (C_3^-), 1734.8 cm^{-1} (C_7^-), and 1936 cm^{-1} (C_6^-). Figures 5-1 and 5-8 show spectra where these bands appear, along with their assignments. Absorption bands do not appear for C_4^-, C_8, and C_8^-. C_8 has an extremely low intensity in carbon vaporization experiments, the reason for which is not yet understood. In fact the first C_8 band assignments were made only very recently.[108]

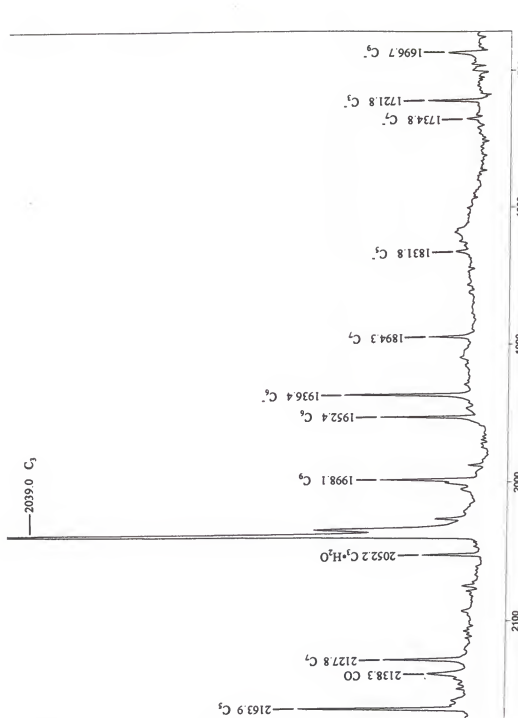

Figure 5-8. Portion of the infrared spectrum of C_n/C_n^- species trapped in an Ar matrix at 12K.

Since isotopomer experiments have not yet been conducted, the assignments have been based on cluster intensity distributions as a function of laser power, and tracking band intensity during annealing. While the experimental section described how the anions are differentiated from their neutral counterparts, the assignment of each band to a particular carbon cluster is not as straightforward. The matrix is made up of (at least) anionic and neutral carbon clusters. There is no reason to believe that the progressive change in the intensity distribution of carbon cluster bands during annealing will be any different from that seen when a matrix of all neutral clusters is annealed. This means that, under diffusion controlled conditions, carbon clusters will react with each other to gradually make larger and larger clusters over time. (It is assumed that an anion will react with a neutral but not another anion, conserving the total number of -1 charges). Indeed, this is seen experimentally. This method has been employed to understand which bands are due to smaller and larger carbon cluster anions.

Summary

The anions of even-membered carbon chains containing from 6 to 36 atoms have been produced by two different methods and studied in an argon matrix. The electronic transition wavelengths stretch from the visible (615.8 nm for C_6^-) to the infrared (6097.5 nm for C_{36}^-). Matrix UV photolysis has shown that the C_n^- clusters (with $n \geq 16$) appear to be resistant to photodestruction. A tentative, but reasonably good match has been found between two of the unidentified interstellar infrared emission bands at 3.3 μm and

6.2 μm and the cluster anions C_{24}^- and C_{36}^-, respectively. Other carbon chains may contribute to the underlying emission background and smaller features. Several other bands in the IR have been identified and assigned to the asymmetric stretch modes of the carbon cluster anions C_3^-, C_5^-, C_6^-, C_7^-, and C_9^-. However, isotopic substitution experiments will be necessary in order to definitively confirm these assignments.

CHAPTER 6
THEORETICAL STUDIES OF CARBON ANIONS

Introduction

The chemistry of pure carbon clusters has been the focus of a great deal of experimental and theoretical effort for a number of decades.[25] Since the mid-1980's a great deal has been learned about the geometric and electronic structure of small carbon clusters, C_n ($n < 20$). Larger carbon clusters like the fullerenes (especially C_{60}) and carbon nanotubes have practically become a field in themselves. This has been due, by and large, to the fact that milligram to gram quantities of these materials can be synthesized and are stable under ordinary conditions. On the other hand, carbon cluster ions have proven to be a little more difficult to characterize. The little experimental information that is known has been gathered through techniques such as ion cyclotron resonance,[137-140] coulombic explosion,[141-144] ESR,[145-149] and gas-phase ion mobility.[150-153] Yet, because a majority of the experiments have involved positive carbon ions, theory has provided most of the insight into carbon anions. Most of the theoretical effort has been spent refining itself to more accurately reproduce and expand on the experimentally known electronic states, electron affinities, and ionization energies.[154-159] Oddly, despite the thorough treatment carbon anions have received, no systematic study of carbon anion frequencies has been

published. Raghavachari has reported the calculated vibrational frequencies for C_3^-.[157] And, recently, Botschwina and Schmatz have reported the calculated symmetric frequencies for C_6^- and C_8^-.[160] To fill this void, the vibrational frequencies for linear and some cyclic carbon anions, C_n^- (n = 2-9), have been calculated at the B3LYP/6-31G* level. The results of these calculations will be compared to newly discovered experimental IR bands presented in Chapter 5.

Theoretical

All calculations have been carried out using the GAUSSIAN 94 program package.[91] The B3LYP exchange-correlation functional is used exclusively. This hybrid functional consists of the Lee-Yang-Parr[161] correlation functional and Becke's three parameter exchange functional.[162] The exchange functional is a linear combination of the local density approximation, Becke's gradient correction[163] and the 'exact' HF exchange energy. These hybrid methods have been shown to be more accurate than standard gradient corrected methods.[164] The 6-31G* basis set was also employed throughout. This basis set has been found to yield very similar geometries for neutral linear carbon clusters as the correlation consistent cc-pVDZ basis used by Martin, El-Yazal, and Francois.[165] Linear carbon anion geometries were constrained to be linear. Cyclic anions were optimized within their respective point groups which are listed in Table 6-6 and shown in Figure 6-3.

Results and Discussion

Linear Anions

The B3LYP/6-31G* geometries are presented in Figure 6-1. Total energies, spin-squared ($<S^2>$) eigenvalues, rotational constants, and zero-point energies for each anion studied are listed in Table 6-1. Table 6-2 lists the calculated vibrational frequencies and IR intensities for each mode. The geometries in Figure 6-1 are compared with the results of a ROHF/DZP study of carbon anions performed by Watts and Bartlett.[21] The geometries in both studies have a long/short bond alteration characteristic of a slightly acetylenic structure. This agrees with the prediction that cumulenic carbon neutrals become more acetylenic-like as electrons are added.[21,166] However, the alternation found here is not as pronounced as in the ROHF study. With the exception of C_2^-, the average B3LYP bond length is 0.004 to 0.01Å longer and the deviation from the average bond length is smaller than the ROHF structures.

In Table 6-3 are listed the experimental band positions and the carbon cluster anions to which they are assigned. To aid in the assignment vibrational frequencies for the linear carbon anions were calculated, the results of which are also listed in Table 6-3. A simple scaling factor (0.95) applied to the calculated band positions of these anions yields excellent agreement with experiment. The average deviation between experimental and calculated band positions is 19 cm^{-1}. This good agreement with experiment allows us to predict the band positions of anions that were not observed experimentally.

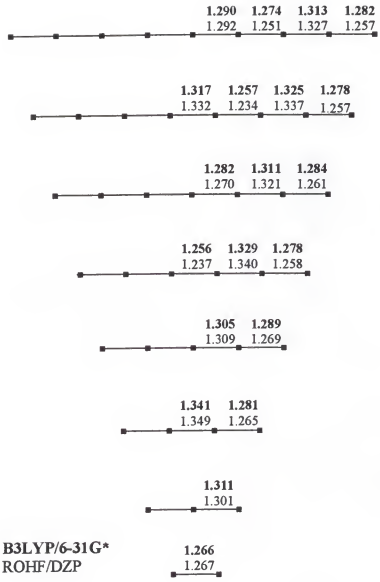

Figure 6-1. Linear carbon anion optimized geometries. Bond lengths in angstroms. B3LYP/6-31G* lengths in bold type, ROHF/6-31G* lengths from reference 166 in normal type.

Table 6-1. Linear carbon anion total energies (hartrees), zero-point energies (kcal/mol), rotational constants (GHz), spin squared values, in their ground electronic states calculated at the B3LYP/6-31G* level of theory.

	State	$\langle S^2 \rangle$	B3LYP/6-31G*	Rotational Constant	Z. P. E.
C^-	^4S	3.751	-37.844 27	---	---
C_2^-	$^2\Sigma_g^+$	0.753	-76.007 85	52.485338	2.677
C_3^-	$^2\Pi_g$	0.768	-114.097 77	12.238791	5.356
C_4^-	$^2\Pi_g$	0.760	-152.204 34	4.946407	9.249
C_5^-	$^2\Pi_u$	0.779	-190.289 53	2.495564	12.244
C_6^-	$^2\Pi_u$	0.766	-228.383 63	1.432485	16.396
C_7^-	$^2\Pi_g$	0.790	-266.465 31	0.899969	19.456
C_8^-	$^2\Pi_g$	0.771	-304.554 87	0.601110	23.738
C_9^-	$^2\Pi_u$	0.801	-342.635 31	0.422028	26.678

Table 6-2. Vibrational frequencies (cm^{-1}), IR intensities (km/mol), and symmetries for linear carbon anions C_n (n=2-9) calculated at the B3LYP/6-31G* level of theory.

C_2^-	1872.7 (0) σ_g
C_3^-	1772.1 (152) σ_u, 1201.9 (0) σ_g, 453.4 (28) π_u, 319.1 (40) π_u
C_4^-	2112.7 (0) σ_g, 1785.2 (87) σ_u, 926.4 (0) σ_g, 605.4 (0) π_g, 533.1 (0) π_g, 265.5 (27) π_u, 241.5 (50) π_u
C_5^-	1923.7 (0) σ_g, 1902.5 (855) σ_u, 1472.6 (23) σ_u, 777.2 (0) σ_g, 751.7 (0), 604.9 (8), 432.6 (0) π_g, 360.7 (0) π_g, 170.9 (35), 167.8 (24)
C_6^-	2193.2 (0) σ_g, 2036.6 (726) σ_u, 1865.4 (0) σ_g, 1222.4 (1) σ_u, 810.5 (0), 774.7 (0), 657.9 (0) σ_g, 553.4 (3), 516.6 (12), 293.4 (0), 285.0 (0), 132.8 (24), 127.4 (30)
C_7^-	2079.6 (0) σ_g, 1990.1 (157) σ_u, 1835.7 (2331) σ_u, 1608.7 (0) σ_g, 1089.9 (8) σ_u, 929.1 (2), 827.7 (3), 669.4 (0), 582.0 (0), 577.8 (0) σ_g, 416.3 (8) π_u, 367.4 (12) π_u, 226.4 (0), 221.1 (0), 94.6 (20), 93.6 (23)
C_8^-	2174.8 (1563) σ_u, 2160.2 (0) σ_g, 2029.4 (0) σ_g, 1882.1 (512) σ_u, 1383.8 (0) σ_g, 983.5 (0), 964.4 (17) σ_u, 963.0 (0), 721.0 (1), 702.4 (0), 515.7 (0), 507.5 (0) σ_g, 489.5 (0), 306.6 (18), 303.5 (10), 187.6 (0), 181.7 (0), 74.6 (17), 73.5 (19)
C_9^-	2147.5 (0) σ_g, 2083.1 (262) σ_u, 1941.1 (0) σ_g, 1814.9 (4201) σ_u, 1664.0 (728) σ_u, 1268.0 (0) σ_u, 1268.0 (0) σ_g, 1052.5 (3), 979.9 (1), 877.3 (132) σ_u, 806.8 (0), 732.7 (0), 603.4 (1), 542.5 (2), 547.4 (0) σ_g, 401.4 (0) π_g, 367.1 (0) π_g, 258.8 (16), 250.2 (11), 148.9 (0), 147.1 (0), 58.2 (14), 58.0 (15)

Table 6-3. A comparison of experimental and select calculated linear carbon anion bands. Frequencies in cm^{-1}, intensities in km/mol.

		B3LYP/6-31G*			
	Experiment	scaled (0.95)	unscaled	IR intensity	Δ (E-T)[b]
C_2^-	1781.2[a]	1779.1	1872.7	0	2.1
C_3^-	1722.0	1683.5	1772.1	152	38.5
C_4^-		1695.9	1785.2	87	
C_5^-	1831.9	1807.4	1902.5	855	24.5
			1472.6	23	
C_6^-	1936.8	1934.7	2036.6	726	2.1
C_7^-			1990.1	157	
	1734.9	1743.9	1835.7	2331	-9.0
C_8^-		2066.0	2174.8	1563	
			1882.1	512	
C_9^-			2083.1	262	
	1686.8	1724.1	1814.9	4201	-37.3
			1664.0	728	
			877.3	132	

[a] Gas phase. From reference 167.

[b] Experimental minus scaled theoretical values.

Two anions (C_4^- and C_8^-) are not observed experimentally. C_4 is a relatively low intensity peak and C_8 is almost never seen. This is due either to low concentration or a weak oscillator strength. Any anions that are formed are going to be a small percentage of the neutral (~10%), so if C_4 and C_8 are not produced in abundance the anion concentration will be extremely low, making them even more difficult to detect. Even though they are not seen experimentally, bands for C_4^- and C_8^- are predicted to exist near 1696 cm^{-1} and 2066 cm^{-1}, respectively (Table 6-3).

Pitzer and Clementi[44] calculated that reactions between neutral carbon clusters occur with no apparent activation energy and are strongly exothermic. But can the same be said about the reaction between anionic and neutral clusters? To better understand these reactions, calculations have been run to estimate the thermochemistry of the reaction $C_n + C_m^- \rightarrow C_{n+m}^-$ (n,m = 1 to 8). Reaction energies are collected in Table 6-5 and represented graphically in Figure 6-2. (The results of the reactions between neutral carbon clusters at the B3LYP/6-31G* level are shown in Table 6-4). Zero point corrections were left out of these energies as they amounted to a small fraction of the total reaction energy ($\leq$5%). All of these reactions are highly exothermic, in fact more exothermic than the analogous reactions between their corresponding neutral clusters. Furthermore, aggregation reactions between anionic carbon clusters and even-numbered neutral clusters are predicted to be 20 to 30% more exothermic than reactions between anionic carbon clusters with odd-numbered neutral clusters. These findings are consistent with experimental observation (Chapter 5).

Table 6-4. Energies of reaction (kcal/mol) between neutral linear carbon chains ($n_{product} \leq 9$ atoms) calculated at the B3LYP/6-31G* level of theory. Not zero-point corrected.

	$C(^3P)$	C_2	C_3	C_4
$C(^3P)$	-119.1	---	---	---
C_2 ($^1\Sigma_g^+$)	-199.2	-168.2	---	---
C_3 ($^1\Sigma_g^+$)	-88.1	-173.4	-104.7	---
C_4 ($^3\Sigma_g^-$)	-204.3	-215.8	-173.3	-223.6
C_5 ($^1\Sigma_g^+$)	-130.5	-172.1	-107.5	-176.5
C_6 ($^3\Sigma_g^-$)	-160.7	-176.0	-134.1	
C_7 ($^1\Sigma_g^-$)	-134.5	-172.6		
C_8 ($^3\Sigma_g^-$)	-157.2			

Table 6-5. Energies of reaction[a] (kcal/mol) between linear carbon neutrals (abscissa) and linear carbon anions (ordinate) yielding a longer linear carbon anion. Calculated at the B3LYP/6-31G*level of theory. Electronic states in parenthesis.

	$C\ (^3P)$	$C_2\ (^1\Sigma_g^+)$	$C_3\ (^1\Sigma_g^+)$	$C_4\ (^3\Sigma_g^-)$	$C_5\ (^1\Sigma_g^+)$	$C_6\ (^3\Sigma_g^-)$	$C_7\ (^1\Sigma_g^+)$	$C_8\ (^3\Sigma_g^-)$	$C_9\ (^1\Sigma_g^+)$
$C^-\ (^4S)$	-199.1	-232.9	-197.0	-258.8	-209.9	-227.1	-219.1	-231.5	-225.4
$C_2^-\ (^2\Sigma_g^+)$	-152.8	-197.0	-147.8	-215.2	-158.5	-180.6	-166.9	-183.5	
$C_3^-\ (^2\Pi_g)$	-163.2	-194.1	-150.5	-210.0	-158.3	-174.7	-165.1		
$C_4^-\ (^2\Pi_g)$	-150.0	-186.3	-134.9	-199.4	-142.0	-162.5			
$C_5^-\ (^2\Pi_u)$	-155.6	-184.1	-137.6	-196.3	-143.1				
$C_6^-\ (^2\Pi_u)$	-147.7	-181.2	-129.0	-191.9					
$C_7^-\ (^2\Pi_g)$	-152.6	-180.4	-132.4						
$C_8^-\ (^2\Pi_g)$	-146.9	-299.9							
$C_9^-\ (^2\Pi_u)$	-224.1								

[a] Not zero-point corrected.

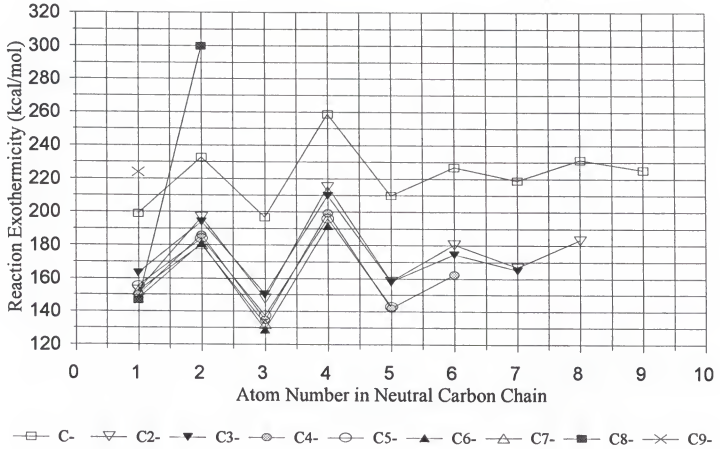

Figure 6-2. Plot of the exothermicity of the reaction between neutral carbon cluster chains (ordinate) and anionic carbon chains (in graph). Note the larger exothermictiy for reactions with even numbered neutral chains.

Cyclic Anions

Cyclic C_3^-. A D_{3h} and two C_{2v} structures are possible for cyclic C_3. However, the D_{3h} structure could not be located at this level of theory. The C_{2v} structure, **A**, was found to be a stable minimum 14.4 kcal/mol higher in energy than the linear isomer. The other C_{2v} structure, **B,** was found to be a first order saddle point whose energy lowering mode of motion yielded the stable minimum **A**.

Cyclic C_4^-. Five nonlinear structures were investigated, but only three minima were located. The lowest energy structure of these five, **D**, involves a three membered ring and has C_{2v} symmetry. It is 37.7 kcal/mol higher in energy than the linear structure. A Mulliken population analysis indicates that half of the total charge resides on the terminal carbon on the 'stem' of the ring. The next most stable isomer, **E**, is a planar diamond-shaped structure having D_{2h} symmetry. It is predicted to lie 39.0 kcal/mol higher in energy than the linear form. This separation is considerably larger than the 13.8 kcal/mol difference predicted by Hutter, Luthi, and Deiderich[121] between the corresponding neutrals. The last local minimum, **C**, is similar to the previous isomer except that it is a nonplanar diamond-shaped structure having C_{2v} symmetry. This isomer is less elongated and is 18.7 kcal/mol higher in energy than E (+57.7 kcal/mol with respect to the linear isomer). The shortest distance between opposite points in this ring is 1.7Å (Figure 6-3). This distance would suggest that no bond is formed across the ring. One structure, a rectangular shaped structure with D_{2h} symmetry, was located but found to be a third order saddle point. Two of these imaginary modes were doubly degenerate and

A (C_{2v})

B (C_{2v})

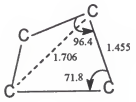

dihedral = 133.9

C (C_{2v})

D (C_{2v})

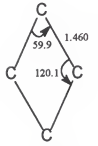

E (D_{2h})

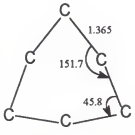

F (D_{3h})

Figure 6-3. Optimized structures of all stable cyclic anion structures found at the B3LYP/6-31G* level of theory.

Table 6-6. Symmetries, total energies (hartrees), spin squared values, zero-point energies (kcal/mol), and the number of imaginary frequencies[a] (*iv*) found for each of the cyclic carbon anion species.

Isomer	Sym.	B3LYP/6-31G*	Relative Energy[b]	$< S^2 >$	Z.P.E.	*iv*
A	C_{2v}	-114.074 86	14.4	0.753	4.6	0
B	C_{2v}	-114.072 46	15.9	0.754	3.9	1
C	C_{2v}	-152.112 36	57.7	0.763	6.8	0
D	C_{2v}	-152.148 98	37.7	0.758	9.1	0
E	D_{2h}	-152.142 17	39.0	0.762	6.7	0
F	D_{3h}	-228.326 52	35.8	0.757	15.4	0

[a] Only isomers with one or no imaginary frequencies are listed.
[b] Energy relative to the linear isomer.

Table 6-7. Vibrational frequencies of the cyclic carbon anions calculated at the B3LYP/6-31G* level. Frequencies are in cm^{-1} and intensities are in km/mol.

A	768.5 (0), 935.9 (53), 1558.9 (14)
B	763.7i (617), 1154.0 (27), 1591.0 (1)
C	124.9 (0), 564.4 (8), 736.9 (105), 802.0 (9), 1247.0 (5), 1290.5 (1)
D	371.1 (1), 506.6 (4), 779.7 (50), 1334.5 (2), 1683.9 (1901), 1716.3 (0)
E	185.3 (0), 483.1 (35), 506.0 (39), 1006.0 (0), 1208.7 (6), 1324.3 (0)
F	451.9 (16), 552.6 (0), 552.6 (0), 598.6 (0), 600.3 (0), 600.3 (0), 919.9 (60), 920.2 (60), 1127.9 (0), 1245.5 (0), 1609.1 (275), 1609.1 (275)

lead to the planar diamond structure. The third imaginary mode involves a C-C bond rupture, creating a linear-like isomer. The last isomer sought was a pyrimidal structure with C_{3v} symmetry, but no stable structure was located, and this isomer is presumed not to exist.

Cyclic C_6^-. Four six-membered ring structures were investigated, but only two stationary points were found. The lowest energy cyclic C_6^- isomer, **F**, is a planar ring having D_{3h} symmetry, and is also the only stable minimum found. Unlike their neutral counterparts which were nearly isoenergetic, **F** is predicted to be 35.8 kcal/mol higher in energy than the linear form. A planar D_{6h} isomer was located, and found to be a second order saddle point 59.9 kcal/mol higher in energy than the linear form. The imaginary frequencies represent a doubly degenerate motion both of which lead to the D_{3h} minimum. Two other geometries were tested, neither of which yielded a stationary point. The first is a six-membered ring in the 'boat' conformation. This geometry consistently reverted to a D_{3h}-like structure. The second was an arrangement of carbon atoms with octahedral symmetry. No stable geometry in the O_h point group was found.

Vibrational frequencies. The calculated vibrational frequencies for each cyclic minima found are presented in Table 6-7. These calculations were run in order to determine if cyclic C_n^- isomers are present in the laser vaporization experiments and if they are causing any of the IR bands seen. From the data in Table 6-7, it seems unlikely that cyclic isomers are causing or even contributing to the experimental bands listed in Table 6-3. All of the IR active bands are predicted to lie below 1700 cm^{-1}, and of those only the 1683.9 cm^{-1} band of isomer **D** lies near the range of the experimental bands. This is also

the only band with an intensity comparable to the linear anions, therefore would be the most likely band to be seen. Compounding the case against the cyclic anions is the fact that they are calculated to be higher in energy than the linear anions. This is especially true as the number of carbons in the ring increases.

Summary

In conjunction with an experimental study, vibrational frequencies for linear carbon anions C_n^- (n = 2-9) have been calculated at the B3LYP/6-31G* level. Remarkably good agreement with the experimentally assigned bands is found (ave. dev. = 19 cm^{-1}), and predictions of band positions for those anions which are not observed are made. To investigate if cyclic carbon anions are present in the experiment, calculations on several cyclic C_n^- (n = 3, 4, 6) isomers have been carried out. Based on the relative stabilities of the cyclic and linear anions and the predicted positions of vibrational frequencies, it is concluded that no cyclic isomers are present in the laser vaporization matrix isolation experiments.

CHAPTER 7
THEORETICAL STUDIES OF C_3 ISOLATED IN AN ARGON MATRIX

Introduction

It has recently been reported that C_3 embedded in Ar and Kr matrices is bent with a bond angle of ~160°.[168] Vapor phase C_3 is known to be linear, but is considered to be a very floppy molecule (its potential energy surface in the bending coordinate is very broad).[31-33] Because of the geometry difference in the two phases, it was of interest to determine how the presence of the rare gas atoms in close proximity to the C_3 molecule could cause the observed molecular bending. Was a C_3•Ar (or Kr) complex formed whose geometry favored a bent C_3 or were there matrix (i.e. packing) forces present in the rare gas lattice which were sufficiently strong to lead to a bent C_3? *Ab initio* calculations were performed to determine whether one Ar atom, held in close proximity to the C_3 molecule, would be sufficient to bend the C_3. This approach was taken recently by Schleyer and coworkers[169] on CaX_2 (X = F, H) and Lakhlifl and coworkers[170,171] on ozone to understand how the approach of an "inert" atom/molecule such as Ne, Ar, Kr, Xe, CO, or N_2 may lead to weak interactions and perturbation of the geometry of the guest species.

Theoretical

The *ab inito* calculations were carried out using the GAUSSIAN 94 program package.[91] Three different C_3•Ar interaction geometries were considered: Ar with the terminal carbon ($C_{\infty v}$ complex symmetry), with the central carbon (C_{2v} complex symmetry), and an Ar bridging the central and a terminal carbons (C_s complex symmetry). The three geometries are illustrated below in Figure 7-1. All calculations were run at the

Figure 7-1.

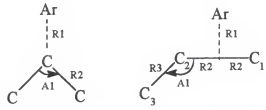

MP2/6-31G* level. Optimized geometries for all three complexes were found, then total energies as a function of C-Ar distance were calculated. At each point the C-Ar distance was fixed and the rest of the parameters (shown in Figure 7-1) were allowed to fully optimize within the constraints of the point group. Total energies, optimized parameters, and Mulliken charges for each of the three orientations are given in Tables 7-1 to 7-3.

Results

In all three orientations the fully optimized geometries have a C-Ar distance of ca. 3.9Å and show virtually no bending of the C_3. The C_3•Ar complexes are, as might be

Table 7-1. Total energies (hartrees), relative energies (kcal/mol), geometric parameters (in angstroms and degrees), and Mullikin charges for the central carbon--argon orientation as a function of C_3-Ar distance.

C_3--Ar distance	MP2/6-31G*	Relative Energy[a]	Geometric Parameters			Mulliken Charges		
			R1	R2	A1	Ar	C(central)	C(terminal)
Full opt.	-640.603 70	0.0	3.921	1.304	180.4	0.0	-0.35	0.175
1.5Å	-640.410 73	121.1	1.5	1.352	71.0	0.641	-0.433	-0.104
2.0Å	-640.541 51	39.0	2.0	1.318	86.2	0.199	-0.263	0.032
2.5Å	-640.586 04	11.1	2.5	1.308	108.7	0.033	-0.301	0.134
3.0Å	-640.600 02	2.3	3.0	1.305	165.0	0.002	-0.372	0.185
3.5Å	-640.603 35	0.2	3.5	1.304	177.8	0.0	-0.349	0.175
4.5Å	-640.603 55	0.1	4.5	1.304	180.4	0.0	-0.35	0.175
6.0Å	-640.603 38	0.2	6.0	1.304	180.2	0.0	-0.35	0.175

[a] Energy in kcal/mol relative to the completely optimized C_3•Ar complex.

Table 7-2. Total energies (hartrees), relative energies (kcal/mol), geometric parameters (in angstroms and degrees), and Mullikin charges for the bridging carbon--argon orientation as a function of C_3-Ar distance.

C_3--Ar distance	MP2/6-31G*	Relative Energy[a]	Geometric Parameters				Mulliken Charges			
			R1	R2	R3	A1	Ar	C_1	C_2	C_3
Full opt.	-640.603 72	0.0	3.886	0.652	1.304	179.6	0.0	0.175	-0.350	0.175
1.5Å	-640.240 63	227.8	1.5	0.710	1.315	160.3	0.627	0.020	-0.526	-0.121
2.0Å	-640.493 55	69.1	2.0	0.655	1.300	150.7	0.174	0.176	-0.433	0.083
2.5Å	-640.580 78	14.4	2.5	0.652	1.303	159.5	0.032	0.201	-0.395	0.162
3.0Å	-640.600 14	2.2	3.0	0.652	1.304	172.2	0.003	0.181	-0.357	0.173
3.5Å	-640.603 44	0.2	3.5	0.652	1.304	178.6	0.0	0.176	-0.350	0.175
4.5Å	-640.603 55	0.1	4.5	0.652	1.304	179.9	0.0	0.175	-0.351	0.175
6.0Å	-640.603 38	0.2	6.0	0.652	1.304	179.9	0.0	0.175	-0.351	0.175

[a] Energy in kcal/mol and relative to the fully optimized C_3•Ar complex.

Table 7-3. Total energies (hartrees), relative energies (kcal/mol), geometric parameters (in angstroms and degrees), and Mullikin charges for the terminal carbon--argon orientation as a function of C_3-Ar distance.

C_3--Ar distance	MP2/6-31G*	Relative Energy[a]	Geometric Parameters			Mulliken Charges			
			R1	R2	R3	Ar	C_1	C_2	C_3
Full opt.	-640.603 68	0.0	3.923	1.304	1.304	0.0	0.172	-0.347	0.175
1.5Å	-640.314 49	181.5	1.5	1.281	1.331	0.644	-0.494	0.043	-0.194
2.0Å	-640.312 12	182.9	2.0	1.299	1.346	0.427	-0.305	0.046	-0.168
2.5Å	-640.577 07	16.7	2.5	1.308	1.304	0.005	0.211	-0.372	0.156
3.0Å	-640.599 53	2.6	3.0	1.305	1.304	-0.005	0.183	-0.345	0.167
3.5Å	-640.603 33	0.2	3.5	1.304	1.304	-0.002	0.171	-0.343	0.173
4.5Å	-640.603 54	0.1	4.5	1.304	1.304	0.0	0.175	-0.351	0.175
6.0Å	-640.603 38	0.2	6.0	1.304	1.304	0.0	0.175	-0.351	0.175

[a] Energy in kcal/mol and relative to the fully optimized C_3•Ar complex.

expected, very weakly bound by only 0.8 kJ/mol. Significant C_3 bending in the central and bridging orientations does not occur until the Ar is at a fixed distance of ca. 2.5Å. The central carbon interaction shows a smooth collapse of the angle A1 as the Ar atom approaches. The same cannot be said about the bridging orientation. As the Ar atom approaches, the bond angle A1 decreases to 150.7° at 2.0Å but then opens slightly to 160.3° at 1.5Å. This is not indicative of a local minimum as the total energy continues to increase at every point as the Ar atom approaches. This unexpected bending behavior could be due to the rearrangement of charge within the C_3•Ar complex. Between 2.0 and 1.5Å - where the bond angle opens up from 150 to 160°- a substantial amount of positive charge builds up on the Ar atom (+0.174 to +0.64) and there is a charge sign change on the carbon (C3) farthest from the Ar. There is no bending angle in the terminal carbon orientation. However, the bending potential of the C_3 as a function of C-Ar distance was calculated and is shown in Figure 7-2. The bending potential increases (as a single well) as the Ar approaches. Yet the increase in total energy for a given bond angle and Ar distance is not as much as the total energy increases found in the central and bridging orientations.

As shown in Figure 7-3 the central and bridging orientations have smoothly increasing total energies from the equilibrium geometries (~3.9Å). The terminal carbon orientation is expected to increase more rapidly due to the fact that it was not allowed to 'relax', i.e. bend in response to the Ar approach. This fact is borne out by the calculations, however, the energy plateaus at C-Ar distances < 2.0Å. Unfortunately, this unexpected behavior cannot be explained at this time.

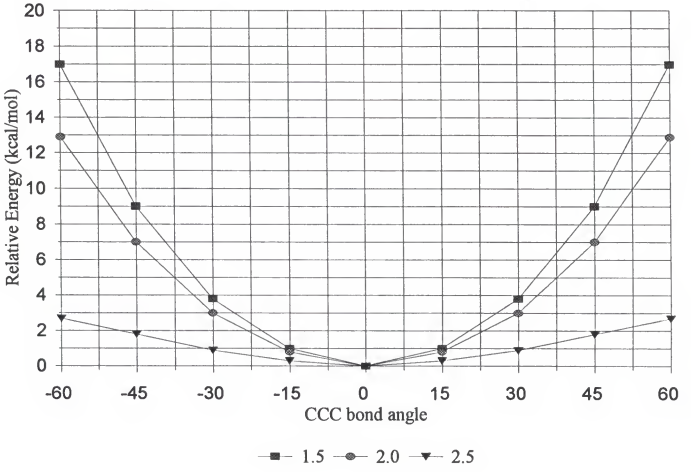

Figure 7-2. Potential energy for the bending of C_3 in the terminal orientation as a function of C-Ar distance. Energies are relative to the linear (CCC bond angle = 0°).

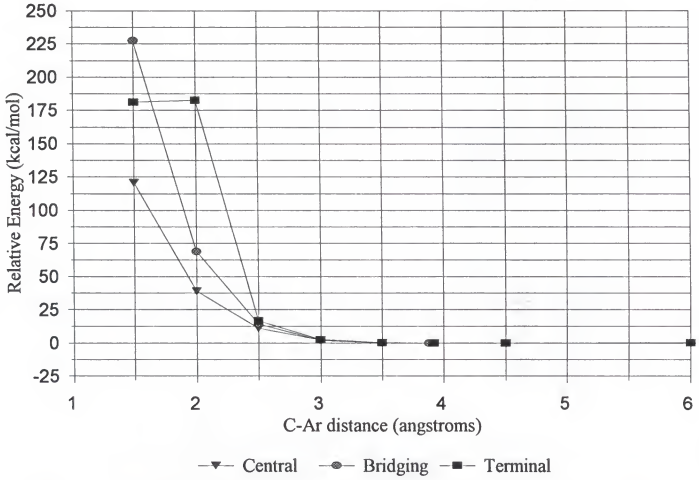

Figure 7-3. Interaction energies between C_3 and Ar in the central, bridging, and terminal orientations. Energies are relative to the completely optimized C_3•Ar complex.

Discussion

We can compare this constrained near neighbor model with the guest/host structure in order to gauge (to a first approximation) what effect the matrix itself might have on C_3. Using the calculated bond length for C_3 of 1.304Å plus an van der Waal orbital extension on the terminal carbons of 0.5Å we arrive at a total length for C_3 of 3.608Å. This is close to the site diameter[172] of 3.76Å which is created by removing one argon atom from its cubic closest packed crystal structure. This extremely crowded arrangement is almost certain to have a physical effect on the C_3. Even when larger sites are considered there is still a rather close arrangement of Ar atoms around the C_3. If a substitutional and an interstitial site are combined, the total cavity length would be 5.31Å. Subtracting the length of the C_3 molecule leaves a mere 0.8Å clearance at each end of the C_3. A doubly substituted site would have a 7.52Å total length. This increases the clearance on each end of the C_3 to 1.9Å. Even this distance lies well within the range of just one Ar atom highly perturbing the C_3 molecule. In addition, if we take the diameter of a C_3 molecule to be 1.2Å, there will only be a clearance of 1.28Å from the side of the C_3 to the nearest Ar neighbor.

Thus, it is clear that such a close arrangement of even one host atom near a C_3 will perturb it enough to force a geometry change. Which one of the three orientations has the greatest influence on the C_3 is not known; however, it is likely that some combination of all three is taking place.

CHAPTER 8
FUTURE WORK

It is tempting to note the excellent correlation between band positions for several polycyclic aromatic hydrocarbons (PAHs) and the positions of the unidentified interstellar emission bands (UIRs), then declare victory over this astrophysical problem. Actually, the question of the carrier of the UIRs is far from being solved. A great deal of debate still exists over the ion/neutral ratio, sizes, or even if PAHs alone account for the UIRs. Considering the high abundance of carbon in space ($n_C = 10^{-4}\ n_H$)[173] it would seem reasonable to believe that the carrier(s) of the UIRs is/are some kind of carbon-based material containing hydrogen. Proposed candidates are the PAHs, highly unsaturated carbon chain molecules,[112,174] C_nH_m ($n > 2$ (even), $m < 3$), and the bare carbon chains proposed here.

The UIR emission spectrum is a series of sharp bands at 3.3, 6.2, 7.7, 8.7, and 11.3 μm built on a emission continuum. This observation presents a double-edged problem. The sharp bands must be due to a small group of similar species emitting at very similar wavelengths, yet the continuum must be due to a mixture of molecules with very different emission characteristics whose bands overlap. Despite the characteristic nature of the prominent emission bands (i.e. 3.3 μm is assigned to a C-H stretch motion) it would seem unlikely that a broad distribution of unrelated molecules could coincidently emit at the

same wavelengths. The various structures would have different internal temperatures yielding a variety of band lineshapes and red shifts. A mixture of molecules almost certainly cannot exist without broadening the sharp emission bands. Therefore, it has been proposed that a family of similar molecules could be responsible for the UIRs.[181] Cook *et al.*[175] have shown that even a family of PAHs can have radically different IR emission spectra (Figure 8-1). In fact it was their conclusion that small and medium sized neutral PAHs (less than 25 carbon atoms) could not account for the observed UIRs.[133,175] They based their conclusion on the fact that, while the 3.3 μm band was invariant, the emission in the 6.2, 7.7, 8.7, and 11.3 μm bands could only account for ca. 10% of the emission from space. Hudgins and Allamandola[116i] have recently concluded that the reason why Cook *et al.*[175] and Schlemmer *et al.*[133] discounted neutral PAHs was because the UIRs are consistent with ionized PAHs. They go on to support this view by comparing the relative intensities seen in the UIRs with a mixture of PAH cation and neutral intensities. It is known[123-133,135] that ionized PAHs exhibit absorption bands very close to neutrals but with very different intensities. Although it is not known exactly why, the PAH cation 6.2, 7.7, and 8.7 μm bands are much more intense than the corresponding neutral, while the 3.3 μm band intensity decreases dramatically. The PAH population in interstellar space is expected to be 10 to 90% ionized depending on the flux of high energy photons available in the region.[16,176,177] So the ion/neutral mixture hypothesis seems to be a credible model.

The prevailing hypothesis on PAHs as the carrier of the UIRs is the following. A mixture of ions and neutrals absorb UV and/or optical photons. Internal conversion and intersystem crossing on a time scale shorter than UV fluorescence redistributes the

absorbed energy among the various vibrational modes of the molecule. Finally, the highly vibrationally excited molecule loses energy via infrared emission at wavelengths characteristic of the particular mode and internal temperature from which the photon is emitted. Experimental observations of the emission spectra of neutral gas-phase PAH molecules excited by UV photons are consistent with this model.[133,135,175,178-180]

However, a very interesting experiment was recently reported by Boissel, Lefevre, and Thiebot.[181] In this experiment they showed that small gas-phase PAH cations actually fragment when exposed to UV/VIS photolysis. The anthracene cation was seen to lose a mass equal to acetylene, and the pyrene cation lost a mass corresponding to two H atoms. This behavior was not seen in matrix isolation experiments with PAH cations. The implication that small PAH cations might not be stable to photolysis is extremely important. This means that both small neutral and cation PAHs cannot be carriers of the UIR bands. Interestingly, it was suspected that, much like the experimental H loss from pyrene, PAHs might be highly dehydrogenated. This simple conclusion is based on a comparison of the intensities of the C-C modes to the C-H modes in the UIRs.[16,17] This dehydrogenation was also predicted by photothermodissociation models.[182] Yet, like most aspects of the UIRs, Hudgins and Allamandola[131] state that the dehydrogenation mechanism seems unreasonable since the abundance of hydrogen in the zones where UIRs are observed is 10,000 times that of the PAH abundance.

The future work proposed here is extremely basic but impacts fundamentally on the very model of the UIR carriers. These experiments would seek to understand the behavior of ions suspected of being the carriers of the UIRs when exposed to UV radiation. The

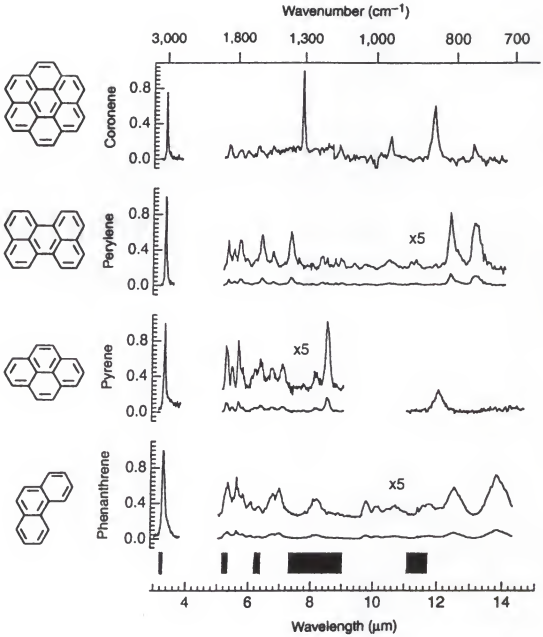

Figure 8-1. Infrared emission spectra of several unsubstituted PAH molecules. Black bands at the bottom represent wavelengths where UIRs are observed. Spectra were recorded using the single-photon infrared emission spectroscopy (SPIRES) technique. Figure from reference 175.

species would include PAHs of various sizes and saturation as well as bare carbon chains. First, the parent ions of various PAH ions should be trapped in an ICR mass spectrometer cell, and their photostability studied. This is essentially a repeat of the Boissel, Lefevre, and Thiebot experiment. PAHs of various sizes should be studied and the fragmentation patterns determined so trends in stability (if any) can be noted. Next, carbon anions should be produced in an ICR cell so that their photostability can be tested. The results of this experiment will determine which (if any) of the carbon anions can be suggested as a UIR carrier(s). Once these experiments have been completed another stability experiment on $C_nH_m^-$ molecules can be conducted. These molecules should be able to be created by introducing H_2 into an ICR cell loaded with C_n^- species. Addition of a neutral in this manner is a typical ICR technique and should yield the partially hydrogenated $C_nH_m^-$ molecules. The last experiment is slightly more complex. It would be extremely helpful to have emission spectra of these ions under astrophysical conditions. It is proposed here that IR emission experiments on gas-phase ions be performed. This is a nontrivial experiment with challenges such as being able to generate enough of the ions of interest, finding a suitable detector, and cryogenically cooling many parts to reduce the IR background. While the ICR cell is an excellent place to trap ions for seconds or even minutes in the gas phase the large magnetic field used is not typical of the interstellar medium. The effect that this field will have on emission, or even fluorescence, from high lying densely populated states in these species is unknown and may have to be gauged with experiments that vary the magnetic field strength. Finally, *ab initio* calculations can be performed on these molecules to help understand structures in the ground and excited

states, absorption and emission spectra, and fragmentation dynamics. Even though theory has been employed,[124,128] it has played only a supporting role in characterizing PAH absorption bands.

REFERENCES

1. Wittle, E.; Dows, D. A.; Pimentel, G. C. *J. Chem. Phys.* **1954**, *22*, 1943.

2. Ball, D. W.; Kafafi, Z. H.; Fredin, L.; Hauge, R. H.; Margrave, J. L. *A Bibliography of Matrix Isolation Spectroscopy*, Rice Universtiy Press: Houston, 1987.

3. Andrews, L.; Moskovits, M. *Chemistry and Physics of Matrix-Isolated Species*, North-Holland: Amsterdam, 1989.

4. McPherson, D. W.; McKee, M. L.; Shevlin, P. B. *J. Am. Chem. Soc.* **1983**, *105*, 6493.

5. Jenniskens, P.; Desert, F. X. *Astron. Astrophys. Suppl. Ser.* **1994**, *106*, 39.

6. Merrill, P.W. *Publ. Astron. Soc. Pac.* **1934**, *46*, 206.

7. Smith, W. H.; Snow, T. P.; York, D. G. *Astrophys. J.* **1977**, *218*, 124.

8. Douglas, A. E. *Nature* **1977**, *269*, 130.

9. Thaddeus, P.; Gottlieb, C. A.; Mollaaghababa, R.; Vrtilek, J. M. *J. Chem. Soc. Faraday Trans.* **1993**, *89*, 2125.

10. Van der Zwet, G. P.; Allamandola, L. J. *Astron. Astrophys.* **1985**, *146*, 76.

11. Foing, B. H.; Ehrenfreund, P. *Nature* **1994**, *369*, 296.

12. Sorokin, P. P.; Glowina, J. H. *Chem. Phys. Lett.* **1995**, *234*, 1.

13. Hinnen, P. C.; Ubachs, W. *Chem. Phys. Lett.* **1995**, *240*, 351.

14. Gillett, F. C.; Forrest, W. J.; Merrill, K. M. *Astrophys. J.* **1973**, *183*, 87.

15. Russell, R.; Soifer, B.; Willner, S. *Astrophys. J.* **1977**, *217*, L149.

16. Allamandola, L. J.; Tielens, A. G. G.M.; Barker, J. R. *Astrophys. J.* **1985**, *290*, L25.

17. Leger, A.; Puget, J. L. *Astron. Astrophys.* **1984**, *137*, L5.

18. Leger, A.; d'Hendecourt, L. *NATO ASI Ser. C (Polycyclic Aromatic Hydrocarbons and Astrophysics)*, Leger, A.; d'Hendecourt, L.; Boccara, N. Eds. 1987, p. 234, No. 191.

19. Clar, E. *Polycyclic Hydrocarbons*. Academic Press: New York, 1964.

20. Yang, S.; Taylor, K. J.; Craycraft, M. J.; Conceicao, J.; Pettiette, C.L.; Cheshnovsky, O.; Smalley, R. E. *Chem. Phys. Lett.* **1988**, *144*, 431.

21. Watts, J. D.; Bartlett, R. J. *J. Chem. Phys.* **1992**, *97*, 3445.

22. Wellegehausen, B.; Hube, M.; Jin, F. *Appl. Phys. B*, **1989**, *49*, 173.

23. Weltner, W., Jr.; Walsh, P. N.; Angell, C. L. *J. Chem. Phys.* **1964**, *40*, 1299.

24. Weltner, W., Jr.; McLeod, D., Jr. *J. Chem. Phys.* **1964**, *40*, 1305.

25. Weltner, W., Jr.; Van Zee, R. *Chem. Rev.* **1986**, *89*, 1713.

26. Federman, S. R.; Huntress, W. T. *Astrophys. J.* **1989**, *338*, 140.

27. Gredel, R.; van Dishoeck, E. F.; Blacl, J. H. *Astrophys. J.* **1989**, *338*, 1047.

28. Goebel, J. H.; Bergman, J. D.; Cooper, D. M.; Goorvitch, D.; Langhoff, S. R.; Witteborn, F. C. *Astrophys. J.* **1983**, *270*, 190.

29. Bernath, P. F.; Hinkle, K. H.; Keady, J. J. *Science* **1989**, *244*, 562.

30. Hare, J. P.; Kroto, H. W. *Acc. Chem. Res.* **1992**, *25*, 106.

31. Rohlfing, E. A.; Goldsmith, J. E. M. *J. Opt. Soc. Am.* **1990**, *B7*, 1915.

32. Northrup, F. J.; Sears, T. J. *J. Opt. Soc. Am.* **1990**, *B7*, 1924.

33. Jensen, P.; Rohlfing, C. M.; Amlof, J. *J. Chem. Phys.* **1992**, *97*, 3399.

34. Northrup, F. J.; Sears, T. J.; Rohlfing, E. A. *J. Mol. Spectrosc.* **1991**, *145*, 74.

35. Mladenovic, M.; Schmatz, S.; Botschwina, P. *J. Chem. Phys.* **1994**, *101*, 5891.

36. Szczepanski, J.; Vala, M. *J. Phys. Chem.* **1993**, *99*, 7371.

37. Ortman, B. J.; Hauge, R. H.; Margrave, J. L.; Kafafi, Z. H. *J. Phys. Chem.* **1990**, *94*, 7973.

38. Ahmed, S.N.; McKee, M. L.; Shevlin, P. B. *J. Am. Chem. Soc.* **1983**, *105*, 3942.

39. Vala, M.; Chandrasekhar, T. M.; Szczepanski, J.; Pellow, R. *J. Molec. Struct.* **1990**, *222*, 209.

40. Liu, R.; Zhou, X.; Pulay, P. *J. Phys. Chem.* **1992**, *96*, 5748.

41. Szczepanski, J.; Vala, M. *J. Phys. Chem.* **1991**, *95*, 2792.

42. Frisch, M. J.; Trucks, G. W.; Head-Gordon, M.; Gill, P. M. W.; Wong. M. W.; Foresman, J. B.; Johnson, B. G.; Schlegel, H. B.; Robb, M. A.; Replogle, E. S.; Gomperts, R.; Andres, J. L.; Raghavachari, K.; Binkley, J. S.; Gonzales, C.; Martin, R. L.; Fox, D. J.; Defrees, D. J.; Stewart, J. J. P.; Pople, J. A. GAUSSIAN 92, Revision E.1; Gaussian, Inc.: Pittsburgh. PA.

43. Szczepanski, J.; Pellow, R.; Vala, M. *Z. Naturforsch.* **1992**, *47a*, 595.

44. Pitzer, K. S.; Clementi, E. *J. Am. Chem. Soc.* **1959**, *81*, 4477.

45. Bondybey, V. E.; English, J. H. *J. Chem. Phys.* **1978**, *68*, 4640.

46. Hinkle, K. H.; Keady, J. J.; Bernath, P. F. *Science* **1988**, *241*, 1319.

47. Merer, A. *Can. J. Phys.* **1962**, *45*, 4103.

48. Schmuttenmaer, C. A.; Cohen, R. C.; Pugliano, N.; Heath, J. R.; Cooksy, A. L.; Basarow, K. L.; Saykally, R. J. *Science* **1990**, *249*, 897.

49. Shen, L. N.; Graham, W. R. M. *J. Chem. Phys.* **1989**, *91*, 5115.

50. Vala, M.; Chandrasekhar, T. M.; Szczepanski, J.; Van Zee, R.; Weltner, W., Jr. *J. Chem. Phys.* **1989**, *90*, 595.

51. Moszzen-Ahmadi, N.; McKellar, A. R. W.; Amano. T. *Chem. Phys. Lett.* **1989**, *157*, 1.

52. Vala, M.; Chandrasekhar, T. M.; Szczepanski, J.; Pellow, R. *High Temp. Sci.* **1990**, *27*, 19.

53. Kranze, R. H.; Graham, W. R. M. *J. Chem. Phys.* **1992**, *96*, 2517.

54. Heath, J. R.; Saykally, R. J. *J. Chem. Phys.* **1991**, *94*, 3271.

55. Hwang, H. J.; Van Orden, A.; Tanaka, K.; Kuo, E.; Heath, J. R.; Saykally, R. J. *Mol. Phys.* **1993**, *79*, 769.

56. Martin, J. M. L.; Francois, J. P.; Gijbels, R. *J. Chem. Phys.* **1990**, *93*, 8852.

57. Heath, J. R.; Sheeks, R. A.; Cooksy, A. L.; Saykally, R. J. *Science* **1990**, *249*, 895.

58. Heath, J. R.; Van Orden, A.; Kuo, E.; Saykally, R. J. *Chem. Phys. Lett.* **1991**, *182*, 17.

59. Szczepanski, J.; Ekern, S. P.; Pellow, R.; Vala, M. *Chem. Phys.* In Press.

60. Kurtz, J.; Adamowicz, L. *Astrophys. J.* **1991**, *370*, 784.

61. Van Orden, A.; Hwang, H. J.; Kuo, E. W.; Saykally, R. J. *J. Chem. Phys.* **1993**, *98*, 6678.

62. MacIntosh, D. F.; Peterson, M. R. Quantum Chemistry Program Exchange, Program No. QCMP012, Indiana University. 1984.

63. Person, W. B.; Del Bene, J. E.; Szajda, W.; Szczepaniak, K.; Szczesniak, M. *J. Phys. Chem.* **1991**, *95*, 2770.

64. Brown, R. D.; Pullin, D. E.; Rice, E. H. N.; Rodler, M. J. *J. Am. Chem. Soc.* **1985**, *107*, 7877.

65. Irvine, W. M.; Brown, D. M.; Cragg, P.; Friberg, P.; Godfrey, P. D.; Kaifu, N.; Matthews, H. E.; Ohishi, M.; Suzuki, H.; Takeo, H. *Astrophys. J.* **1988**, *355*, L89.

66. Herbst, E.; Smith, D.; Adams, N. G. *Astron. Astrophys.* **1984**, *138*, L13.

67. Brown, R. D.; Godfrey, P. D.; Cragg, D. M.; Rice, E. H. N.; Suzuki, H.; Ohishi, M.; Kaifu, N.; Morimoto, M. *Astrophys. J.* **1985**, *297*, 302.

68. Herbst, E.; Leung, C. M. *Astrophys. J.* **1986**, *310*, 378.

69. Williams, D. A. In *Galactic and Extragalactic Infrared Spectroscopy*, Kessler, M. F., Phillips, J. P., Eds.; D. Reidel: Dordrecht, 1982, p. 242.

70. Herbst, E. *Chem. Phys. Lett.* **1994**, *222*, 297.

71. Herbst, E. *Angew. Chemie, Int. Ed. Eng.* **1990**, *29*, 595.

72. Matthews, H. E.; Irvine, W. M.; Friberg, P.; Brown, R. D.; Godfrey, P. O. *Nature* **1984**, *310*, 125.

73. Petrie, S.; Bettens, R. P. A.; Freeman, C. G.; McEwan, M. J. *J. Phys. Chem.* **1993**, *97*, 13673.

74. Maclagan, R. G. A. R.; McEwan, M. J.; Scott, G. B. *Chem. Phys. Lett.* **1995**, *240*, 185.

75. Szczepanski, J.; Ekern, S. P.; Vala, M. *J. Phys. Chem.* **1995**, *99*, 8002.

76. Farnell, L.; Radom, L. *Chem. Phys. Lett.* **1982**, *91*, 373.

77. Radom, L. *Aust. J. Chem.* **1978**, *31*, 1.

78. Komornicki, A.; Dykstra, C. E.; Vincent, M. A.; Radom, L. *J. Am. Chem. Soc.* **1981**, *103*, 1652.

79. Dykstra, C. E.; Schaefer, H. F. *J. Am. Chem. Soc.* **1978**, *100*, 1378.

80. Schaefer, H. F., III *Acc. Chem. Res.* **1979**, *12*, 288.

81. Brown, R. F. C.; Eastwood, F. W.; Harrington, K. J. *Aust. J. Chem.* **1974**, *27*, 2373.

82. Blackman, G. L.; Brown, R. D.; Brown, R. F. C.; Eastwood, F. W.; McMullen, G. L. *J. Mol. Spectrosc.* **1977**, *68*, 488.

83. Brown, R.D.; Brown, R. F. C.; Eastwood, F. W.; Godfrey, P. D.; McNaughton, D. *J. Am. Chem. Soc.* **1979**, *101*, 4705.

84. Tielens, A. G. G. M.; Allamandola, L. J. In *Interstellar Processes*, Hollenbach, D. J., Thronson Jr., H. J., Eds.; D. Reidel: Dordrecht, 1987, p. 397.

85. Tielens, A. G. G. M.; Allamandola, L. J. *NATO ASI Ser. C (Physical Processes in Interstellar Clouds)*, Morfill, G. E.; Scholer, M., Eds.; 1987, p. 333, No. 210.

86. Williams, D. A. *NATO ASI Ser. C (Physical Processes in Interstellar Clouds)*, Morfill, G. E.; Scholer, M., Eds.; 1987, p. 377, No. 210.

87. Winnewisser, G. *J. Mol. Spectrosc.* **1973**, *46*, 16.

88. Benson, R. C.; Fluygare, W. H.; Oda, M.; Breslow, R. *J. Am. Chem. Soc.* **1973**, *95*, 2772.

89. Brown, R. D.; Godfrey, P. D.; Champion, R.; McNaughton, D. *J. Am. Chem. Soc.* **1981**, *103*, 5711.

90. Ekern, S. P.; Szczepanski, J.; Vala, M. *J. Phys. Chem.* In Press (1996).

91. Frisch, M. J.; Trucks, G. W.; Schlegel, H. B.; Gill, P. M. W.; Johnson, B. G.; Robb, M. A.; Cheeseman, J. R.; Keith, T.; Petersson, G. A.; Montgomery, J. A.; Raghavachari, K.; Al-Laham, M. A.; Zakrzewski, V. G.; Ortiz, J. V.; Foresman, J. B.; Peng, C. Y.; Ayala, P. Y.; Chen, W.; Wong, M. W.; Andres, J. L.; Replogle, E. S.; Gomperts, R.; Martin, R. L.; Fox, D. J.; Binkley, J. S.; Defrees, D. J.; Baker, J.; Stewart, J. P.; Head-Gordon, M.; Gonzalez, C.; Pople, J. A. GAUSSIAN 94, Revision B.2. Gaussian, Inc., Pittsburgh PA, 1995.

92. Judeikis, H. S.; Flournoy, J. M.; Siegel, S. *J. Chem. Phys.* **1962**, *37*, 2272.

93. Muto, H.; Toriymama, K.; Nunome, K.; Iwasaki, M. *Radiat. Phys. Chem.* **1982**, *19*, 201.

94. Hiraoka, K.; Yamashita, A.; Yachi, Y.; Aruga, K.; Sato, T.; Muto, H. *Astrophys. J.* **1995**, *443*, 363.

95. Hiralka, K.; Ohashi, N.; Kihara, Y.; Yamamoto, K.; Sato, T.; Yamashita, A. *Chem. Phys. Lett.* **1994**, *229*, 408.

96. Takahashi, J.; Yamashita, K. *J. Chem. Phys.* **1996**, *104*, 6613.

97. Woon, D. E.; Herbst, E. *Astrophys. J.* **1996**, *465*, 795.

98. Bauschlicher, C. W., Jr.; Langhoff, S. R. J. *J Chem. Phys.* **1987**, *87*, 2919.

99. DeKock, R. L.; Weltner, W., Jr. *J. Am. Chem. Soc.* **1971**, *93*, 7106.

100. Maier, G.; Reisenauer, H. P.; Balli, H.; Brandt, W.; Janoschek, R. *Angew. Chem. Int. Ed. Eng.* **1990**, *29*, 905.

101. Williams, D. A. *Astrophys. J.* **1968**, *151*, 935.

102. Tielens, A. G. G. M.; Hagen, W. *Astron. Astrophys.* **1982**, *114*, 245.

103. Helden, G.; Gotts, N. G.; Bowers, M. T. *Nature* **1993**, *363*, 60.

104. Curl, R. F.; Smalley, R. E. *Sci. Amer.* **1991**, *265*, 32.

105. Iijima, S.; Ichihashi, T. *Nature* **1993**, *363*, 603.

106. Rinzler, A. G.; Hafner, J. H.; Nikolaev, P.; Lou, L.; Kim, S. G.; Tomanek, D.; Nordlander, P.; Colbert, D. T.; Smalley, R. E. *Science* **1995**, *269*, 1550.

107. Heath, J. R.; Saykally, R. J. In *On Clusters and Clustering*, Reynolds, P. J., Ed., Elsevier: Amsterdam, 1993, pp.7-21.

108. Szczepanski, J.; Ekern , S. P.; Vala, M. *Chem. Phys.* In Press (1996).

109. Giesen, T. F.; Vanorden, A.; Hwang, H. J.; Fellers, R. S.; Provencal, R. A.; Saykally, R. J. *Science* **1994**, *265*, 756.

110. Freivogel, P.; Fulara, J.; Jacobi, M.; Forney, D.; Maier, J. P. *J. Chem. Phys.* **1995**, *103*, 54.

111. Watson, J. K. G. *Astrophys. J.* **1994**, 437, 678.

112. Hunter, J. M.; Fye, J. L.; Roskamp, E. J.; Jarrold, M. F. *J. Phys. Chem.* **1994**, *98*, 1810.

113. Ekern, S. P.; Szczepanski, J.; Vala, M. *J. Phys. Chem.* In Press. (1996).

114. Schmatz, S.; Botschwina, P. *Chem. Phys. Lett.* **1995**, *235*, 8.

115. Honig, R. E. *J. Chem. Phys.* **1954**, *22*, 126.

116. Pargellis, A. N. *J. Chem. Phys.* **1990**, *93*, 2099.

117. Arnold, D. W.; Bradforth, S. E.; Kitsopoulos, T. N.; Neumark, D. M. *J. Chem. Phys.* **1991**, *95*, 8753.

118. Kitsopoulos, T. N.; Chick,C. J.; Zhao, Y.; Neumark, D. M. *J. Chem. Phys.* **1991**, *95*, 5479.

119. Arnold, C. C.; Zhao, Y.; Kitsopoulos, T. N.; Neumark, D. M. *J. Chem. Phys.* **1992**, *97*, 6121.

120. Handshuh, H.; Gantefor,G.; Kessler,B.; Bechthold, P.S.; Eberhardt, W. *Phys. Rev. Lett.* **1995**, *77*, 1095.

121. Hutter, J.; Luthi, H. P.; Diederich, F. *J. Am. Chem. Soc.* **1994**, *116*, 750.

122. von Helden, G.; Kemper, P.; Gotts, N. G.; Bowers, M. T. *Science* **1993**, *259*, 1300.

123. Szczepanski, J.; Roser, D.; Personette, W.; Eyring, M.; Pellow, R.; Vala, M. *J. Phys. Chem.* **1982**, *96*, 7876.

124. Szczepanski, J.; Vala, M.; Talbi, D.; Parisel, O.; Ellinger, Y. *J. Chem. Phys.* **1993**, *98*, 4494.

125. Szczepanski, J.; Chapo, C.; Vala, M. *Chem. Phys. Lett.* **1993**, *205*, 434.

126. Vala, M.; Szczepanski, J. *Nature* **1993**, *363*, 699.

127. Szczepanski, J.; Vala, M. *Astrophys. J.* **1993**, *414*, 646.

128. Vala, M.; Szczepanski, J.; Pauzat, F.; Parisel, O.; Talbi, D.; Ellinger, Y. *J. Phys. Chem.* **1994**, *98*, 9187.

129. Szczepanski, J.; Wehlburg, C.; Vala, M. *Chem. Phys. Lett.* **1995**, *232*, 221.

130. Hudgins, D.H.; Sandford, S. A.; Allamandola, L. J. *J. Phys. Chem.* **1994**, *98*, 4243.

131. Hudgins, D. M.; Allamandola, L. J. *J. Phys. Chem.* **1995**, *99*, 3033.

132. Hudgins, D. M.; Allamandola, L. J. *J. Phys. Chem.* **1995**, *99*, 8979.

133. Schlemmer,S.; Cook, D. J.; Harrison, J. A.; Wurfel, B.; Chapman, W.; Saykally, R. J. *Science* **1994**, *265*, 1686.

134. Pellow, R.; Auerbach, E.; Vala, M. *Astrophys. J.* In Press. (1996).

135. Geballe, T. R.; Tielens, A. G. G. M.; Allamandola, L. J.; Moorhouse, A.; Brand, P. W. J. L. *Astrophys. J.* **1989**, *341*, 278.

136. Snow T. P., In *The Diffuse Interstellar Bands*, Tielens, A. G. G. M.; Snow, T. P. Eds., Academic Publishers. Kluwer: Netherlands, 1995, p. 379.

137. McElvany, S. W.; Creasy, W. R.; O'Keefe, A. *J. Chem. Phys.* **1986**, *85*, 632.

138. McElvany, S. W.; Dunlap, B. I.; O'Keefe, A. *J. Chem. Phys.* **1987**, *86*, 715.

139. Bach, S. B. H.; Eyler, J. R. *J. Chem. Phys.* **1990**, *92*, 358.

140. Ramanathan, R.; Zimmerman, J. A.; Eyler, J. R. *J. Chem. Phys.* **1993**, *98*, 7838.

141. Faibis, A.; Kanter, E. P.; Tack, L. M.; Bakke, E.; Zabransky, B. J. *J. Chem. Phys.* **1987,** *91*, 6445.

142. Algranati, M.; Feldman, H.; Kella, D.; Malkin, E.; Miklazky, E.; Naaman, R.; Vager, Z.; Zajfman, J. *J. Chem. Phys.* **1989,** *90*, 4617.

143. Vager, Z.; Feldman, H.; Kella, D.; Malkin, E.; Miklazky, E.; Zajfman, J.; Naaman, R. *Z. Phys. D.* **1991,** *19*, 413.

144. Heber, O.; Kella, D.; Zajfman, D.; Feldman, H.; Majer, D.; Vager, Z.; Naaman, R. *Nuc. Instrum, Methods. Phys. Res., Sect. B* **1993,** *B79*, 27.

145. Graham, W. R. M.; Dismuke, K. I.; Weltner, W., Jr. *J. Chem. Phys.* **1974,** *61*, 4793.

146. Graham, W. R. M.; Dismuke, K. I.; Weltner, W., Jr. *Astrophys. J.* **1976,** *204*, 301.

147. van Zee, R. J.; Ferrante, R. F.; Zeringue, K. J.; Weltner, W., Jr. *J. Chem. Phys.* **1987,** *86*, 5212.

148. Knight, L. B., Jr.; Cobranchi, S. T.; Earl, E. *J. Chem. Phys.* **1988,** *88*, 7348.

149. van Zee, R. J.; Ferrante, R. F.; Zeringue, K. J.; Weltner, W., Jr. *J. Chem. Phys.* **1988,** *88*, 3465.

150. von Helden, G.; Hsu, M.; Gotts, N.; Bowers, M. T. *J. Phys. Chem.* **1993,** *97*, 8182.

151. Hunter, J.; Fye, J. L.; Jarrold, M. F. *J. Chem. Phys.* **1993,** *99*, 1785.

152. von Helden, G.; Hsu, M. T.; Kemper, P. R.; Bowers, M. T. *XIVth Int. Symp. On Molec. Beams*, 1992, 451.

153. Book, L. D.; Xu, C.; Scuseria, G. E. *Chem. Phys. Lett.* **1994,** *222*, 281.

154. Sunil, K. K.; Orendt, A.; Jordan, K. D.; DeFrees, D. *J. Chem. Phys.* **1984,** *89*, 245.

155. Watts, J. D.; Cernusak, I.; Bartlett, R. J. *Chem. Phys. Lett.* **1991,** *178*, 259.

156. Watts, J. D.; Bartlett, R. J. *J. Chem. Phys.* **1994,** *101*, 409.

157. Raghavachari, K. *Chem. Phys. Lett.* **1990,** *171*, 249.

158. Adamowicz, L. *Chem. Phys. Lett.* **1991,** *180*, 466.

159. Adamowicz, L. *Chem. Phys. Lett.* **1991,** *182*, 45.

160. Schmatz, S.; Botschwina, P. *Chem. Phys. Lett.* **1995,** *235*, 5.

161. Lee, C.; Yang, W.; Parr, R. G. *Phys. Rev. B* **1988,** *37*, 785.

162. Becke, A. D. *J. Chem. Phys.* **1993,** *98*, 5648.

163. Becke, A. D. *J. Chem. Phys.* **1988,** *88*, 1053.

164. Barone, V.; Adamo, C.; Mele, F. *Chem. Phys. Lett.* **1996,** *249*, 290.

165. Martin, J. M. L.; El-Yazal, J.; Francois, J. *Chem. Phys. Lett.* **1995,** *242*, 570.

166. Watts, J. D.; Gauss, J.; Stanton, J. F.; Bartlett, R. J. *J. Chem. Phys.* **1992,** *97*, 8372.

167. Rehfuss, B. D.; Liu, D. -J.; Dinelli, B. M.; Jagod, M. -F.; Ho, W. C.; Crofton, M. W.; Oka, T. *J. Chem. Phys.* **1988,** *89*, 129.

168. Szczepanski, J.; Vala, M. *J. Chem. Phys.* **1993**, *99*, 7371.

169. Kaupp, M.; von Schleyer, P.; Stoll, H. *J. Phys. Chem.* **1992**, *96*, 9801.

170. Lakhlifl, A.; Dahoo, R. In Press. (1995).

171. Lakhlifi, A.; Girardet, C.; Dahoo, R.; Brosset, P.; Gauthier-Roy, B.; Abouaf-Marguin, L. *Chem. Phys.* **1993**, *177*, 31.

172. Hastie, J. W.; Hauge, R. H.; Margrave, J. L. In *Spectroscopy in Inorganic Chemistry Vol. 1*, Rao, C. N. R.; Ferraro, J. R. Eds., Academic Press: New York, 1970, p. 74.

173. Jura, M. In *NATO ASI Ser. C (Polycyclic Aromatic Hydrocarbons and Astrophysics)*, Leger, A.; d'Hendecourt, L.; Boccara, N. Eds. 1987, p. 3, No. 191.

174. Fulara, J.; Lessen, D.; Freivogel, P.; Maier, J. P. *Nature* **1993**, *366*, 439.

175. Cook, D. J.; Schlemmer, S.; Balucani, N.; Wagner, D. R.; Steiner, B.; Saykally, R. J. *Nature* **1996**, *380*, 227.

176. d'Hendecourt, L.; Leger, A. *Astron. Astrophys.* **1987**, *180*, L9.

177. Verstraete, L.; Leger, A.; d'Hendecourt, L.; Dutuit, O.; Defourneau, D. *Astron. Astrophys.* **1990**, *237*, 436.

178. Cherchneff, I.; Barker, J. R. *Astrophys. J.* **1989**, *341*, L21.

179. Shan, J.; Suto, M.; Lee, L. C. *Astrophys. J.* **1992**, *388*, L39.

180. Brenner, J. D.; Barker, J. R. *Astrophys. J.* **1992**, *388*, L39.

181. Boissel, P.; Lefevre, G.; Thiebot, P. *Proceedings of the 50th International Meeting of Physical Chemsitry*. 1993. p. 33.

182. Leach, S. In *NATO ASI Ser. C (Polycyclic Aromatic Hydrocarbons and Astrophysics)*, Leger, A.; d'Hendecourt, L.; Boccara, N. Eds. 1987, p. 99, No. 191.

BIOGRAPHICAL SKETCH

Scott Ekern was born on May 5, 1968, in Milwaukee, Wisconsin. After living on a farm in Wisconsin, he moved to Atlanta, Georgia, where he attended middle and high school. Scott received his B. S. degree in chemistry from Auburn University in 1990. His M. S. degree is also from Auburn University and was awarded in 1992. The M. S. degree research in gas-phase ion-molecule reactions and applied computational chemistry was directed by Drs. Andreas Illies and Michael McKee, respectively. Scott began his work at the University of Florida in 1993, receiving his Ph. D. in 1996. The experimental and theoretical work is compiled in this thesis. Scott is a qualified private pilot, and member to the American Chemical Society and the Alpha Iota chapter of Phi Lambda Upsilon, the national chemical honorary society.

I certify that I have read this study and that in my opinion it conforms to acceptable standards of scholarly presentation and is fully adequate, in scope and quality, as a dissertation for the degree of Doctor of Philosophy.

Martin Vala
Professor of Chemistry

I certify that I have read this study and that in my opinion it conforms to acceptable standards of scholarly presentation and is fully adequate, in scope and quality, as a dissertation for the degree of Doctor of Philosophy.

Philip Brucat
Associate Professor of Chemistry

I certify that I have read this study and that in my opinion it conforms to acceptable standards of scholarly presentation and is fully adequate, in scope and quality, as a dissertation for the degree of Doctor of Philosophy.

Willis Person
Professor of Chemistry

I certify that I have read this study and that in my opinion it conforms to acceptable standards of scholarly presentation and is fully adequate, in scope and quality, as a dissertation for the degree of Doctor of Philosophy.

Kirk Schanze
Associate Professor of Chemistry

I certify that I have read this study and that in my opinion it conforms to acceptable standards of scholarly presentation and is fully adequate, in scope and quality, as a dissertation for the degree of Doctor of Philosophy.

Elizabeth Seiberling
Associate Professor of Physics

This dissertation was submitted to the Graduate Faculty of the Department of Chemistry in the College of Liberal Arts and Sciences and to the Graduate School and was accepted as partial fulfillment of the requirements for the degree of Doctor of Philosophy.

December, 1996

Richard J. Fox

Dean, Graduate School

LD
1780
1996
.E361